

Prediction of Limit Cycle Oscillation
in an Aeroelastic System using Nonlinear Normal Modes

Christopher Wyatt Emory

Dissertation submitted to the Faculty of the
Virginia Polytechnic Institute and State University
in partial fulfillment of the requirements for the degree of

Doctor of Philosophy

in

Aerospace Engineering

Mayuresh J. Patil, Chair

Robert A. Canfield

Charles M. Denegri, Jr.

Rakesh K. Kapania

December 3, 2010

Blacksburg, Virginia

Keywords: Nonlinear Aeroelasticity, Limit Cycle Oscillation, Nonlinear Normal Modes

Copyright 2010, Christopher Wyatt Emory

Prediction of Limit Cycle Oscillation in an Aeroelastic System using Nonlinear Normal Modes

Christopher Wyatt Emory

(ABSTRACT)

There is a need for a nonlinear flutter analysis method capable of predicting limit cycle oscillation in aeroelastic systems. A review is conducted of analysis methods and experiments that have attempted to better understand and model limit cycle oscillation (LCO). The recently developed method of nonlinear normal modes (NNM) is investigated for LCO calculation.

Nonlinear normal modes were used to analyze a spring-mass-damper system with nonlinear damping and stiffness to demonstrate the ability and limitations of the method to identify limit cycle oscillation. The nonlinear normal modes method was then applied to an aeroelastic model of a pitch-plunge airfoil with nonlinear pitch stiffness and quasi-steady aerodynamics. The asymptotic coefficient solution method successfully captured LCO at a low relative velocity. LCO was also successfully modeled for the same airfoil with an unsteady aerodynamics model with the use of a first order formulation of NNM. A linear beam model of the Goland wing with a nonlinear aerodynamic model was also studied. LCO was successfully modeled using various numbers of assumed modes for the beam. The concept of modal truncation was shown to extend to NNM. The modal coefficients were shown to identify the importance of each mode to the solution and give insight into the physical nature of the motion.

The quasi-steady airfoil model was used to conduct a study on the effect of the nonlinear normal mode's master coordinate. The pitch degree of freedom, plunge degree of freedom, both linear structural mode shapes with apparent mass, and the linear flutter mode were all used as master coordinates. The master coordinates were found to have a significant influence on the accuracy of the solution and the linear flutter mode was identified as the preferred option.

Galerkin and collocation coefficient solution methods were used to improve the results

of the asymptotic solution method. The Galerkin method reduced the error of the solution if the correct region of integration was selected, but had very high computational cost. The collocation method improved the accuracy of the solution significantly. The computational time was low and a simple convergent iteration method was found. Thus, the collocation method was found to be the preferred method of solving for the modal coefficients.

Contents

1	Introduction	1
2	Literature Review	3
2.1	SEEK Eagle LCO Flight Testing Experiences	3
2.2	LCO Analysis Methods and Experiments	5
2.2.1	Pitch-Plunge Airfoil with Structural Nonlinearities	5
2.2.2	Continuous Systems	12
2.3	Nonlinear Normal Modes	17
3	Nonlinear Normal Modes	18
3.1	Second-Order Formulation	
	with Asymptotic Modal Coefficient Solution	18
3.1.1	Linear Spring-Mass-Damper Example	22
3.1.2	Alternative Eigenvalue Solution to Linear Coefficients	27
3.1.3	Linear Normal Mode (LNM) Solution	30
3.2	First-Order Formulation	31
3.3	Galerkin Modal Coefficient Solution	32
3.4	Collocation Modal Coefficient Solution	35
4	Physical Models	37
4.1	Two Degree-of-Freedom Van der Pol Style Oscillator	38
4.2	Nonlinear Pitch-Plunge Airfoil with Quasi-Steady Aerodynamics	38

4.3	Nonlinear Pitch-Plunge Airfoil with Unsteady Aerodynamics	41
4.4	Goland Beam Wing with Nonlinear, Quasi-Steady Aerodynamics	43
5	Results	47
5.1	Two Degree-of-Freedom	
	Van der Pol Style Oscillator	48
5.2	Pitch-Plunge Airfoil	
	with Quasi-steady Aerodynamics	60
	5.2.1 Sample Results	60
	5.2.2 Master Coordinate Study	70
	5.2.3 Galerkin Modal Coefficient Solution	74
	5.2.4 Collocation Modal Coefficient Solution	81
5.3	Pitch-Plunge Airfoil	
	with Unsteady Aerodynamics Sample Results	87
5.4	Goland Beam Wing	96
	5.4.1 Modal Truncation	97
6	Conclusions	105
6.1	Future Work	106
	Bibliography	109

List of Figures

3.1	Three Degree-of-Freedom Spring-Mass-Damper System	23
4.1	Nonlinear Spring-Mass-Damper	39
4.2	Pitch-Plunge Airfoil Model	40
4.3	Goland Wing Model	43
5.1	Nonlinear SMD Phase Space Diagrams for First NNM, Case 1	52
5.2	Nonlinear SMD Phase Space Diagrams for Second NNM, Case 1	53
5.3	Nonlinear SMD Phase Space Diagrams for First NNM, Case 2	54
5.4	Nonlinear SMD Phase Space Diagrams for Second NNM, Case 2	55
5.5	Nonlinear SMD Time History for First NNM, Case 1	56
5.6	Nonlinear SMD Time History for Second NNM, Case 1	57
5.7	Nonlinear SMD Time History for First NNM, Case 2	58
5.8	Nonlinear SMD Time History for Second NNM, Case 2	59
5.9	LCO Time History Plots of Quasi-steady Airfoil at $1.05 V_f$	63
5.10	LCO Phase Space Plots of Quasi-steady Airfoil at $1.05 V_f$	64
5.11	Damped Mode Time History Plots of Quasi-steady Airfoil at $1.05 V_f$	65
5.12	Growth of LCO Motion in Exact System due to Approximate Initial Condition	66
5.13	LCO Phase Space Plots of Quasi-steady Airfoil at $1.17 V_f$	67
5.14	Frequency vs. Velocity	68
5.15	Amplitude vs. Velocity	68
5.16	Asymptotic Convergece at $1.01V_f$	69

5.17 Asymptotic Convergece at $1.05V_f$	69
5.18 Master Coordinate Amplitude Error Results	73
5.19 Master Coordinate Frequency Error Results	74
5.20 Galerkin with Integration Region $0.5\times$ Exact Amplitudes, $1.17V_f$	76
5.21 Galerkin with Integration Region $1.0\times$ Exact Amplitudes, $1.17V_f$	77
5.22 Galerkin with Integration Region $1.2\times$ Exact Amplitudes, $1.17V_f$	78
5.23 Galerkin with Integration Region $1.4\times$ Exact Amplitudes, $1.17V_f$	79
5.24 Galerkin with Integration Region $1.6\times$ Exact Amplitudes, $1.17V_f$	80
5.25 Galerkin with Integration Region $1.2\times$ Exact Amplitudes, $1.5V_f$	82
5.26 Collocation Modal Coefficient Solution Sample Results at $1.17V_f$	84
5.27 Motion Growth with Collocation Solution	86
5.28 Collocation Iteration 1 at $1.5V_f$	89
5.29 Collocation Iteration 2 at $1.5V_f$	90
5.30 Collocation Iteration 4 at $1.5V_f$	91
5.31 Steady LCO results at $\bar{u} = 1.05V_f$ for Linear Flutter Mode - US Aero	93
5.32 Steady LCO results at $\bar{u} = 1.17V_f$ for Linear Flutter Mode - US Aero	94
5.33 Normalized Unsteady (US) vs. Quasi-steady (QS) LCO solution at $1.17V_f$	95
5.34 Goland Wing with 5 Bending and 5 Torsion Modes	97
5.35 Goland Wing with Multiple Modal Solutions	101
5.36 Goland Wing LCO Amplitude Error vs. Number of Modes	102

List of Tables

5.1	NNM Results for SMD with Nonlinear Damping	51
5.2	Galerkin Integration Region Data	75
5.3	Collocation Results	83
5.4	Collocation Iteration at a High Velocity	88
5.5	Beam Wing Flutter Velocities and Run Speeds	100
5.6	Beam Wing Error	100
5.7	Beam Wing CPU Times in Seconds	101
5.8	Beam Wing Modal Coefficients	103
5.9	Normalized Beam Wing Modal Coefficients	104

Chapter 1

Introduction

Aeroelasticity is the interaction of aerodynamic, elastic, and inertial forces. Flutter is an aeroelastic phenomenon in which a dynamic instability occurs due to the interaction of aircraft surfaces, most often wings, with the air flowing past. In classical flutter, the wing will cyclically increase in amplitude until it breaks which can occur in very few cycles. A number of modern aircraft, such as the F-16, have also experienced a phenomenon termed a limit cycle oscillation (LCO) in which the wing behaves similarly to a flutter situation, but does not diverge. One or more nonlinearities, such as geometric, aerodynamic, stiffness, or structural damping, in the system act to limit the amplitude of the motion. In the case of the F-16, the occurrence of LCO can make it difficult or impossible for the aircrew to perform necessary tasks. If the amplitude is large enough, the motion can damage the aircraft or stores attached to the wings[1].

Flutter has typically been modeled with linear analysis. Since LCO is by its very nature nonlinear, these linear models are not capable of predicting all aspects LCO. Linear flutter analysis has been demonstrated to be adequate to predict the frequency and modal composition, but it is incapable of identifying the onset velocity or the amplitude[2]. This inability to fully predict the LCO creates the need for extensive flight testing. For an aircraft like the F-16, the number of under-wing store configurations has been increasing and flight testing costs are continually rising[3]. Denegri identifies the need for a nonlinear flutter

analysis method capable of predicting all the aspects of LCO behavior[2][3].

Many models and experiments, covered in detail in the following literature review, have been pursued to aid in the development of a model capable of capturing the physics involved in LCO. Many of these models are purely computational. Most simply are not practical for modeling a real world case like the F-16 due to the large amount of computation necessary. One of the most promising modeling approaches has been harmonic balance and it has been applied to a few F-16 test cases with somewhat favorable results[4].

The goal of this work is to take a step toward a new, practical method of nonlinear analysis to model LCO that offers insight into the physics underlying the LCO phenomena. Furthermore, the analysis methodology should be extendable to complex real world problems in the future. The method of nonlinear normal modes (NNM), which was developed during the 1990's, is explored as an alternative method of LCO prediction. The NNM model can reduce the order of the system to a single degree of freedom while trying to maintain some or all nonlinearity and the effect of all degrees of freedom desired in the model. Only having to solve a system with a single degree of freedom could save considerable computational time. The modal analysis nature of NNM should also offer some unique information about the physical modeshapes involved in LCO motion.

Terminology used in the description of flutter and LCO is often ambiguous and confusing. Many papers use the same terms to mean different things. As such, in this paper the following definitions will be used throughout unless explicitly noted. LCO will refer to a sustained periodic oscillation due to nonlinear aeroelastic interaction. Linear flutter or classic flutter refers to divergent aeroelastic oscillations in a linear system or model. Nonlinear flutter refers to divergent aeroelastic oscillation in a nonlinear system or model. A flutter or LCO boundary refers to a line or curve that dictates the onset of the particular aeroelastic phenomenon in a freestream velocity and other variable space.

Chapter 2

Literature Review

This literature review is composed of three sections. The first section reviews papers from the US Air Force SEEK Eagle office about their experiences with limit cycle oscillation (LCO) in Flight Testing of the F-16. The following section reviews a number of modeling techniques and experiments that other researchers have used to study flutter and LCO. The final section briefly reviews the development and implementation of nonlinear normal modes.

2.1 SEEK Eagle LCO Flight Testing Experiences

Bunton and Denegri^[1] discuss the general characteristics of LCO encountered in the F-16 and the basic problems that are caused. LCO is found to occur at high subsonic and transonic speeds. The response is characterized by antisymmetric motion of the wings. The behavior has been observed in both straight-and-level flight and elevated load factor maneuvers. The motion is self sustaining and displays hysteresis with respect to the onset airspeed and load factor. Typically, LCO has a fixed amplitude for a given set of flight conditions and the amplitude increases with airspeed. A number of different LCO behaviors have been observed as the load factor is increased. In some cases, the amplitude increases gradually as the load factor is increased while in others the amplitude suddenly drops off at a higher load factor. It is also possible for the LCO to suddenly appear at a high load factor and then grow rapidly

with further increased load factor. The LCO can make it difficult or impossible for the aircrew to perform necessary tasks and if the LCO amplitude is large enough, it can damage the aircraft or stores carried under-wing.

Denegri[2] demonstrates that linear flutter analysis is adequate to predict LCO frequency and modal composition, but is unable to predict the onset velocity or amplitude of LCO. Typical LCO is defined by a gradual onset of sustained oscillation that has a constant amplitude for given flight conditions. The amplitude of typical LCO increases with an increased airspeed. Nontypical LCO is defined as sustained oscillations that are only present over a limited speed range, first appearing and then disappearing when airspeed is increased. Typical LCO, nontypical LCO, and classic flutter are all shown to occur in F-16 flight tests. It is hypothesized that the antisymmetry of the LCO motion is due to the ease of energy transfer in antisymmetric fuselage body modes as opposed to the high resistance in symmetric fuselage body modes. Denegri[2] conveys the need for a nonlinear flutter analysis method capable of discerning the difference between typical LCO, nontypical LCO, and classical flutter behaviors discussed.

Denegri et al.[3] studied the progression of the LCO mode shape in the F-16 wing as flight speed and load factor were increased. Flight tests of the F-16 show that at the onset of LCO the mode shape bears a strong resemblance to the linear flutter mode shape from analysis. The mode shape becomes increasingly nonsynchronous (more galloping character) as the speed, and therefore the amplitude, was increased. At a high speed and load factor, the motion was seen to become nearly synchronous while maintaining LCO which indicates a change in mechanism. The authors hope their observations can help shed light on the physical mechanisms involved in the nonlinear behavior. They further state that it is necessary to find methods to accurately predict flutter and LCO characteristics because the cost of flight testing is growing and the number and combinations of store configurations are continually increasing requiring more flight tests to insure the safety of pilots and equipment.

Dawson and Maxwell[5] present a study of asymmetric store configurations on the F-16. It is shown that asymmetric store configurations can lead to a higher or lower critical

flutter and LCO speed than symmetric installations of each half of the asymmetric configuration. This proves that the industry practice of using half span models and assuming the more critical case can unnecessarily limit the flight envelope or be catastrophically dangerous if a low flutter speed is not predicted. Flight tests demonstrate that the LCO behavior can be better or worse for an asymmetric configuration than the symmetric halves. It makes obvious the need for models that are able to capture the complex behavior in an asymmetric aircraft configuration.

2.2 LCO Analysis Methods and Experiments

2.2.1 Pitch-Plunge Airfoil with Structural Nonlinearities

The aeroelastic behavior of a two degree of freedom, pitch-plunge airfoil with a nonlinear stiffness in one or both degrees of freedoms has been the focus of many analyses. The first nonlinear investigation of this model was conducted by Woolston et al.[6] through the use of an analog computer. They studied nonlinearities due to freeplay, hysteresis, a soft cubic pitch spring, and a hard cubic pitch spring. For the hard cubic spring, the LCO boundary did not change as compared to the linear flutter boundary and LCO was predicted beyond the linear flutter velocity. The LCO amplitude increased as the velocity was increased. For the soft cubic spring, the nonlinear flutter motion was highly divergent beyond the linear flutter velocity. Furthermore, the nonlinear flutter onset velocity decreased as the initial condition amplitude was increased. Beyond a small initial condition, the freeplay nonlinearity significantly decreased the nonlinear flutter speed. Over a moderate initial condition range, the system experienced LCO and beyond the moderate range divergent nonlinear flutter was encountered. Experimental results were obtained for the freeplay case and compared well with the analog computer simulation. For the case with hysteresis, the linear flutter boundary was again reduced for large enough initial conditions forming a different nonlinear flutter boundary. For speeds between the lower nonlinear onset velocity and the linear flutter velocity, the system experienced LCO. Divergent flutter was experienced beyond the

linear flutter boundary. Overall, the nonlinear flutter speed did not change from the linear flutter speed for small disturbances. For larger initial conditions, the nonlinear flutter speed decreased for all cases except the hard cubic spring.

Lee and LeBlanc[7] studied the effects the airfoil/air mass ratio, undamped plunge and pitch natural frequencies, distance between the center of mass and the elastic axis, and multiple cubically nonlinear pitch stiffnesses. Their analysis was accomplished via time marching of the nonlinear differential equations with Houbolt's[8] implicit finite difference method. The time marching scheme used in this paper was later used in many others.

An airfoil with bilinear and cubic nonlinearities in pitch was investigated by Prince et al.[9]. They used Wagner's function for the aerodynamics and the nonlinear differential equations were integrated with the finite difference method of Houbolt[8]. The equations were also solved with the harmonic balance method which was originally derived by Krylov and Bogoliubov[10]. The effect of a moment preload on the airfoil was studied. The results showed LCO well below the linear flutter velocity for both bilinear and cubically nonlinear stiffnesses. The finite difference method identified a secondary bifurcation, which was not found by the harmonic balance method due to its assumption that the fundamental harmonic dominates the behavior of the system. Chaotic motion was shown in particular cases for the cubic system showing that chaos can occur in the continuously nonlinear system.

The chaotic motion of the airfoil with a cubically nonlinear stiffness was also studied by Zhao and Yang[11]. The harmonic balance method and fourth order Runge-Kutta was used to search for chaotic motion. Chaotic motion was found only for a limited range of elastic axis positions and only when the freestream velocity was in excess of the static divergence speed.

Lee, Gong, and Wong[12] introduced four new aerodynamic variables to eliminate the aerodynamic lag integrals in the aeroelastic equations of motions. Earlier work had solved the Wagner function integrals at each time step for the unsteady aerodynamics. With the elimination of the integrals the system could be written in terms of eight first-order ordinary differential equations in the time domain making analytical analysis of the equations

possible. For this study, only harmonic solutions to these equations were considered. The method of slowly varying amplitude was used to investigate the behavior of the system. Equilibrium points were computed for the harmonic solution and a linear stability analysis was performed to determine stability of the equilibrium points. The authors provided a technique to determine the amplitude-frequency relationship. Their results were obtained by assuming the effects of high harmonics were small and amplitudes were slowly varying functions of time. The results compared well with fourth-order Runge-Kutta and the Lee and LeBlance[7] numerical time integration of exact equations.

The eight first-order differential equation form was further used by Lee, Jiang, and Wong[13] to study both soft and hard cubic springs. For a soft spring, the nonlinear flutter speed decreases with increases in the pitch and plunge initial conditions. For a hard spring, the nonlinear flutter boundary is independent of the initial conditions and beyond the flutter boundary limit cycle oscillation occurs instead of divergent flutter. LCO amplitude increases as the speed is increased. For a hard spring, an approximate method was used to estimate the frequency and agreement with Runge-Kutta simulation was found to be dependent on the plunge-pitch frequency ratio. An asymptotic theory that was a function of the estimated frequency was used to find the LCO amplitude. Results were good for small frequency but deteriorated for larger frequency values. The authors suggested that the results could be improved with the application of center manifold theory.

Center manifold theory was applied to the nonlinear airfoil by Liu, Wong, and Lee[14]. The pitch-plunge airfoil equations were formulated in the eight first-order differential equation form. The center manifold theory was then applied to reduce the order of the system from eight to two states. The reduced system was then studied with varying linear and nonlinear stiffness coefficients. The results of the reduced system closely matched the behavior of a simulation of the original equations. The reduced order results compared well near the linear flutter velocity where the center manifold was formulated. However, the results deteriorated as velocity was increased above the linear flutter velocity. The general behavior of reduced system's LCO was comparable to that observed in other studies.

With the eight first-order equation form, Liu and Dowell[15] studied the effect of adding higher harmonics to the harmonic balance method. A secondary bifurcation was detected via time stepping when the flow velocity was increased past the initial bifurcation at the linear flutter velocity. The velocity at which the secondary bifurcation occurred depended on the initial condition. The authors show that secondary bifurcation cannot be identified with a quasi-steady aerodynamic assumption. The secondary bifurcation was thoroughly examined with Runge-Kutta integration to create region of attraction diagrams over a range of initial conditions. The effect of changing the number of harmonics included in the harmonic balance method was then examined. The results indicate that at least nine harmonics must be included to detect the secondary bifurcation. As the harmonics were increased beyond nine, the results better matched the numerical simulation. The results with a higher number of harmonics give a more precise speed of the secondary bifurcation. The harmonic balance method only identifies the multiple steady motions and cannot determine the effect of initial conditions or the stability of the steady motions identified. All branches identified with time stepping are considered stable. A perturbation analysis was used to determine the stability of the branches identified in the harmonic balance method. Perturbation of a linearized system was shown to be adequate to identify the stable motions.

In a follow up study, the high dimensional harmonic balance method (HDHB) was used to study the secondary bifurcation[16]. HDHB is a reformulation of the harmonic balance method in terms of time domain variables. The dependent variables are motion values at a number of equally spaced sub-time intervals over one cycle. This circumvents the necessity of having to derive the analytical expression of the Fourier coefficients. The HDHB variables are related to the harmonic balance variables by a constant Fourier transformation matrix. At the secondary bifurcation the amplitude almost doubled, and the pitch motions switched from one peak per cycle to three, while the plunge remained at one peak per cycle. The results of the HDHB compared well with Runge-Kutta results. For small amplitude motion near the linear flutter velocity, the harmonic balance and the HDHB were close to time marching results. Away from this point the difference between the harmonic balance, HDHB, and

Runge-Kutta results became significant. For an equal number of harmonics included, the harmonic balance is more accurate than the HDHB. To get the same order accuracy, the HDHB must include approximately twice as many harmonics. However, harmonic balance is difficult to derive with a large number of harmonics and HDHB is easy to derive and implement even with a very large number of harmonics included.

Nonlinear Aeroelastic Test Apparatus (NATA)

The NATA model has been used for many nonlinear studies of the classic two-dimensional pitch-plunge symmetric airfoil model. A unique test carriage was developed for the low speed wind tunnel at Texas A&M. The carriage allows for variation of the nonlinear pitch and plunge stiffness through the use of custom shaped cams. The carriage has to plunge with the wing, but only the wing pitches creating the only major difference from the classic two degree of freedom model and experiments. This is easily dealt with by a simple addition to the mass term in the standard plunge equation.

For one of the early experiments with the NATA model[17], the equations of motion included a Coulomb damping term and retained nonlinearities in structural stiffness and kinematics. The aerodynamics were modeled using an approximation of Wagner's function which includes a convolution integral. The simulation of the equations was accomplished with the finite difference scheme of Houbolt[8] using a recurrence formula for the convolution integral. Experiments found stall flutter of the model with linear stiffnesses to occur at a pitch amplitude of 0.25 radians. The nonlinear stiffness resulted in LCO pitch amplitudes sufficiently below the stall flutter amplitude; therefore, the aerodynamics are assumed to be linear. The LCO is thus assumed to be caused by structural nonlinearity alone. The stability boundary was shown to be sensitive to initial conditions if Coulomb damping was included and was not affected if only viscous damping was modeled. The LCO was shown to have the same amplitude and frequency for a given freestream velocity regardless of initial conditions. The amplitude of the LCO was shown to increase with an increase in freestream velocity. Freestream velocity had no measurable effect on the experimental LCO frequency, but the

predicted frequency showed a gradual increase. The prediction of LCO amplitude showed the proper trends, but the magnitudes differed by an appreciable amount.

Gilliatt et al.[18] modeled the NATA system with cubically nonlinear, quasi-steady aerodynamics and cubically nonlinear spring stiffness. A fourth-order Runge-Kutta method with a variable time step was used to simulate equations. The initial conditions used were always displacements and not velocities. Experiments with a linear structure indicated that stall flutter occurred at a pitch amplitude of 0.25 radians. LCO measured for the nonlinear stiffness case had amplitudes well below the stall flutter amplitude. LCO was observed over a ten meter per second airspeed band with little change in amplitude. The results agreed with experiments and analysis performed previously. LCO is said to be due to nonlinear structure because pitch amplitude is within the area where linear aerodynamics are applicable. Sensitivity of the flutter/LCO boundary to the initial conditions was observed and attributed to coulomb damping. The resulting LCO amplitude was not a function of the initial conditions. A fast Fourier transform analysis of the data showed higher harmonics were present in the motions, especially in plunge degree of freedom. The predicted fundamental frequency was a little higher than measured. The authors attempted to study internal resonance in the system but conveyed the difficulty of understanding the phenomenon in terms of the original dynamic equations.

Gilliatt et al.[19] demonstrated that internal resonances are theoretically possible in the NATA model with a linear stiffness and quasi-steady aerodynamics with a cubic stall model.

O'Neil and Strganac[20] modeled the NATA apparatus with viscous and Coulomb damping, kinematic nonlinearities, centripetal acceleration, and transcendental terms all included in the equations of motion. For aerodynamics, Theodorsen's equations were used with $C[k] = 1$ leading to quasi-steady aerodynamics. Both pitch and plunge stiffnesses were nonlinear, but the pitch nonlinearity was much larger as compared to the plunge nonlinearity. The equations of motions were integrated following the approach used by Lee and LeBlanc[7] where the finite difference approximation of Houbolt[8] was used. The reduced frequency

was observed to be small enough that quasi-steady aerodynamic assumption was valid (k approximately 0.1). Experiments were done with linear and nonlinear stiffness. The tests were conducted by holding the model at an initial condition and releasing it in a stabilized freestream velocity. Experiments were conducted to validate the zero freestream velocity prediction and at a freestream velocity slightly greater than linear flutter velocity. Slight differences attributed to small unmodeled nonlinearities were noted between predicted and actual response for the linear case. Results showed that flutter was suppressed as the elastic axis was moved toward the center of gravity, effectively mass balancing the system. Nonlinear spring coefficients were found by a cubic curve fit. Prediction at a freestream velocity slightly greater than linear flutter velocity showed LCO, but pitch amplitude was too large to compare to experiment. A higher nonlinear pitch stiffness coefficient was used to keep the amplitude in linear aerodynamic bounds. Higher freestream velocity was observed to increase LCO amplitude. LCO onset showed sensitivity to initial conditions which was credited to presence of Coulomb damping. Analytic results showed good agreement with the experiment and are consistent with findings of other studies.

Thompson and Strganac[21] added an under wing store to the NATA model. Quasi-steady aerodynamics were used with equations allowing for nonlinear stiffness, viscous damping, Coulomb damping, nonlinear kinematic terms. The analysis used a linear plunge stiffness and a fifth order polynomial for pitch stiffness. Sine and cosine in the nonlinear kinematic terms were replaced with Taylor series expansions to the third order. This study used the method of variation of parameters to analyze the system and show the advantage of including kinematic nonlinearities. It was quickly seen that the kinematic nonlinearities are important to the response of the system. The equations of motion were numerically integrated ignoring structural damping and with a small freestream velocity in an attempt to study internal resonance in the system. The pitch stiffness was held constant while the plunge stiffness varied to provide varied frequency responses. A slow modulation was observed when a 1:3 frequency ratio was prescribed which is indicative of internal resonance. It is still unclear if there is a link between store-induced LCO and internal resonance, but the results make it

clear that nonlinear analysis is necessary to model the effect of the store. The study notes the difficulty of studying internal resonance in a highly damped systems because amplitudes drop too quickly to identify amplitude modulation.

Sheta et al.[22] analyzed the NATA model with a high fidelity multidisciplinary computational environment (MDICE). A nonlinear structure typical of the previous studies of the NATA model was used. Aerodynamics were computed with the full Navier-Stokes equations, which are generally nonlinear, using CFD-Fastran. MDICE was used for aeroelastic simulation. The response to an initial plunge displacement was studied. The predicted pitch and plunge response agreed well with experimental observations over a range of freestream velocities. As expected, LCO amplitude increased with the freestream velocity. Theory and experiment showed a small change in frequency over velocity range. The relatively small variation in LCO behavior over the large freestream velocity range used suggests that the LCO was strongly dependent on the structural nonlinearity. The study demonstrated the importance of modeling the flow viscosity by comparing the MDICE results to a simpler aerodynamic model. The authors claim the viscosity effects can not be modeled accurately if analytic aerodynamic formulations are used and that the accurate results show the importance of a high fidelity model.

2.2.2 Continuous Systems

Beam-like Cantilever Wings

Kim and Strganac[23] studied the effect of various nonlinearities on the LCO behavior of a cantilevered beam-like wing. Structural nonlinearities were included to the third order with nonlinear beam equations. Aerodynamic nonlinearities were included with a quasi-steady model including a simple cubic stall model. Kinematic nonlinearities were included for a store attached beneath the wing. The Galerkin Method was used to transform the PDEs into ODEs which were then converted to state space form. Phase portraits were used to investigate the effect of each nonlinearity individually and in all possible combinations. All cases were examined above and below the linear flutter velocity. The motion damped out be-

low the flutter velocity and continuously increases in amplitude above the flutter velocity for nonlinearities in structure only, store only, and structure and store. For aerodynamic nonlinearity alone and aerodynamic with structural or store nonlinearities, the motion damped out below the flutter velocity and goes to a single LCO above the flutter velocity. When all three nonlinearities were combined, a single LCO is found above the flutter velocity. Below the flutter velocity, the behavior depended on the initial condition. For a small initial condition, the motion damped out, but for a larger one the motion went to an LCO.

In a follow up study, Kim and Strganac[24] included variation of the mass, inertia, and position of the under wing store. The LCO behavior was found to be dependent on the store parameters. In all the cases considered, LCO existed below the linear flutter speed for a larger initial condition and motion damped out for a smaller initial condition. Otherwise the results were similar to the previous study. Poincare maps were also used to help better understand the bifurcation behavior.

Plate-like Wings

Tang et al.[25] studied LCO of a cantilevered rectangular plate wing. A three dimensional, time domain, unsteady vortex lattice model with a reduced-order aerodynamic eigenmode technique was used to model the aerodynamics. A quasi-static correction was used to account for the neglected aerodynamic eigenmodes. Nonlinear structural equations were derived with Hamilton's Principle and Lagrange's Equations based on the Von Karman nonlinear plate equations. Approximate structural modes were used to with Lagrange's equations. The method assumed that all nonconservative forces acted in the direction perpendicular to the plate. The system was written in discrete time form and a standard discrete time algorithm was used to calculate the nonlinear response of the system with the complete and reduced order aerodynamic model. It was shown that only a few aerodynamic eigenmodes need to be retained in the aeroelastic model to attain good accuracy. The plate wing was a constant thickness with aspect ratio varied from 0.75 to 10 for different cases. The linear flutter motion was shown to be dominated by the coupling between the first two structural modes,

spanwise bending and the rigid plunge and rotation modes in the chordwise direction. With the velocity set at less than linear flutter velocity, the motion damped out. When the velocity was set greater than the linear flutter velocity an LCO was shown to exist. There was good agreement between the full and reduced aerodynamic model results. The LCO frequency and amplitude were found to increase as the flow velocity increases. The amplitude increased faster when the aspect ratio was higher.

Tang et al.[26] went on to study the LCO of a cantilevered plate delta wing. The aerodynamic and structural models followed the same procedure as the previous except that they were adapted to the delta wing shape. Linear flutter results were shown to be nearly identical for the full and reduced order aerodynamic models. Results were very close between the reduced and full model in nonlinear cases. An experiment was conducted with a 45 degree Lucite wing with center 60% of root clamped. Good agreement was found between theoretical and experimental natural frequencies. Good agreement was also found between the theory and experimental LCO amplitudes and frequencies.

Tang and Dowell[27] expanded the previous study of LCO in a delta wing model to study the effect of an initial steady angle of attack. The same theoretical model was used with the addition of a steady angle of attack term. The initial angle of attack was varied from 0 to 2 degrees. The authors discussed how the structural natural frequency varied as the airspeed increased due to increased static deflection. The analysis showed that as the static angle of attack was increased the flutter velocity decreased. At higher static angles the primary mode of flutter changed from the coupling of the first structural modes to coupling of higher order modes. LCO was only observed above the linear flutter velocity for this system. As the flow velocity increased, both the static and dynamic amplitude were seen to increase with a small angle of attack. After crossing a certain angle, the dynamic amplitude was seen to decrease as the velocity was increased further. At even higher angles of attack, the dynamic amplitude was shown to completely disappear. At one of the higher angles of attack, the LCO amplitude and frequency experienced a jump phenomenon from a larger dynamic amplitude to a small one. The frequency increased more than two-fold at the same jump

point. At the next angle, the LCO was dominated by the after jump behavior. Overall the maximum LCO amplitude is shown to decrease as the steady angle of attack is increased for a given speed. The frequency rose and then fell slowly before the jump to higher frequency, after which it stayed relatively constant as the steady alpha is increased further. The jump is supposed to correspond to the change from the lower to higher structural modes.

Attar et al.[28] expanded the steady angle of attack study to include experimental data. In the experiment the static angle of attack was set and then the airspeed was incrementally increased. Five cases were examined from 0 to 4 degrees in 1 degree increments. Theoretically, both clamped and free restraints on the in-plane motion were considered. The theoretical and experimental plate natural frequencies matched well. The fully clamped in-plane boundary condition proved to be much too stiff and the zero restraint case modeled the experimental behavior better. The velocity for this study was limited to a narrow band. All the LCO found consisted of a coupling between the first bending and first torsion modes. The theoretical model showed a slight increase in frequency with both angle of attack and flow velocity while the experiment showed a slight decrease. Both theoretical and experimental frequency changes were very small. Both the experiment and theory showed an increase followed by a decrease in the flutter speed as the static angle of attack increased. Both also showed an increase in the magnitude of the LCO at a given velocity for higher static angle of attack. The qualitative results agreed relatively well.

The same delta wing model was used yet again by Tang et al.[29]. For this study a store was added near the wing tip. The store was modeled as a slender rigid body attached to the wing at two points. The forward connection was pinned and the aft connection was a spring. A slender body aerodynamic model was applied to the store. The effect of the placement of the store on the wing was studied and it was found that the LCO behavior was sensitive to the store span location and the stiffness of the spring connection. When the store was near the leading edge, the flutter velocity was higher than if the store was to the rear. The theory predicted the flutter velocity and the frequency well, but it did not accurately predict the amplitude of the LCO.

Tang and Dowell[30] added a freeplay gap to the spring connection at the store's aft end. For this study, the store was moved around the wing and the freeplay gap was varied. The LCO amplitude had a significant dependence on the store's initial conditions and pitch motion. As in the previous study, the LCO was sensitive to the location of the store and additionally it was sensitive to the freeplay gap value. The theoretical results were good around the flutter velocity in a qualitative sense, but were poor at higher velocities.

Attar, Dowell, and White[31] and Attar, Dowell, and Tang[32] used a high fidelity nonlinear structural model with a linear vortex lattice model in the finite element package ANSYS to study the delta wing model from the previous studies with and without a store. For cases without the store, the correlation between the high fidelity model and the experiment were better than the von Karman model. The LCO amplitudes and frequencies predicted by the high fidelity model matched well with the experimental values. When the store was added to the high fidelity model, it accurately predicted sensitivity to the spanwise location of the store. With the store placed closer to the root, the experiment and theory showed that the model had a low sensitivity to an initial non-zero angle of attack. With the store placed further out the wing, the experimental model showed a high sensitivity of the flutter velocity to an initial angle of attack. This behavior was not predicted by the analytical model and it was suspected that the simplicity of the aerodynamic model was to blame.

Attar and Gordnier[33] analyzed a cropped delta wing model with a well validated finite difference Euler fluid solver implicitly coupled to a high fidelity finite element structural solver via subiteration. The structural solver was formulated in a co-rotational manner to accurately model large deflections and rotations. This was an improvement over von Karman theory which allows only for moderate rotations. The solver did not significantly improve over previous simpler formulations in the flow regime where experimental data was available; however, it differed from the simpler model as the flow velocity was increased more and the LCO amplitude became higher. The current model was thought to be a more accurate prediction because it was better able to capture the aerodynamic and structural effects at the higher amplitudes.

2.3 Nonlinear Normal Modes

Shaw and Pierre[34] extended the linear system concept of normal modes of vibration to general nonlinear systems. Drawing inspiration from the center manifold reduction technique, they constructed invariant manifolds which represent a normal mode of motion for nonlinear systems with finite degrees of freedom. The initial paper constructed the manifold with an approximate asymptotic approach. This approach limits itself to systems with weak nonlinearities and the order of accuracy cannot be determined *a priori*.

A number of extensions and improvements have been made to the method of nonlinear normal modes. Shaw and Pierre[35] reformulated the method in terms of continuous systems. The original single mode manifolds were incapable of modeling internal resonances present in the system. Pesheck et al.[36] developed multi-mode manifolds which made it possible to include coupling between modes due to internal resonance in a single nonlinear normal mode. A Galerkin-based approach of formulating the manifolds was introduced which allowed a user to prescribe a domain and the order of accuracy of the nonlinear normal mode[37]. All of the nonlinear normal modes mentioned so far assumed the system was not forced. Jiang, Pierre, and Shaw[38] incorporated the ability to include a harmonic excitation into the method.

The application of nonlinear normal modes to structural dynamics problems was considered by Pierre et al[39]. The method was demonstrated with the Galerkin formulation on the classic spring-mass-damper problem including nonlinearities, a finite element beam supported by a nonlinear spring on one end, and on a simple finite element rotating blade model. The frequency response of the beam model was also shown with the method including harmonic excitation. Pesheck et al.[40] presented a thorough study of nonlinear normal modes applied the structural dynamics of a helicopter rotor blade model.

Chapter 3

Nonlinear Normal Modes

Nonlinear normal modes (NNM) are an extension of the theory of linear normal modes to systems with nonlinearities. A modal motion relationship is formulated through the use of invariant manifolds. In this chapter the theory of NNM is developed. The second-order formulation of Shaw and Pierre[34] is presented first and includes an example. This derivation includes the asymptotic manifold approximation. Then, a generalization of the second-order formulation to include first-order systems is presented. The first-order formulation was required to allow the use of unsteady aerodynamics and certain master coordinates useful in the analysis of aeroelastic LCO. The final two sections detail new approaches for calculating the modal coefficients solution, including the Galerkin approach and a collocation approach. The collocation approach is ideal for the LCO studied in this dissertation.

3.1 Second-Order Formulation

with Asymptotic Modal Coefficient Solution

This section mostly follows the derivation of nonlinear normal modes by Shaw and Pierre[34]. A few changes in notation and description have been made to aid in a quick understanding of the method.

The derivation of nonlinear normal modes begins with an original system of N coupled,

second-order differential equations. They must be written in the form of Eq. (3.1) or must be transformed to this form.

$$\ddot{x}_i = f_i [x_1, x_2, \dots, x_N, \dot{x}_1, \dot{x}_2, \dots, \dot{x}_N] \quad (3.1)$$

The N second-order equations are then transformed to $2N$ first-order differential equations.

$$\begin{aligned} \dot{x}_i &= y_i \\ \dot{y}_i &= f_i [x_1, x_2, \dots, x_N, y_1, y_2, \dots, y_N] \end{aligned} \quad (3.2)$$

One of the x_i - y_i coordinate pairs must be chosen as the master coordinate on which the nonlinear normal modes are constructed. Pair one is chosen for convenience of notation, but any of the pairs can be chosen.

$$\begin{aligned} x_1 &= u \\ y_1 &= v \end{aligned} \quad (3.3)$$

The modal degrees of freedom are denoted here as u and v . The remaining system degrees of freedom are slaved to the master modal coordinates by a rule for modal motion.

$$\begin{aligned} x_i &= X_i[u, v] \\ y_i &= Y_i[u, v] \end{aligned} \quad (3.4)$$

In the case of linear normal modes, only a linear relationship would exist between the master and slave coordinates; however, for nonlinear normal modes, the relationship is considered to be of a general nonlinear form. To create an asymptotic approximation of the nonlinear normal modes, $X_i[u, v]$ and $Y_i[u, v]$ are expanded as a Taylor series in two variables to the

desired order of the approximation.

$$\begin{aligned} X_i[u, v] &= a_{1i}u + a_{2i}v + a_{3i}u^2 + a_{4i}uv + a_{5i}v^2 + \dots \\ Y_i[u, v] &= b_{1i}u + b_{2i}v + b_{3i}u^2 + b_{4i}uv + b_{5i}v^2 + \dots \end{aligned} \quad (3.5)$$

The a 's and b 's are unknown coefficients. The first step in solving for the unknown coefficients is to take the derivative of Eq. (3.4).

$$\begin{aligned} \dot{x}_i &= \frac{\partial X_i}{\partial u} \dot{u} + \frac{\partial X_i}{\partial v} \dot{v} \\ \dot{y}_i &= \frac{\partial Y_i}{\partial u} \dot{u} + \frac{\partial Y_i}{\partial v} \dot{v} \end{aligned} \quad (3.6)$$

The equations of motion, Eq. (3.2), are used to substitute for \dot{x}_i and \dot{y}_i .

$$\begin{aligned} y_i &= \frac{\partial X_i}{\partial u} \dot{u} + \frac{\partial X_i}{\partial v} \dot{v} \\ f_i[x_1, x_2, \dots, x_N, y_1, y_2, \dots, y_N] &= \frac{\partial Y_i}{\partial u} \dot{u} + \frac{\partial Y_i}{\partial v} \dot{v} \end{aligned} \quad (3.7)$$

Since $\dot{u} = \dot{x}_1 = y_1 = v$ and $\dot{v} = \dot{y}_1 = f_1[x_1, \dots, x_N, y_1, \dots, y_N]$, Eq. (3.7) can be rewritten as

$$\begin{aligned} y_i &= \frac{\partial X_i}{\partial u} v + \frac{\partial X_i}{\partial v} f_1[x_1, x_2, \dots, x_N, y_1, y_2, \dots, y_N] \\ f_i[x_1, x_2, \dots, x_N, y_1, y_2, \dots, y_N] &= \frac{\partial Y_i}{\partial u} v + \frac{\partial Y_i}{\partial v} f_1[x_1, x_2, \dots, x_N, y_1, y_2, \dots, y_N]. \end{aligned} \quad (3.8)$$

The remaining x_1 's and y_1 's are replaced by u and v and the x_i 's and y_i 's are replaced by $X_i[u, v]$ and $Y_i[u, v]$.

$$\begin{aligned} Y_i[u, v] &= \frac{\partial X_i}{\partial u} v + \frac{\partial X_i}{\partial v} f_1[u, X_2[u, v], \dots, X_N[u, v], v, Y_2[u, v], \dots, Y_N[u, v]] \\ f_i[u, X_2[u, v], \dots, X_N[u, v], v, Y_2[u, v], \dots, Y_N[u, v]] &= \frac{\partial Y_i}{\partial u} v + \frac{\partial Y_i}{\partial v} f_1[u, X_2[u, v], \dots, X_N[u, v], v, Y_2[u, v], \dots, Y_N[u, v]] \end{aligned} \quad (3.9)$$

The above equations are polynomials in u and v with coefficients composed of combinations

of the unknown a and b coefficients from Eq. (3.5). The form is like

$$\sum_{i=0}^{z_o} \sum_{j=0}^{(z_o)-i} C_{ij} u^i v^j = 0, \quad C_{00} = 0. \quad (3.10)$$

Here z is the order of the nonlinear modal approximation in Eq. (3.5) and o the order of the nonlinearities of the system from Eq. (3.1). The C_{ij} terms are composed of unknown a and b coefficients. At this point, one of several options may be chosen to solve for the unknown coefficients. For this derivation, the asymptotic method is used because it is the simplest and most common. New solution methods were developed and will be presented later in this chapter.

For the asymptotic method, the only terms from Eq. (3.10) retained are ones in which $(i + j)$ is less than or equal to the order of the modal approximation z . The higher order terms are not accounted for in the solution leading to the possibility of inaccuracies.

$$\sum_{i=0}^z \sum_{j=0}^{z-i} C_{ij} u^i v^j + H.O.T. = 0, \quad C_{00} = 0 \quad (3.11)$$

The C_{ij} 's are extracted and set equal to zero creating a system of equations in a and b .

$$C_{ij} = 0, \quad (i + j) \leq z \quad (3.12)$$

This system is nonlinear in the unknown a and b coefficients and gives multiple solutions. The coefficients can be solved for in groups associated with the combined polynomial order $(i + j)$. Referring back to Eq. (3.5), the linear coefficients a_{1i} , a_{2i} , b_{1i} , and b_{2i} can be solved as a set followed by the quadratic coefficients a_{3i} , a_{4i} , a_{5i} , b_{3i} , b_{4i} , and b_{5i} , and so on. The linear order equations have some real and some complex solutions. Each real solution corresponds to one of the nonlinear modal modes of motion. The complex solutions are meaningless and disregarded. The real solutions can also be obtained from a complex eigenvalue analysis performed on a linearized version of the original system. The eigenvalue method of solving

for these linear coefficients will be shown in the spring-mass-damper example below. Each real solution obtained either from the solution to the linear order equations or the eigenvalue analysis can then be substituted into the higher order coefficient equations. After the substitution, the higher order equations are linear in the unknown coefficients and can be solved easily.

The modes generated with the coefficient solution to the linear order equations are equivalent to the modes obtained from a complex eigenvalue analysis performed on a linearized version of the original system. The eigenvalue method of solving for these linear coefficients will be shown in the spring-mass-damper example below.

With the unknown coefficients now known, the modal rules can be inserted into the equations of motion of the master coordinate. Each set of a and b coefficients create a different nonlinear normal mode. The modal form of the equation will appear in first-order oscillator form as

$$\begin{aligned} \dot{u} &= v \\ \dot{v} &= f_1 [u, X_2[u, v], \dots, X_N[u, v], v, Y_2[u, v], \dots, Y_N[u, v]] \end{aligned} \quad (3.13)$$

or in second-order form

$$\ddot{u} = f_1 [u, X_2 [u, \dot{u}], \dots, X_N [u, \dot{u}], \dot{u}, Y_2 [u, \dot{u}], \dots, Y_N [u, \dot{u}]] . \quad (3.14)$$

This equation can then be used to find the systems behavior in that mode. The modal motion found can be converted back into physical coordinates if desired by using Eqs. (3.3) and (3.4).

3.1.1 Linear Spring-Mass-Damper Example

This section applies the nonlinear normal mode method to a linear three degree of freedom spring-mass-damper problem to demonstrate the method and aid in understanding. It follows the process described in the previous section. The system to be used can be seen in Fig. 3.1.

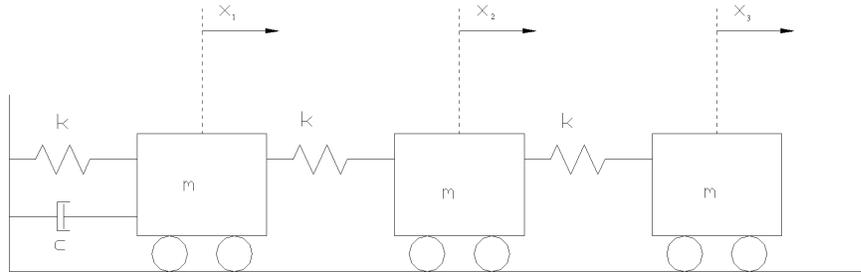


Figure 3.1: Three Degree-of-Freedom Spring-Mass-Damper System

The equations of motion for this system are

$$\begin{aligned}
 m\ddot{x}_1 &= -c\dot{x}_1 + kx_2 - 2kx_1 \\
 m\ddot{x}_2 &= kx_3 - 2kx_2 + kx_1 \\
 m\ddot{x}_3 &= -kx_3 + kx_2.
 \end{aligned}
 \tag{3.15}$$

In these equations, m is the mass of each block, k is the linear spring stiffness of each spring, and c is the damping coefficient. These equations are then converted to first-order form.

$$\begin{aligned}
 \dot{x}_1 &= y_1 \\
 \dot{y}_1 &= f_1 [x_1, x_2, x_3, y_1, y_2, y_3] = -cy_1 + kx_2 - 2kx_1 \\
 \dot{x}_2 &= y_2 \\
 \dot{y}_2 &= f_2 [x_1, x_2, x_3, y_1, y_2, y_3] = kx_3 - 2kx_2 + kx_1 \\
 \dot{x}_3 &= y_3 \\
 \dot{y}_3 &= f_3 [x_1, x_2, x_3, y_1, y_2, y_3] = -kx_3 + kx_2
 \end{aligned}
 \tag{3.16}$$

The master coordinate is chosen to be x_1 - y_1 and the modal motion rules are formed. Since this is a linear system, only the linear expansion is used.

$$\begin{aligned}x_1 &= u \\y_1 &= v\end{aligned}\tag{3.17}$$

$$\begin{aligned}x_2 &= X_2[u, v] = a_1u + a_2v \\y_2 &= Y_2[u, v] = b_1u + b_2v \\x_3 &= X_3[u, v] = c_1u + c_2v \\y_3 &= Y_3[u, v] = d_1u + d_2v\end{aligned}\tag{3.18}$$

The solution for the unknown a , b , c , and d coefficients must be found. The first step is to take the time derivative of Eqs. (3.18).

$$\begin{aligned}\dot{X}_2 &= a_1\dot{u} + a_2\dot{v} \\ \dot{Y}_2 &= b_1\dot{u} + b_2\dot{v} \\ \dot{X}_3 &= c_1\dot{u} + c_2\dot{v} \\ \dot{Y}_3 &= d_1\dot{u} + d_2\dot{v}\end{aligned}\tag{3.19}$$

Substitutions are now made according to Eqs. (3.7), (3.8), and (3.9) to get

$$\begin{aligned}b_1u + (-a_1 + b_2)v - a_2^2kv + a_2(2ku - a_1ku + cv) &= 0 \\ -b_1v + b_2cv + k((1 + 2b_2 - a_1(2 + b_2) + c_1)u + (-a_2(2 + b_2) + c_2)v) &= 0 \\ d_1u + (-c_1 + d_2)v + c_2(cv - k((-2 + a_1)u + a_2v)) &= 0 \\ -c_1ku - a_1(-1 + d_2)ku + 2d_2ku - d_1v + cd_2v + a_2kv - c_2kv - a_2d_2kv &= 0.\end{aligned}\tag{3.20}$$

The coefficients of u and v in each of the four equations are extracted and set equal to zero to form the system below.

$$\begin{aligned}
 2ka_2 - ka_1a_2 + b_1 &= 0 \\
 k - 2ka_1 + 2kb_2 - ka_1b_2 + kc_1 &= 0 \\
 b_1 + 2kc_2 - ka_1c_2 &= 0 \\
 ka_1 + 2kb_2 - ka_1b_2 - kc_1 &= 0 \\
 -a_1 + ca_2 - ka_2^2 + b_2 &= 0 \\
 -2ka_2 - b_1 + cb_2 - ka_2b_2 + kc_2 &= 0 \\
 b_2 - c_1 + cc_2 - ka_2c_2 &= 0 \\
 ka_2 - b_1 + cb_2 - ka_2b_2 - kc_2 &= 0
 \end{aligned} \tag{3.21}$$

The system coefficients must be calculated numerically to solve this system. For simplicity, the mass of each block and all the spring stiffnesses are taken as unity. The damping coefficient is set to 0.3.

$$\begin{aligned}
 2a_2 - a_1a_2 + b_1 &= 0 \\
 1 - 2a_1 + 2b_2 - a_1b_2 + c_1 &= 0 \\
 b_1 + 2c_2 - a_1c_2 &= 0 \\
 a_1 + 2b_2 - a_1b_2 - c_1 &= 0 \\
 -a_1 + 0.3a_2 - a_2^2 + b_2 &= 0 \\
 -2a_2 - b_1 + 0.3b_2 - a_2b_2 + c_2 &= 0 \\
 b_2 - c_1 + 0.3c_2 - a_2c_2 &= 0 \\
 a_2 - b_1 + 0.3b_2 - a_2b_2 - c_2 &= 0
 \end{aligned} \tag{3.22}$$

The solution of these equations results in three sets of real coefficients and twelve complex solutions. The complex solutions are meaningless in the terms the problem was formulated and are discarded. The remaining three sets of real coefficients determine the modes of

motion. The modes created with these coefficients are identical to the modes found through an eigenvalue analysis. The three sets of modal coefficients can be seen below.

$$\begin{array}{rcccc}
 & \text{Mode 1} & \text{Mode 2} & \text{Mode 3} & \\
 a_1 = & -1.211 & 0.435 & 1.801 & \\
 a_2 = & 0.1982 & 0.1341 & 0.268 & \\
 b_1 = & -0.636 & -0.210 & -0.0533 & \\
 b_2 = & -1.231 & 0.413 & 1.792 & (3.23) \\
 c_1 = & 0.531 & -0.776 & 2.25 & \\
 c_2 = & -0.1146 & -0.01014 & 0.424 & \\
 d_1 = & 0.368 & 0.01586 & -0.0844 & \\
 d_2 = & 0.542 & -0.774 & 2.23 &
 \end{array}$$

The modal rules can now be fully defined for each mode of motion. Any mode calculated above can be substituted into the first equation of motion to derive the corresponding modal equation. The subscripts in Eq. (3.24) refer to the modal degree of freedom.

$$\begin{array}{r}
 \dot{u}_1 = v_1 \\
 \dot{v}_1 = -3.21u_1 - 0.1018v_1 \\
 \dot{u}_2 = v_2 \\
 \dot{v}_2 = -1.565u_2 - 0.1659v_2 \\
 \dot{u}_3 = v_3 \\
 \dot{v}_3 = -0.1991u_3 - 0.0323v_3
 \end{array} \tag{3.24}$$

In second-order form, these equations are

$$\begin{array}{r}
 \ddot{u}_1 = -3.21u_1 - 0.1018\dot{u}_1 \\
 \ddot{u}_2 = -1.565u_2 - 0.1659\dot{u}_2 \\
 \ddot{u}_3 = -0.1991u_3 - 0.0323\dot{u}_3.
 \end{array} \tag{3.25}$$

This is exactly the same result that is found by traditional linear modal decomposition. These modal equations can now be simulated or otherwise analyzed to determine the system's behavior in the modes.

3.1.2 Alternative Eigenvalue Solution to Linear Coefficients

When using the asymptotic method to solve for the unknown modal coefficients, the equations used to solve for the linear coefficients are nonlinear. These equations can be solved for a simple system in a short time, but as the complexity of the system increases the time required to solve these equations grows rapidly. For example, with three bending and three torsion mode shapes for the beam model presented later, the nonlinear equation solver included in Mathematica did not give the solution within two hours. However, the linear modal coefficients can be found with an eigenvalue solution of the linearized system. The eigenvalue solution to the linear coefficients is also used as the first step in the Galerkin and collocation solution methods presented in this dissertation.

Starting with the linearized system written in second-order matrix form

$$[M] \{\ddot{q}_i\} + [C] \{\dot{q}_i\} + [K] \{q_i\} = 0, \quad (3.26)$$

the first-order stiffness matrix is formed, where $[0]$ and $[I]$ are zero and identity matrices of the correct size.

$$A = \begin{bmatrix} [0] & [I] \\ -M^{-1}K & -M^{-1}C \end{bmatrix} \quad (3.27)$$

For a first-order system, the A matrix would be known directly. The eigenvectors of A are found and written column wise defining a modal matrix Z . Each column (eigenvector) of Z is normalized by the component corresponding to the desired master coordinate creating Z^* . From here, a transformation matrix is desired that would transform the original system matrix A into block diagonal of oscillator equations. This is achieved through a matrix W

which is composed of the complex conjugate pairs of the eigenvalues λ_i and λ_i^* .

$$W = \text{BlockDiagonal} \left[\dots \begin{pmatrix} 1 & 1 \\ \lambda_i & \lambda_i^* \end{pmatrix} \dots \right] \quad (3.28)$$

The transformation matrix $U = Z^*W^{-1}$ will transform the A matrix to the block diagonal first-order oscillator form just like the first-order modal equation, Eq. (3.13), in the NNM derivation. Each set of two columns in the matrix U corresponds to a modal solution.

The three degree of freedom, spring-mass-damper system from Fig.3.1 and Eq. (3.15) is used here as an example of this process. In second-order matrix form Eq. (3.15) becomes

$$\begin{pmatrix} 1 & 0 & 0 \\ 0 & 1 & 0 \\ 0 & 0 & 1 \end{pmatrix} \begin{pmatrix} \ddot{x}_1 \\ \ddot{x}_2 \\ \ddot{x}_3 \end{pmatrix} + \begin{pmatrix} 0.3 & 0 & 0 \\ 0 & 0 & 0 \\ 0 & 0 & 0 \end{pmatrix} \begin{pmatrix} \dot{x}_1 \\ \dot{x}_2 \\ \dot{x}_3 \end{pmatrix} + \begin{pmatrix} 2 & -1 & 0 \\ -1 & 2 & -1 \\ 0 & -1 & 1 \end{pmatrix} \begin{pmatrix} x_1 \\ x_2 \\ x_3 \end{pmatrix} = \begin{pmatrix} 0 \\ 0 \\ 0 \end{pmatrix}. \quad (3.29)$$

The first-order system matrix is then easily computed.

$$A = \begin{pmatrix} 0 & 0 & 0 & 1 & 0 & 0 \\ 0 & 0 & 0 & 0 & 1 & 0 \\ 0 & 0 & 0 & 0 & 0 & 1 \\ -2 & 1 & 0 & -0.3 & 0 & 0 \\ 1 & -2 & 1 & 0 & 0 & 0 \\ 0 & 1 & -1 & 0 & 0 & 0 \end{pmatrix} \quad (3.30)$$

Finding the eigenvectors of A , the Z matrix is created and normalized by the row corresponding to the first degree-of-freedom which is being used as the master coordinate.

$$Z^* = \begin{pmatrix} 1 & 1 & 1 & 1 & 1 & 1 \\ -1.221 + 0.355i & -1.221 - 0.355i & 0.424 + 0.1674i & 0.424 - 0.1674i & 1.797 + 0.1194i & 1.797 - 0.1194i \\ 0.537 - 0.205i & 0.537 + 0.205i & -0.775 - 0.01266i & -0.775 + 0.01266i & 2.24 + 0.1891i & 2.24 - 0.1891i \\ -0.0509 + 1.791i & -0.0509 - 1.791i & -0.0829 + 1.248i & -0.0829 - 1.248i & -0.01615 + 0.446i & -0.01615 - 0.446i \\ -0.574 - 2.20i & -0.574 + 2.20i & -0.244 + 0.516i & -0.244 - 0.516i & -0.0822 + 0.799i & -0.0822 - 0.799i \\ 0.340 + 0.971i & 0.340 - 0.971i & 0.0801 - 0.966i & 0.0801 + 0.966i & -0.1205 + 0.995i & -0.1205 - 0.995i \end{pmatrix} \quad (3.31)$$

The matrix W is then formulated using the complex conjugate pairs of eigenvalues.

$$W = \begin{pmatrix} 1 & 1 & 0 & 0 & 0 & 0 \\ -0.0509 + 1.791i & -0.0509 - 1.791i & 0 & 0 & 0 & 0 \\ 0 & 0 & 1 & 1 & 0 & 0 \\ 0 & 0 & -0.0829 + 1.248i & -0.0829 - 1.248i & 0 & 0 \\ 0 & 0 & 0 & 0 & 1 & 1 \\ 0 & 0 & 0 & 0 & -0.01615 + 0.446i & -0.01615 - 0.446i \end{pmatrix} \quad (3.32)$$

Finally the transformation matrix, U is found.

$$U = \begin{pmatrix} 1 & 0 & 1 & 0 & 1 & 0 \\ -1.211 & 0.1982 & 0.435 & 0.1341 & 1.801 & 0.268 \\ 0.531 & -0.1146 & -0.776 & -0.01014 & 2.25 & 0.424 \\ 0 & 1 & 0 & 1 & 0 & 1 \\ -0.636 & -1.231 & -0.210 & 0.413 & -0.0533 & 1.792 \\ 0.368 & 0.542 & 0.01586 & -0.774 & -0.0844 & 2.23 \end{pmatrix} \quad (3.33)$$

If the first-order system matrix is transformed with this matrix, $U^{-1}AU$, the first-order oscillator form would result.

$$A^* = \begin{pmatrix} 0 & 1 & 0 & 0 & 0 & 0 \\ -3.21 & -0.1018 & 0 & 0 & 0 & 0 \\ 0 & 0 & 0 & 1 & 0 & 0 \\ 0 & 0 & -1.565 & -0.1659 & 0 & 0 \\ 0 & 0 & 0 & 0 & 0 & 1 \\ 0 & 0 & 0 & 0 & -0.1991 & -0.0323 \end{pmatrix} \quad (3.34)$$

Now referring back to the modal definition equation from the NNM derivation, Eq. (3.5), it

can be deciphered that the matrix U is of the form

$$U = \begin{pmatrix} 1 & 0 & 1 & 0 & 1 & 0 \\ a_{1,1} & a_{2,1} & a_{1,2} & a_{2,2} & a_{1,3} & a_{2,3} \\ c_{1,1} & c_{2,1} & c_{1,2} & c_{2,2} & c_{1,3} & c_{2,3} \\ 0 & 1 & 0 & 1 & 0 & 1 \\ b_{1,1} & b_{2,1} & b_{1,2} & b_{2,2} & b_{1,3} & b_{2,3} \\ d_{1,1} & d_{2,1} & d_{1,2} & d_{2,2} & d_{1,3} & d_{2,3} \end{pmatrix}, \quad (3.35)$$

where the second index on the coefficients corresponds to the mode. Referring back to the previous example, the pairs of columns in the U transformation matrix correspond to three modal solutions seen in Eq. (3.23).

3.1.3 Linear Normal Mode (LNM) Solution

Throughout this dissertation the results for nonlinear normal mode (NNM) solutions are compared to a linear normal mode (LNM) solution. The LNM solution is a simplification of the NNM solution. The nonlinear modal approximation function from Eq. (3.5) is simplified to a linear modal approximation function.

$$\begin{aligned} X_i[u, v] &= a_{1i}u + a_{2i}v \\ Y_i[u, v] &= b_{1i}u + b_{2i}v \end{aligned} \quad (3.36)$$

The rest of the process for generating the NNM is followed with this simplified modal approximation. This results in a model that captures the nonlinearity in the master coordinate, but with only linear coupling between the modes.

3.2 First-Order Formulation

Two systems encountered in the work for this dissertation could not be transformed to conform to the standard formulation of nonlinear normal modes currently in literature. In the first instance, using unsteady aerodynamics with the pitch-plunge airfoil created a system with two second-order and two first-order differential equations. Obviously, this system could be transformed into six first-order differential equations, but cannot be written in a second-order form. The second instance was discovered during a study on the effect of the master coordinate. When the linear flutter mode was chosen as the master coordinate for the pitch-plunge airfoil, the system consisted of four coupled, first-order differential equations that could not be transformed back into two coupled, second-order differential equations. Published methods only allow for a set of second-order differential equations, Eq. (3.1). Encountering these two cases necessitated deriving a formulation of NNM for a system of coupled, first-order equations. As such, this derivation starts with a system of the form

$$\dot{x}_i = f_i[x_1, x_2, \dots, x_N]. \quad (3.37)$$

Two master coordinates are chosen and the remaining coordinates are slaved to the master coordinates.

$$x_j = u \quad (3.38)$$

$$x_k = v$$

$$x_i = X_i[u, v] \quad i \neq j, k \quad (3.39)$$

A two variable Taylor series is then assumed for the modal relationship with unknown coefficients a_{mi} , where m is the number of terms in the Taylor series.

$$X_i[u, v] = a_{1i}u + a_{2i}v + a_{3i}u^2 + a_{4i}uv + a_{5i}v^2 + \dots \quad i \neq j, k \quad (3.40)$$

To solve for the unknown coefficients, the time derivative of Eq. (3.39) is taken.

$$\dot{x}_i = \frac{\partial X_i}{\partial u} \dot{u} + \frac{\partial X_i}{\partial v} \dot{v} \quad i \neq j, k \quad (3.41)$$

Using Eq. (3.38), \dot{x}_j and \dot{x}_k are substituted for \dot{u} and \dot{v} , respectively.

$$\dot{x}_i = \frac{\partial X_i}{\partial u} \dot{x}_j + \frac{\partial X_i}{\partial v} \dot{x}_k \quad i \neq j, k \quad (3.42)$$

Then using the equations of motion, Eq. (3.37), \dot{x}_i , \dot{x}_j , and \dot{x}_k are replaced.

$$f_i [x_1, \dots, x_N] = \frac{\partial X_i}{\partial u} f_j [x_1, \dots, x_N] + \frac{\partial X_i}{\partial v} f_k [x_1, \dots, x_N] \quad i \neq j, k \quad (3.43)$$

Finally, the rules for modal motion, Eqs. (3.39) and (3.40), are used to get the final form of the equations.

$$\begin{aligned} & f_i [u, v, X_i[u, v], \dots, X_n[u, v]] \\ & - \left(\frac{\partial X_i[u, v]}{\partial u} f_j [u, v, X_i[u, v], \dots, X_n[u, v]] + \frac{\partial X_i[u, v]}{\partial v} f_k [u, v, X_i[u, v], \dots, X_n[u, v]] \right) = 0 \\ & i \neq j, k \end{aligned} \quad (3.44)$$

The unknown coefficients can be found from these equations with the asymptotic method as previously presented. Eq. (3.44) can also be treated as a residual equation for the approximate nonlinear normal mode and a weighted residual type method can be used to solve for the coefficients. Two such methods are developed in the next two sections.

3.3 Galerkin Modal Coefficient Solution

The asymptotic solution method for the unknown modal coefficients presented as part of the second-order NNM derivation is only accurate for weakly nonlinear systems and a limited

amplitude range. The asymptotic method cannot be trusted for a system with a relatively large amplitude. In fact, if the amplitude grows too large, the asymptotically generated modes will become unstable. The unstable modes exhibit a divergent solution and fail to capture LCO. In aeroelastic LCO, the amplitude of the motion increases when the velocity is increased which creates a problem with the asymptotic solution at higher velocities. Additionally, no method exists for determining the error of the asymptotic method without knowing the exact solution and increasing the order of the approximation function will not necessarily improve the results[34][37]. In an attempt to alleviate these deficiencies in the asymptotic method and improve the results obtained herein, a Galerkin based solution was attempted. The Galerkin method is a weighted residual method that drives a weighted average of the approximation function's error to zero over a specified domain. Pesheck et al.[37] transformed their system into an amplitude and phase domain to formulate a Galerkin based solution to the modal coefficients. A combination polynomial and transcendental modal relation was used and good results were obtained. A simpler, more direct version of the Galerkin solution was attempted here which applied the Galerkin method in the same domain and with the same modal relationship as the asymptotic method. Remaining in the same domain facilitated comparisons between the different coefficient solution methods.

The process is presented here using the second-order equations, but an exact parallel exists for Eq. (3.44) in the first-order derivation. Starting with Eq. (3.9) from the second-order derivation, all terms are moved to one side and the result is treated as a residual equation.

$$\begin{aligned}
 R_{1i} &= Y_i(u, v) - \left(\frac{\partial X_i}{\partial u} v + \frac{\partial X_i}{\partial v} f_1(u, X_2(u, v), \dots, X_N(u, v), v, Y_2(u, v), \dots, Y_N(u, v)) \right) \\
 R_{2i} &= f_i(u, X_2(u, v), \dots, X_N(u, v), v, Y_2(u, v), \dots, Y_N(u, v)) \\
 &\quad - \left(\frac{\partial Y_i}{\partial u} v + \frac{\partial Y_i}{\partial v} f_1(u, X_2(u, v), \dots, X_N(u, v), v, Y_2(u, v), \dots, Y_N(u, v)) \right)
 \end{aligned} \tag{3.45}$$

The Galerkin approach has the advantage that all the terms in this equation can be considered as it does not have to be truncated at the order of the approximation as in the asymptotic

method.

The modal expansions from Eq. (3.5) are considered to be of the form

$$\begin{aligned} X_i[u, v] &= \sum_{j=1}^n a_{j,i} \phi_j[u, v] \\ Y_i[u, v] &= \sum_{j=1}^n b_{j,i} \phi_j[u, v]. \end{aligned} \tag{3.46}$$

Here the $\phi_j[u, v]$ shape functions could be chosen as any appropriate set. For this study, the shapes were kept identical to the polynomial set used in the asymptotic formulation for an easier and more direct comparison between the asymptotic and Galerkin solutions. Note that the first two coefficients in each expansion correspond to the linear order solution and can be found exactly by the eigenvalue method. Consequently, there are two choices: 1) the Galerkin integral can be used to solve for all the coefficients; or 2) the linear coefficients can be found with the eigenvalue method and then the Galerkin integral can be used to solve for just the coefficients of nonlinear order. Using the eigenvalue method has two main advantages. The linear portion of the solution will be exact and the solution of the coefficients from the result of the Galerkin integrals will be much simpler. Given these advantages, the eigenvalue-Galerkin combination was always used here. As such, the Galerkin integrals are formed where S_{UV} is the region of interest for the u and v modal variables and n is the number of terms in the modal approximation function.

$$\begin{aligned} G_{1,j} &= \int \int_{S_{UV}} \phi_j[u, v] R_{1,j} du dv \\ G_{2,j} &= \int \int_{S_{UV}} \phi_j[u, v] R_{2,j} du dv, \quad \text{for } j = \{3, 4, \dots, n\} \end{aligned} \tag{3.47}$$

The region S_{UV} must be selected appropriately. If the region is too small, the LCO may lie outside the region, providing no guarantee of accuracy. On the other hand, if it is too large, the accuracy of the LCO solution will degrade due to the large area over which the error must be averaged. To pick a good region size, the asymptotic solution was used

to guess the motion's amplitude. The equations resulting from the Galerkin integrals are used to solve for the unknown nonlinear coefficients; however, unlike the asymptotic method these equations are nonlinear and computationally intensive to both derive and solve. Even for the quasi-steady pitch-plunge airfoil system, the Galerkin method took several orders of magnitude more time than the asymptotic method to arrive at a solution for the coefficients, 558 vs. 0.172 seconds for each nonlinear normal mode. Additionally, in Pesheck et al.[37], a supercomputer was necessary to solve for the modal coefficients in their version of the Galerkin solution. This method was used to solve some problems; however, more work in the computational implementation is needed for the Galerkin method to be applicable to real or even relatively simple problems.

3.4 Collocation Modal Coefficient Solution

The best method for solving for the modal coefficients attempted was the collocation method. Like the Galerkin method, the collocation solution considers all the terms from the residual equation, the error can be reduced by increasing the order of the approximation, and the modes generated remain stable even at very large amplitudes, filling deficiencies of the asymptotic method. Both the Galerkin and collocation solutions are weighted residual methods. The Galerkin method uses the shape functions as the weights while the collocation uses Dirac's delta function. While the Galerkin method sets the weighted average residual over a region of interest equal zero, the collocation method forces the residual to zero at specific points in the domain. This is ideally suited to steady state LCO since it occurs on a single path where accuracy is desired and points can be selected. Away from LCO path the accuracy of the solution is unimportant unless accurate information about the growth of the motion is desired.

The eigenvalue method is again used for the solution to the linear coefficients. A set of points where solution accuracy is desired must be chosen in the u and v domain. When the dirac delta function is used as the weight in the residual integral, the result simply substitutes

this chosen set of u_i and v_i points into the residual equations, Eq. (3.45) (or Eq. (3.44) for the first-order version).

$$\begin{aligned}
 R_{1,i,j} &= Y_i(u_j, v_j) - \left(\frac{\partial X_i}{\partial u} v_j + \frac{\partial X_i}{\partial v} f_1(u_j, X_2(u_j, v_j), \dots, X_N(u_j, v_j), v_j, Y_2(u_j, v_j), \dots, Y_N(u_j, v_j)) \right) \\
 R_{2,i,j} &= f_i(u_j, X_2(u_j, v_j), \dots, X_N(u_j, v_j), v_j, Y_2(u_j, v_j), \dots, Y_N(u_j, v_j)) \\
 &\quad - \left(\frac{\partial Y_i}{\partial u} v_j + \frac{\partial Y_i}{\partial v} f_1(u_j, X_2(u_j, v_j), \dots, X_N(u_j, v_j), v_j, Y_2(u_j, v_j), \dots, Y_N(u_j, v_j)) \right)
 \end{aligned} \tag{3.48}$$

These equations can then be solved for the remaining nonlinear modal coefficients. The solution to these equations take on the same order of time as the asymptotic solution, both of which are much faster than the Galerkin solution

The main difficulty with the collocation method, especially in two-dimensions as it must be used here, is the selection of the points where the residual is forced to zero. Based on the type of nonlinearities, certain symmetries may be exploited. Through a study of the form of the residual equations, Eq. (3.45), it was found that for cubic stiffening the first and third quadrants are antisymmetric and the second and fourth quadrants are antisymmetric. As such, points chosen in the first and second quadrants will force the corresponding points in the other quadrants to be zero as well. However, there is still not a good way to pick the points since the amplitude and shape of the motion are not known *a priori*. Since the amplitude and shape must be known to select a good set of points, an asymptotic solution was completed first. A set of equally spaced points in two adjacent quadrants was selected from the asymptotic solution for the u_i and v_i points necessary for collocation solution.

Chapter 4

Physical Models

This chapter provides details on the physical models considered in this work. To achieve a series of objectives, four different models were considered. The first model was a spring-mass-damper (SMD) system with two degrees of freedom and a nonlinear Van der Pol oscillator style damping term[41]. Since limit cycle oscillation (LCO) had not previously been modeled with nonlinear normal modes (NNM), the SMD model was used as an initial test to prove that the NNM method was capable of capturing LCO. Additionally, the system's parameters were varied to study the effect on NNM solution accuracy. The second and most frequently utilized model was a nonlinear variation of the classic pitch-plunge airfoil model that appears extensively in aeroelasticity literature. This model had quasi-steady aerodynamics and a nonlinear pitch stiffness. The quasi-steady, pitch-plunge model was used to accomplish many objectives of the dissertation including modeling of aeroelastic LCO with NNM, studying the effect of the NNM's master coordinate, and accuracy improvements of multiple modal coefficient solution methods. The same pitch-plunge airfoil structure was also coupled with an unsteady aerodynamic model. The unsteady version's main purpose was to adapt the NNM process to deal with the addition of nonstructural, first-order aerodynamic degrees of freedom. The final model considered was an adaptation of the Goland wing model. The Goland wing was coupled with a nonlinear, quasi-steady aerodynamic model. The beam model chiefly allowed the exploration of a more realistic system with many degrees of freedom

and the effect of inclusion or exclusion of additional modal degrees of freedom. Although not of primary importance, this model also demonstrated aerodynamic nonlinearities.

4.1 Two Degree-of-Freedom Van der Pol Style Oscillator

In all the papers found about nonlinear normal modes to date, the only applications were in structural dynamics with nonlinear stiffnesses. Before any more complex aeroelastic systems were analyzed a simple system that would experience a limit cycle oscillation was sought. The system chosen was a nonlinear, two degree-of-freedom, spring-mass-damper as seen in Fig. 4.1. The left hand spring can be nonlinear by assigning a value to g . The damper is made nonlinear by a Van der Pol-like damping term. This is different from the standard Van der Pol oscillator because it has two degrees of freedom so a normal mode can be defined. The equations of motion for this system are

$$\begin{aligned}\ddot{x}_1 &= -(2k + gx_1^2)x_1 + kx_2 - (c + \mu x_1^2)\dot{x}_1 \\ \ddot{x}_2 &= kx_1 - 2kx_2.\end{aligned}\tag{4.1}$$

In these equations, x_1 and x_2 are the degrees of freedom for the masses, k is the linear spring stiffness, g is cubic nonlinear spring stiffness, c is the primary damping term, μ is the nonlinear damping coefficient, and each overdot represents a time derivative.

4.2 Nonlinear Pitch-Plunge Airfoil with Quasi-Steady Aerodynamics

The first aeroelastic model considered in this dissertation is a nonlinear variation of the classic pitch-plunge airfoil as seen in Fig. 4.2. The non-dimensional equations of motion for

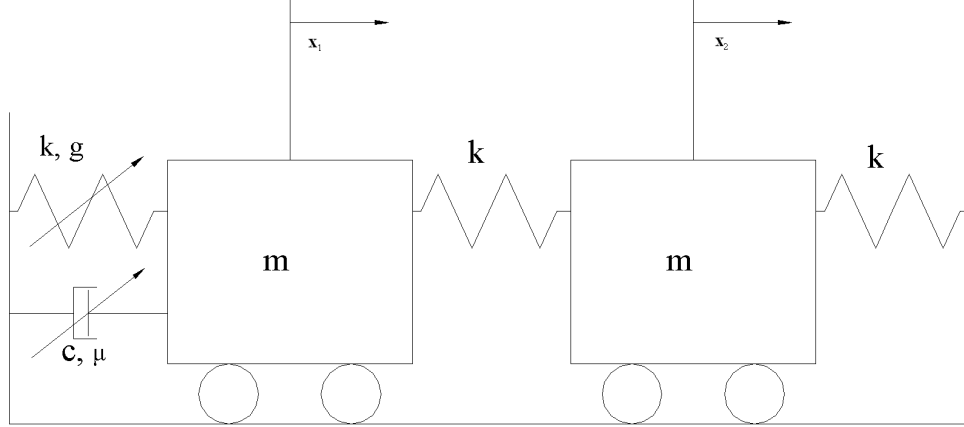


Figure 4.1: Nonlinear Spring-Mass-Damper

the pitch-plunge airfoil are

$$\begin{aligned}
 \ddot{h} + x_\alpha \ddot{\alpha} + \bar{\omega}^2 \bar{h} &= -\bar{L} \\
 x_\alpha \ddot{h} + r_\alpha^2 \ddot{\alpha} + r_\alpha^2 (1 + G_\alpha \alpha^2) \alpha &= \bar{M}
 \end{aligned}
 \tag{4.2}$$

These equations only differ from the classic equations that appear in Bisplinghoff et al. [42] by the dimensionless, nonlinear stiffness term G_α . The variables in Eqs. (4.2) and Fig. 4.2 are as follows: \bar{h} is the nondimensional plunge which is the plunge displacement h divided by the half chord b , α is the pitch, I_α is the pitch inertia, m is the mass, x_α is the dimensionless static imbalance, $K_\alpha[\alpha] = k_\alpha(1 + G_\alpha \alpha^2)$, $\bar{\omega}$ is the plunge-pitch natural frequency ratio $\frac{\omega_h}{\omega_\alpha}$ where $\omega_h = \sqrt{\frac{K_h}{m}}$ and $\omega_\alpha = \sqrt{\frac{k_\alpha}{I_\alpha}}$, r_α is the dimensionless radius of gyration $\sqrt{\frac{I_\alpha}{mb^2}}$, and an overdot represents a time derivative. The nondimensional lift and moment appear as \bar{L} and \bar{M} .

The aerodynamic lift and moment were modeled with Theodorsen's lift and moment

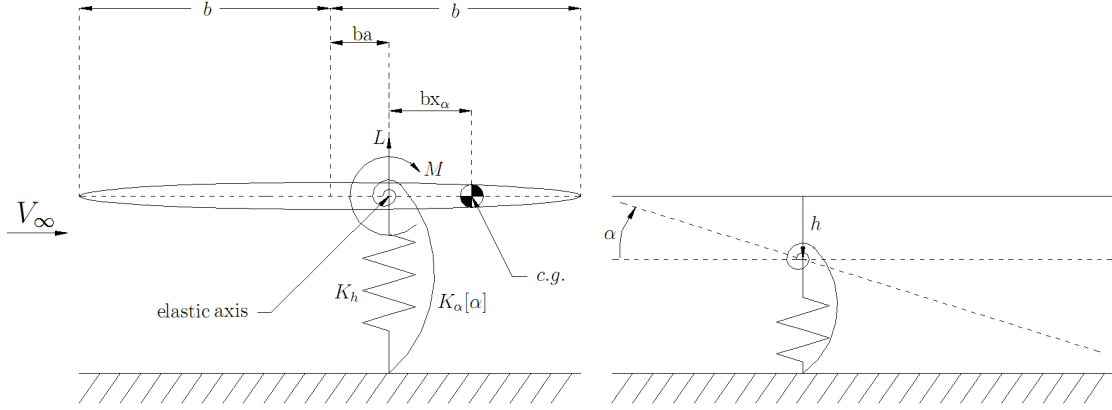


Figure 4.2: Pitch-Plunge Airfoil Model

equations[43].

$$\begin{aligned}
 \bar{L} &= \frac{1}{\mu} \left(\ddot{h} + \bar{u}\dot{\alpha} - a\ddot{\alpha} + 2\bar{u}C[k] \left(\dot{h} + \bar{u}\alpha + \left(\frac{1}{2} - a \right) \dot{\alpha} \right) \right) \\
 \bar{M} &= \frac{1}{\mu} \left(a\ddot{h} - \left(\frac{1}{2} - a \right) \bar{u}\dot{\alpha} - \left(\frac{1}{8} + a^2 \right) \ddot{\alpha} \right) + 2\bar{u}\frac{1}{\mu} \left(\frac{1}{2} + a \right) C[k] \left(\dot{h} + \bar{u}\alpha + \left(\frac{1}{2} - a \right) \dot{\alpha} \right)
 \end{aligned}
 \tag{4.3}$$

In these equations \bar{u} is the dimensionless freestream velocity, a is the elastic axis location, $C[k]$ is Theodorsen's function, and μ is the density ratio. For quasi-steady aerodynamics, $C[k]$ is set to unity. The resulting quasi-steady aeroelastic system is directly compatible with the NNM method and no further manipulation is required.

4.3 Nonlinear Pitch-Plunge Airfoil with Unsteady Aerodynamics

The pitch-plunge airfoil was also considered with unsteady aerodynamics. The same equations from the quasi-steady model, Eqs. (4.2) and (4.3), are used except $C[k]$ is not set to unity. For unsteady aerodynamics, $C[k]$ is in the frequency domain which is not compatible with the NNM method which requires analytic, time domain equations. To facilitate the nonlinear normal mode method the lift and moment were rewritten as

$$\begin{aligned}\bar{L} &= \frac{1}{\mu} \left(\ddot{h} + \bar{u}\dot{\alpha} - a\ddot{\alpha} + 2\bar{u}L_c \right) \\ \bar{M} &= \frac{1}{\mu} \left(a\ddot{h} - \left(\frac{1}{2} - a \right) \bar{u}\dot{\alpha} - \left(\frac{1}{8} + a^2 \right) \ddot{\alpha} \right) + 2\bar{u}\frac{1}{\mu} \left(\frac{1}{2} + a \right) L_c \\ L_c &= C[k] \left(\dot{h} + \bar{u}\alpha + \left(\frac{1}{2} - a \right) \dot{\alpha} \right).\end{aligned}\tag{4.4}$$

Venkatesan and Freidmann [44] developed approximate transfer functions representing Theodorsen's function through the use of Bode plots. Using two zeros and poles, Theodorsen's function can be written as

$$C[k] = \frac{0.5(ik + 0.135)(ik + 0.651)}{(ik + 0.0965)(ik + 0.4555)}.\tag{4.5}$$

The paper showed very good agreement between the transfer function and the exact Theodorsen's equations.

To model L_c , the transfer function was nondimensionalized and then converted to a

state space model with two states. The state space model can be written as

$$\begin{aligned} \begin{Bmatrix} \dot{x}_3 \\ \dot{x}_4 \end{Bmatrix} &= \bar{u} \begin{bmatrix} -0.0965 & 0.08676 \\ 0 & -0.4555 \end{bmatrix} \begin{Bmatrix} x_3 \\ x_4 \end{Bmatrix} + \sqrt{\bar{u}} \begin{bmatrix} 0.09811 \\ 0.2211 \end{bmatrix} \left(\dot{\bar{h}} + \bar{u}\alpha + \left(\frac{1}{2} - a\right) \dot{\alpha} \right) \\ L_c &= \sqrt{\bar{u}} \begin{bmatrix} 0.1962 & 0.4422 \end{bmatrix} \begin{Bmatrix} x_3 \\ x_4 \end{Bmatrix} + 0.5 \left(\dot{\bar{h}} + \bar{u}\alpha + \left(\frac{1}{2} - a\right) \dot{\alpha} \right). \end{aligned} \quad (4.6)$$

The aerodynamic states start at x_3 because x_1 and x_2 are reserved for the modal degrees of freedom of the pitch-plunge airfoil. This state space aerodynamic model was then incorporated into the pitch-plunge airfoil system of two coupled, second-order differential equations to create a system of four equations with two second-order and two first-order differential equations. The full aeroelastic system is

$$\begin{aligned} \ddot{x}_1 + x_\alpha \ddot{x}_2 + \bar{\omega}^2 (1 + G_h x_1^2) x_1 &= -\bar{L} \\ x_\alpha \ddot{x}_1 + r_\alpha^2 \ddot{x}_2 + r_\alpha^2 (1 + G_\alpha x_2^2) x_2 &= \bar{M} \\ \dot{x}_3 &= \bar{u} (-0.0965x_3 + 0.08676x_4) + 0.09811\sqrt{\bar{u}} \left(\dot{x}_1 + \bar{u}x_2 + \left(\frac{1}{2} - a\right) \dot{x}_2 \right) \\ \dot{x}_4 &= -0.4555\bar{u}x_4 + 0.2211\sqrt{\bar{u}} \left(\dot{x}_1 + \bar{u}x_2 + \left(\frac{1}{2} - a\right) \dot{x}_2 \right), \end{aligned} \quad (4.7)$$

where

$$\begin{aligned} \bar{L} &= \frac{1}{\mu} \left(\ddot{x}_1 + \bar{u}\dot{x}_2 - a\ddot{x}_2 + 2\bar{u} \left(\sqrt{\bar{u}} (0.1962x_3 + 0.4422x_4) + 0.5 \left(\dot{x}_1 + \bar{u}x_2 + \left(\frac{1}{2} - a\right) \dot{x}_2 \right) \right) \right) \\ \bar{M} &= \frac{1}{\mu} \left(a\ddot{x}_1 - \left(\frac{1}{2} - a\right) \bar{u}\dot{x}_2 - \left(\frac{1}{8} + a^2\right) \ddot{x}_2 \right) \\ &\quad + 2\bar{u} \frac{1}{\mu} \left(\frac{1}{2} + a\right) \left(\sqrt{\bar{u}} (0.1962x_3 + 0.4422x_4) + 0.5 \left(\dot{x}_1 + \bar{u}x_2 + \left(\frac{1}{2} - a\right) \dot{x}_2 \right) \right). \end{aligned} \quad (4.8)$$

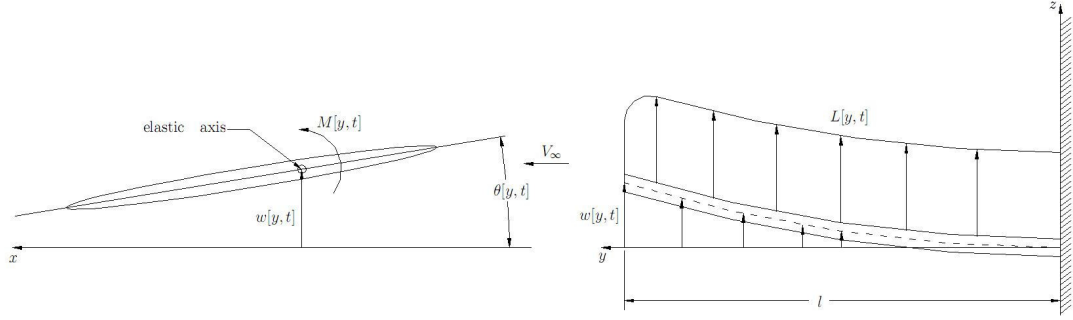


Figure 4.3: Goland Wing Model

4.4 Goland Beam Wing with Nonlinear, Quasi-Steady Aerodynamics

The final model is like the Goland wing model [45]. The Goland wing model is a straight, non-tapered, bending-torsion beam. In this case, the beam wing remains linear and the nonlinearities appear in the aerodynamic model. A diagram of the beam wing model appears in Fig. 4.3.

The equations of motion for the Goland beam wing are

$$\begin{aligned}
 m \frac{\partial^2 w[y, t]}{\partial t^2} - S_y \frac{\partial^2 \theta[y, t]}{\partial t^2} + EI \frac{\partial^4 w[y, t]}{\partial y^4} &= L \\
 I_y \frac{\partial^2 \theta[y, t]}{\partial t^2} - S_y \frac{\partial^2 w[y, t]}{\partial t^2} - GJ \frac{\partial^2 \theta[y, t]}{\partial y^2} &= M.
 \end{aligned} \tag{4.9}$$

In these equations $\theta[y, t]$ is the pitch degree of freedom, $w[y, t]$ is the plunge degree of freedom, m is the mass per unit span, I_y is the moment of inertia in pitch, S_y is the static mass imbalance, EI is the bending stiffness, GJ is the torsional stiffness, and L and M are the lift and moment per unit span. Since the nonlinearities appear in the lift and moment terms L and M , these equations are exactly as they appear in the linear model presented in [42].

For the beam wing, a quasi-steady aerodynamic model with a cubic stall-like nonlin-

earity was used.

$$\begin{aligned}
 L &= \rho V_\infty^2 b C_{l\alpha} (\alpha_e - C_3 \alpha_e^3) \\
 M &= -\rho V_\infty^2 b^2 C_{m\alpha} (\alpha_e - C_3 \alpha_e^3) \\
 \alpha_e &= \theta[y, t] - \frac{1}{V_\infty} \frac{\partial w[y, t]}{\partial t}
 \end{aligned} \tag{4.10}$$

In these equations: ρ is air density, V_∞ is the freestream velocity, α_e is the effective angle of attack, b is the semi-chord of the wing, $C_{l\alpha}$ is the linear lift curve slope 2π , and $C_{m\alpha}$ is the linear moment curve slope $(\frac{1}{2} + a) C_{l\alpha}$. A similar model was used by Kim and Strganac [23], [24] and the value for the nonlinear aerodynamic term $C_3 = .00034189 \left(\frac{180}{\pi}\right)^3 / C_{l\alpha}$ was taken from their papers. The model uses strip theory which implies that two-dimensional aerodynamics is sufficient to model the lift at each span location. Since strip theory does not model wing tip vortices, the aspect ratio of the wing has to be relatively large for the method to be reasonably accurate.

As shown above, the beam model obviously cannot be used with the nonlinear normal modes method presented in the last chapter. The most convenient way to put the beam model in a form where nonlinear normal modes can be applied is to use the assumed modes method with Lagrange's equations. For the assumed modes, a set of orthogonal polynomials that satisfied all the beam's boundary conditions were used. Up to five modes for bending and five modes for torsion were used. The orthogonal polynomials were chosen over the exact beam bending and torsion mode shapes because the polynomials process much faster. The beam bending and torsion can then be written

$$\begin{aligned}
 w[y, t] &= \sum_{i=1}^{N_w} \phi_{wi}[y] \eta_i[t] \\
 \theta[y, t] &= \sum_{i=1}^{N_\theta} \phi_{\theta i}[y] \eta_{(i+N_w)}[t]
 \end{aligned} \tag{4.11}$$

where $\phi_{wi}[y]$ are the orthogonal polynomials for bending, $\phi_{\theta i}[y]$ are the orthogonal polynomials for torsion, $\eta_i[t]$ are the modal degrees of freedom, N_w is the number of bending modes,

and N_θ is the number of torsion modes.

The kinetic and potential energies of the beam are

$$T = \frac{1}{2} \int_0^l \begin{pmatrix} \frac{\partial w[y,t]}{\partial t} & \frac{\partial \theta[y,t]}{\partial t} \end{pmatrix} \begin{pmatrix} m & -S_y \\ -S_y & I_y \end{pmatrix} \begin{pmatrix} \frac{\partial w[y,t]}{\partial t} \\ \frac{\partial \theta[y,t]}{\partial t} \end{pmatrix} dy \quad (4.12)$$

and

$$U = \frac{1}{2} \int_0^l \begin{pmatrix} \frac{\partial^2 w[y,t]}{\partial y^2} & \frac{\partial \theta[y,t]}{\partial y} \end{pmatrix} \begin{pmatrix} EI & 0 \\ 0 & GJ \end{pmatrix} \begin{pmatrix} \frac{\partial^2 w[y,t]}{\partial y^2} \\ \frac{\partial \theta[y,t]}{\partial y} \end{pmatrix} dy \quad (4.13)$$

and the generalized forces are

$$Q_{wi} = \int_0^l \phi_{wi}[y] L dy, \quad \text{for } i = 1, \dots, N_w$$

$$Q_{\theta i} = \int_0^l \phi_{\theta i}[y] M dy, \quad \text{for } i = 1, \dots, N_\theta. \quad (4.14)$$

In these equations, l is the length of the beam and L and M are the lift and moment from the nonlinear, quasi-steady aerodynamic model above. Lagrange's equations of motion can now be written.

$$\frac{\partial}{\partial t} \left(\frac{\partial(T-U)}{\partial \dot{\eta}_i} \right) - \left(\frac{\partial(T-U)}{\partial \eta_i} \right) = Q_{wi}, \quad \text{for } i = 1, \dots, N_w$$

$$\frac{\partial}{\partial t} \left(\frac{\partial(T-U)}{\partial \dot{\eta}_i} \right) - \left(\frac{\partial(T-U)}{\partial \eta_i} \right) = Q_{\theta i}, \quad \text{for } i = 1 + N_w, \dots, N_w + N_\theta \quad (4.15)$$

Lagrange's equations generate a system of $N_w + N_\theta$ nonlinear equations. The mass matrix is linear so it can easily be extracted from the system and the equations can be rewritten as

$$[M] \{\ddot{\eta}_i\} = \{f_i[\{\dot{\eta}_i\}, \{\eta_i\}]\}, \quad \text{for } i = 1, \dots, N_w + N_\theta \quad (4.16)$$

where $[M]$ is the mass matrix and f_i are nonlinear functions of the modal positions and

velocities. This discretized version of the beam wing is now ready for the application of nonlinear normal modes.

Chapter 5

Results

This chapter details the results from using the nonlinear normal mode (NNM) method to predict limit cycle oscillation (LCO) in a series of different systems. Since nonlinear normal modes have not previously been used for modeling of limit cycle oscillation, the first section discusses a simple spring-mass-damper system with a Van der Pol type nonlinear damping term. Linear and nonlinear system parameters were varied to study the effect on the accuracy of the NNM solution. The NNM method was also applied to two pitch-plunge airfoil systems. Sample results are presented for both quasi-steady and unsteady aerodynamics. The results from a study on the effect of changing the NNM master coordinate are included. Improvements gained with Galerkin and collocation solutions for the modal coefficients are also presented. The final section details the results from the NNM method used on a beam wing and demonstrates that modes can be eliminated without a significant loss in accuracy based on the modal coefficient solutions.

Several different solutions are compared in this chapter. All modal solutions are compared to a reference solution which is a fourth-order Runge-Kutta time simulation of each systems exact equations of motion (referred to as “Exact” in tables and plots) . The Runge-Kutta solution was computed with both absolute and relative error goals set to half of machine precision. The same Runge-Kutta scheme was used to simulate the all the modal equations as well. Many of the nonlinear normal mode solutions are compared to a linear

normal mode solution. The linear normal modes are calculated the same way as the nonlinear normal modes except that only the linear terms in the modal approximation function are retained. In figures the linear normal mode solution is denoted as LNM. There are also several different types of nonlinear normal mode solutions presented including: asymptotic nonlinear normal modes (NNM-A), Galerkin nonlinear normal modes (NNM-G), and collocation nonlinear normal modes (NNM-C).

5.1 Two Degree-of-Freedom Van der Pol Style Oscillator

The primary goal of the two degree of freedom system was to show that the nonlinear normal modes could model limit cycle oscillation and to explore possible limitations. Once the ability of the nonlinear normal modes to predict LCO was established, the stiffness and damping parameters and the initial conditions of the system were parametrically varied to see what effect different relative values of linear to nonlinear terms would have on the accuracy of the solution. The accuracy was judged by the amplitudes of the two masses and the frequency of the motion once the final limit cycle oscillation was established. A small modal displacement was used as the initial condition in all cases.

Table 5.1 contains the results from all the cases where LCO was identified. It contains sections for parametric variation of the linear stiffness, the nonlinear stiffness, and linear and nonlinear damping with and without the inclusion of a nonlinear stiffness term. Since the system had two degrees of freedom, two nonlinear normal modes existed and results for both are presented. All results use the first degree-of-freedom as the master coordinate.

Figures 5.1 through 5.8 present the results from two of the cases in the table. The coefficients for these two cases are bolded. The results from these figures will be discussed first followed by a discussion of the rest of the results in table 5.1.

Case 1 is an example of good results and can be see in phase space diagrams in Figs. 5.1 and 5.2 and time histories in Figs. 5.5 and 5.6. Case 1 used $k = 10$, $g = 0.5$, $c = -0.3$, and

$\mu = 0.6$. The phase space diagrams show that there is good agreement between the NNM and the exact simulations once the motion has settled into LCO. Both the amplitude and the shape of the motion match closely. The time history plots further show that the NNM captures the result well during the growth of the motion from a small initial condition.

Case 2 is an example of poor results and can be seen in phase space diagrams in Figs. 5.3 and 5.4 and in time histories in Figs. 5.7 and 5.8. Case 2 used $k = 10$, $g = 0.5$, $c = -0.6$, and $\mu = 0.3$. In this case the phase diagrams show a very poor result on the part of the NNM solution. The amplitudes are in error by a significant percentage and in the case of the x_2 the shape is totally different, especially in the first mode. The time histories show that the NNM solution does a good job until the motion reaches a particular amplitude. This indicates that the nonlinearities in the system have become too strong for the asymptotic solution method. The error gets worse as the amplitude further increases since the strength of the nonlinearity depends on the amplitude.

Variation of the initial condition is not presented in table 5.1 because it was found to have no effect on the accuracy in either mode with one small exception. If the modal displacement for the second mode was increased far enough the physical solution sometimes ended up in the first mode. Since the nonlinear normal modes were approximate, the modal initial conditions were composed of a mixture of the two modes when converted to the physical coordinates and the physical system picked the mode it preferred.

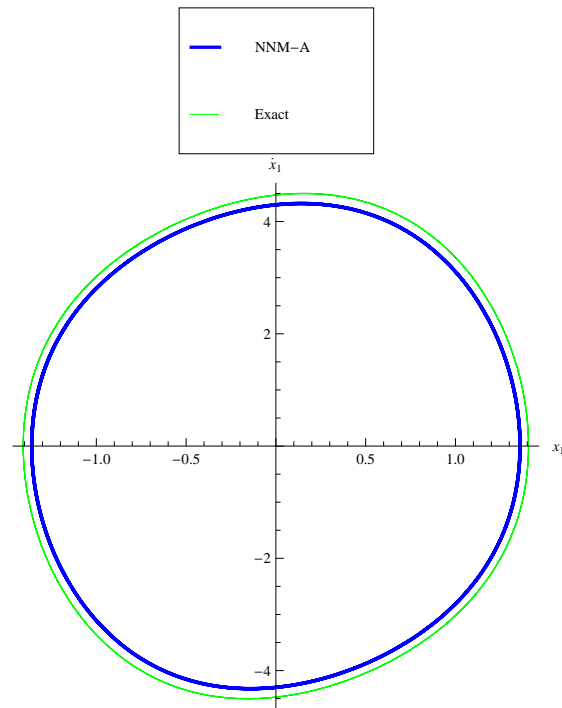
Varying the stiffness and damping parameters did create a few problems not identified in table 5.1. For certain ranges of values, the physical solution would experience what appeared to be chaotic motion. There were other cases where the amplitude varied over time which is indicative of internal resonances in the system. In either of these cases, the nonlinear normal modes are not the correct theoretical tool. In all the cases where the chaotic motion was observed, the nonlinear normal mode exhibited divergent oscillations. In cases with apparent internal resonances, the nonlinear normal mode produced a single an LCO exhibiting a constant amplitude instead of the cyclically varying amplitude of the exact solution.

With a close study of the data in table 5.1, a few trends can be found. In all the cases where a stable LCO was found the frequency results were quite good even if the NNM amplitude was in error by a substantial amount. The first variation shows an increase in the linear stiffness with nonlinearity in damping only. As the linear stiffness increases the error of the NNM solution decreases. The reduction in error can be explained by the reduction in both the nonlinear damping coefficient and the destabilizing linear damping coefficient (damping ratio has stiffness in the denominator). Increasing the nonlinear stiffness produces a proportional increase in the NNM error. This is expected since the asymptotic method is only valid for relatively weak nonlinearities. A nonlinear stiffness greater than ten percent of the linear stiffness results in chaotic motion of this system which obviously cannot be captured by a NNM solution. An increase in the linear damping of the system, making it more unstable at the origin, increases the amplitude and degrades the results of the NNM solution. This leads to the conclusion that a decrease in the linear stability of the system adversely affects the accuracy of the asymptotic NNM solution. In effect, the nonlinear damping term has to work harder to hold the system in LCO which creates a greater relative nonlinearity in the system. An increase in the nonlinear damping term has no measurable effect on the error when the stiffness is linear and actually reduces the error when the stiffness is nonlinear. The increased nonlinear damping does decrease the amplitude of the motion in both cases. In the nonlinear stiffness case, the improvement in results is likely due to the fact that the amplitude is reduced resulting in less nonlinear stiffness effect. As seen before, the nonlinear stiffness quickly increased the error so reducing its effect allows for an improvement in results. Overall, it can be seen that the effect of changing the system parameters would be quite difficult to predict *a priori*.

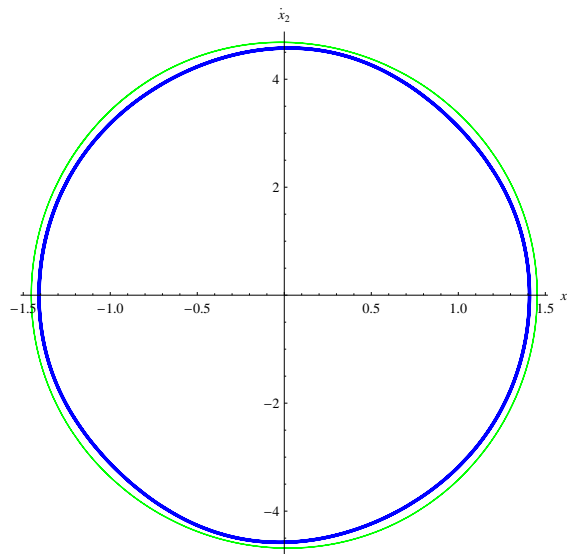
Table 5.1: NNM Results for SMD with Nonlinear Damping

Mode 1													Variation
k	g	c	μ	Exact Equations			NNM-A			Percent Error			
				x1 Amp.	x2 Amp.	Freq.	x1 Amp.	x2 Amp.	Freq.	x1 Amp.	x2 Amp.	Freq.	
1	0	-0.3	0.3	2.00	1.991	0.1579	1.844	1.937	0.1559	7.89	2.70	1.265	Linear Stiffness
5	0	-0.3	0.3	2.00	1.998	0.356	1.963	1.986	0.352	1.855	0.612	1.081	
10	0	-0.3	0.3	2.00	1.999	0.503	1.981	1.993	0.501	0.950	0.312	0.516	
10	0	-0.3	0.3	2.00	1.999	0.503	1.981	1.993	0.501	0.950	0.312	0.516	Nonlinear Stiffness
10	0.5	-0.3	0.3	1.987	2.12	0.521	1.869	1.988	0.518	5.91	6.25	0.680	
10	1	-0.3	0.3	1.975	2.25	0.536	1.762	1.953	0.528	10.78	13.09	1.405	
1	0	-0.3	0.3	2.00	1.991	0.1579	1.844	1.937	0.1559	7.89	2.70	1.265	Damping with Linear Stiffness
1	0	-0.6	0.3	2.84	2.78	0.1581	2.24	2.54	0.1505	21.1	8.65	4.83	
1	0	-0.3	0.6	1.42	1.408	0.1579	1.304	1.370	0.1558	7.89	2.70	1.328	
1	0	-0.6	0.6	2.01	1.967	0.1581	1.583	1.796	0.1510	21.1	8.65	4.46	Damping with Nonlinear Stiffness
10	0.5	-0.3	0.3	1.987	2.12	0.521	1.869	1.988	0.518	5.91	6.25	0.680	
10	0.5	-0.6	0.3	2.79	3.17	0.535	2.44	2.73	0.525	12.55	13.89	1.885	
10	0.5	-0.3	0.6	1.409	1.456	0.512	1.361	1.411	0.510	3.41	3.10	0.478	Damping with Nonlinear Stiffness
10	0.5	-0.6	0.6	1.987	2.12	0.520	1.827	1.965	0.512	8.09	7.19	1.413	

Mode 2													Variation
k	g	c	μ	Exact Equations			NNM-A			Percent Error			
				x1 Amp.	x2 Amp.	Freq.	x1 Amp.	x2 Amp.	Freq.	x1 Amp.	x2 Amp.	Freq.	
1	0	-0.3	0.3	2.00	2.01	0.276	1.999	2.20	0.280	0.065	9.18	1.211	Linear Stiffness
5	0	-0.3	0.3	2.00	2.00	0.616	2.000	2.04	0.618	0.023	1.84	0.316	
10	0	-0.3	0.3	2.00	2.00	0.872	2.000	2.02	0.873	0.012	0.922	0.172	
10	0	-0.3	0.3	2.00	2.00	0.872	2.000	2.02	0.873	0.012	0.922	0.172	Nonlinear Stiffness
10	0.5	-0.3	0.3	1.996	1.850	0.883	2.19	2.02	0.886	9.49	9.01	0.317	
10	1	-0.3	0.3	1.992	1.713	0.895	2.46	1.953	0.905	23.5	14.0	1.161	
1	0	-0.3	0.3	2.00	2.01	0.276	1.999	2.20	0.280	0.065	9.18	1.211	Damping with Linear Stiffness
1	0	-0.6	0.3	2.83	2.89	0.275	2.85	4.01	0.288	0.776	38.7	4.66	
1	0	-0.3	0.6	1.414	1.422	0.276	1.413	1.553	0.280	0.066	9.18	1.211	
1	0	-0.6	0.6	2.00	2.04	0.275	2.02	2.83	0.288	0.777	38.7	4.56	Damping with Nonlinear Stiffness
10	0.5	-0.3	0.3	1.996	1.850	0.883	2.19	2.02	0.886	9.49	9.01	0.317	
10	0.5	-0.6	0.3	2.82	2.43	0.894	3.50	3.04	0.910	24.2	25.3	1.765	
10	0.5	-0.3	0.6	1.413	1.360	0.877	1.474	1.430	0.879	4.37	5.13	0.245	Damping with Nonlinear Stiffness
10	0.5	-0.6	0.6	1.996	1.853	0.882	2.19	2.12	0.890	9.65	14.16	0.815	

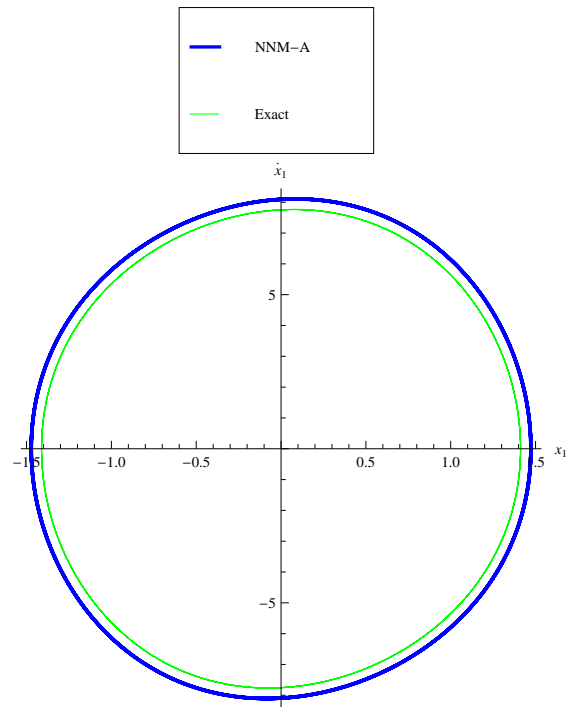


(a) x_1 Phase Space

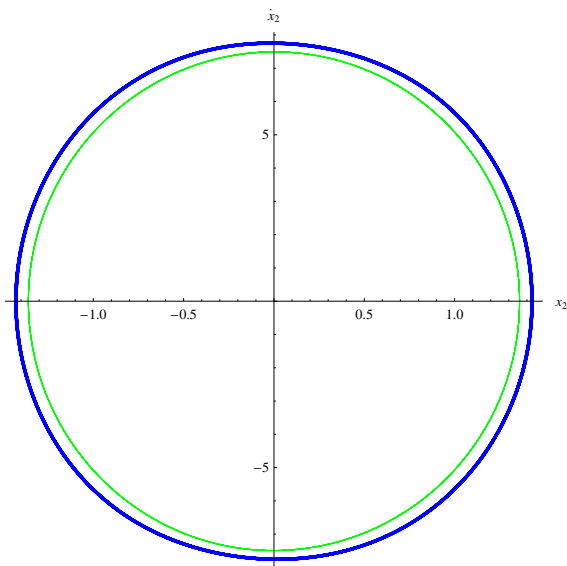


(b) x_2 Phase Space

Figure 5.1: Nonlinear SMD Phase Space Diagrams for First NNM, Case 1

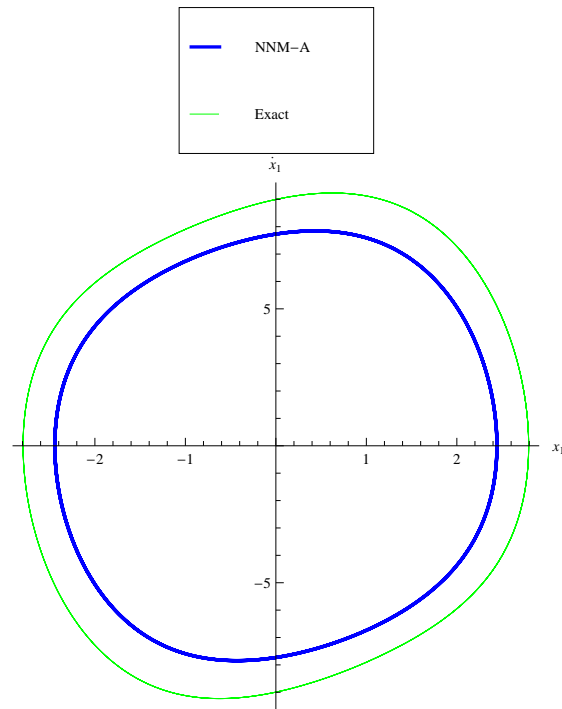


(a) x_1 Phase Space

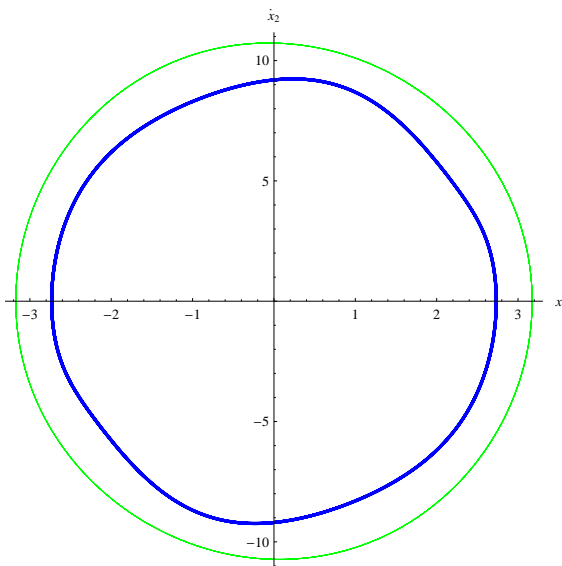


(b) x_2 Phase Space

Figure 5.2: Nonlinear SMD Phase Space Diagrams for Second NNM, Case 1

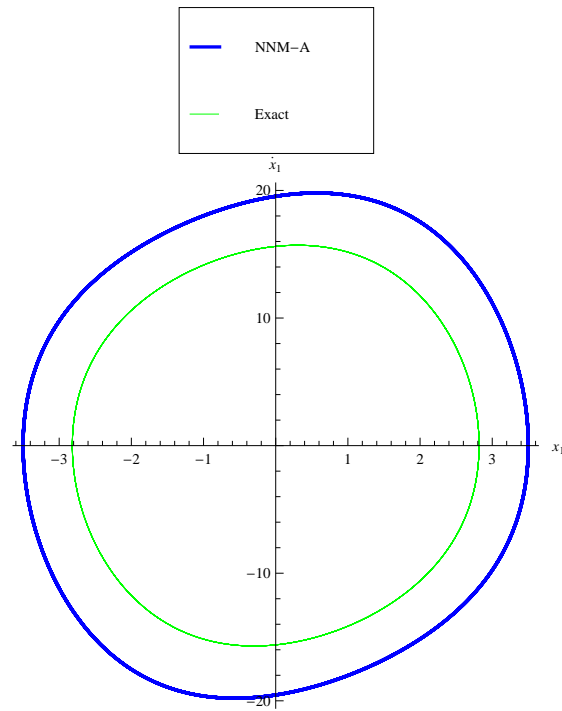


(a) x_1 Phase Space

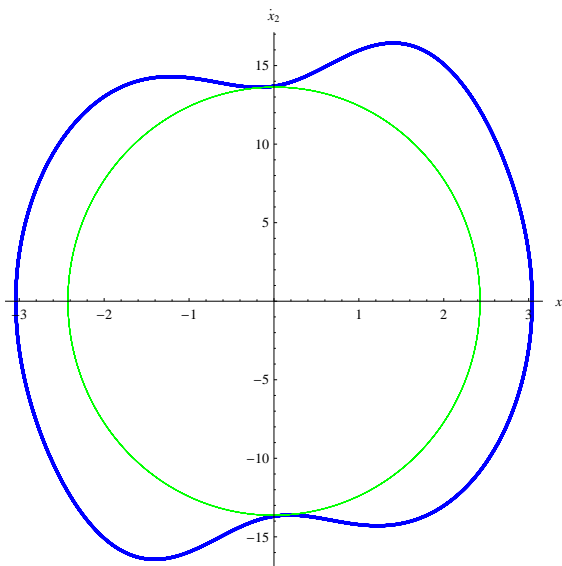


(b) x_2 Phase Space

Figure 5.3: Nonlinear SMD Phase Space Diagrams for First NNM, Case 2



(a) x_1 Phase Space



(b) x_2 Phase Space

Figure 5.4: Nonlinear SMD Phase Space Diagrams for Second NNM, Case 2

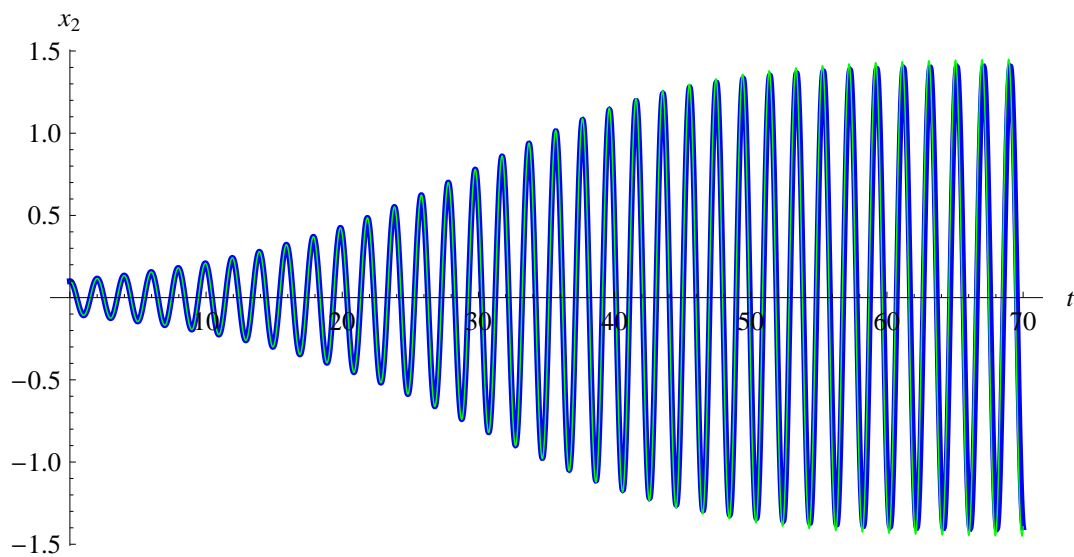
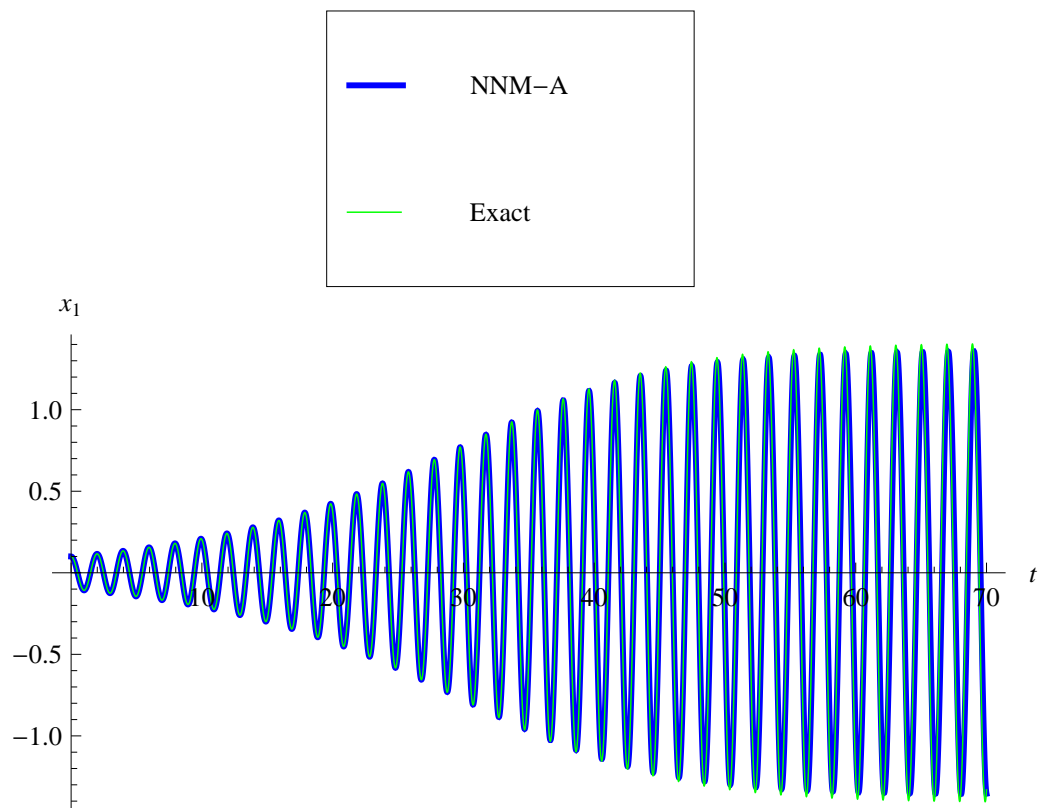
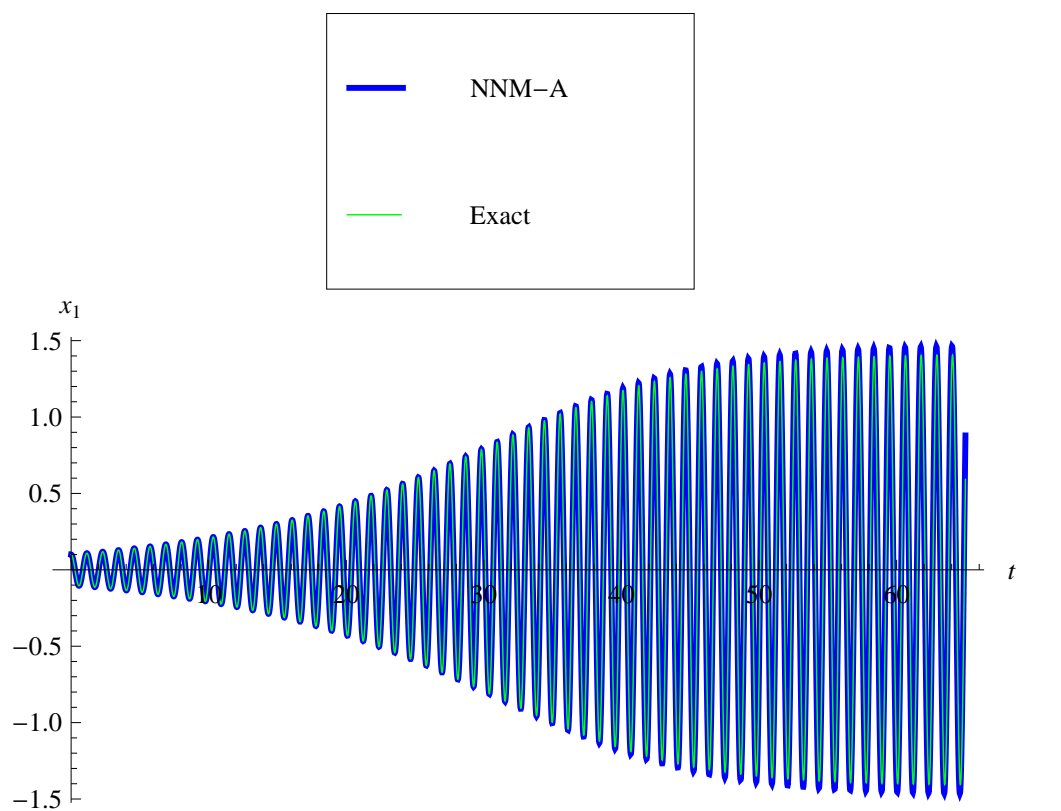
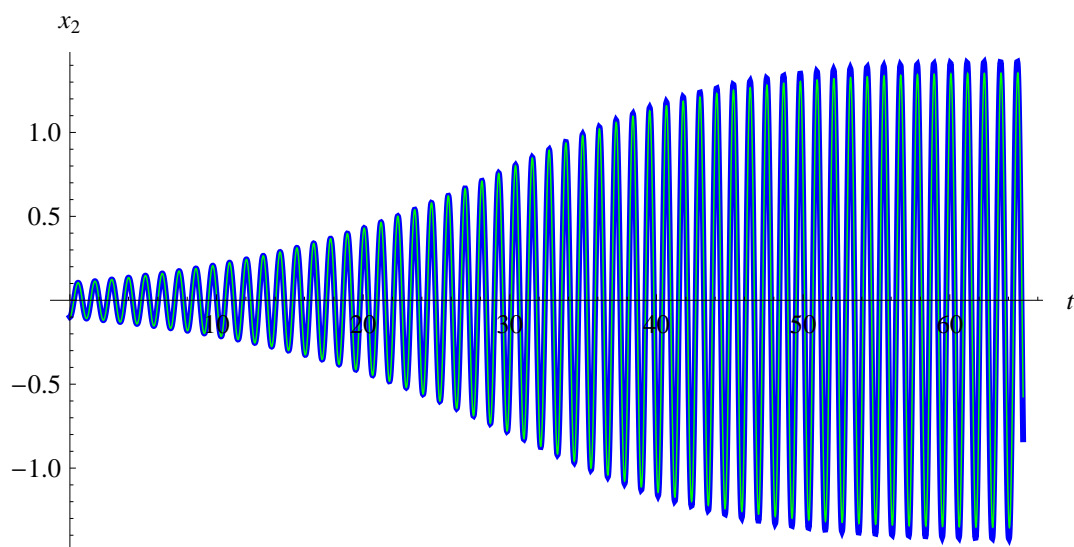


Figure 5.5: Nonlinear SMD Time History for First NNM, Case 1



(a) x_1 Time History



(b) x_2 Time History

Figure 5.6: Nonlinear SMD Time History for Second NNM, Case 1

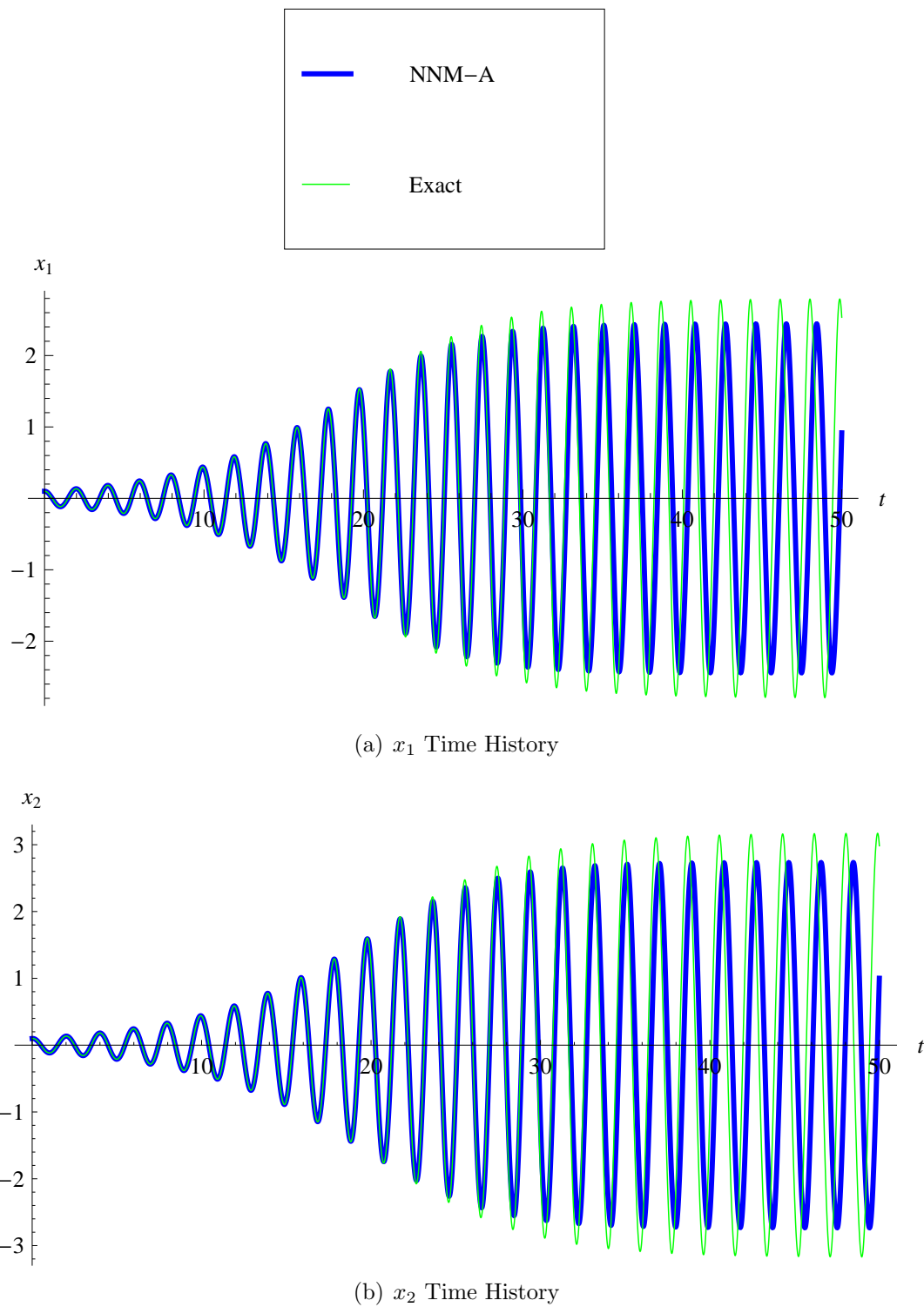


Figure 5.7: Nonlinear SMD Time History for First NNM, Case 2

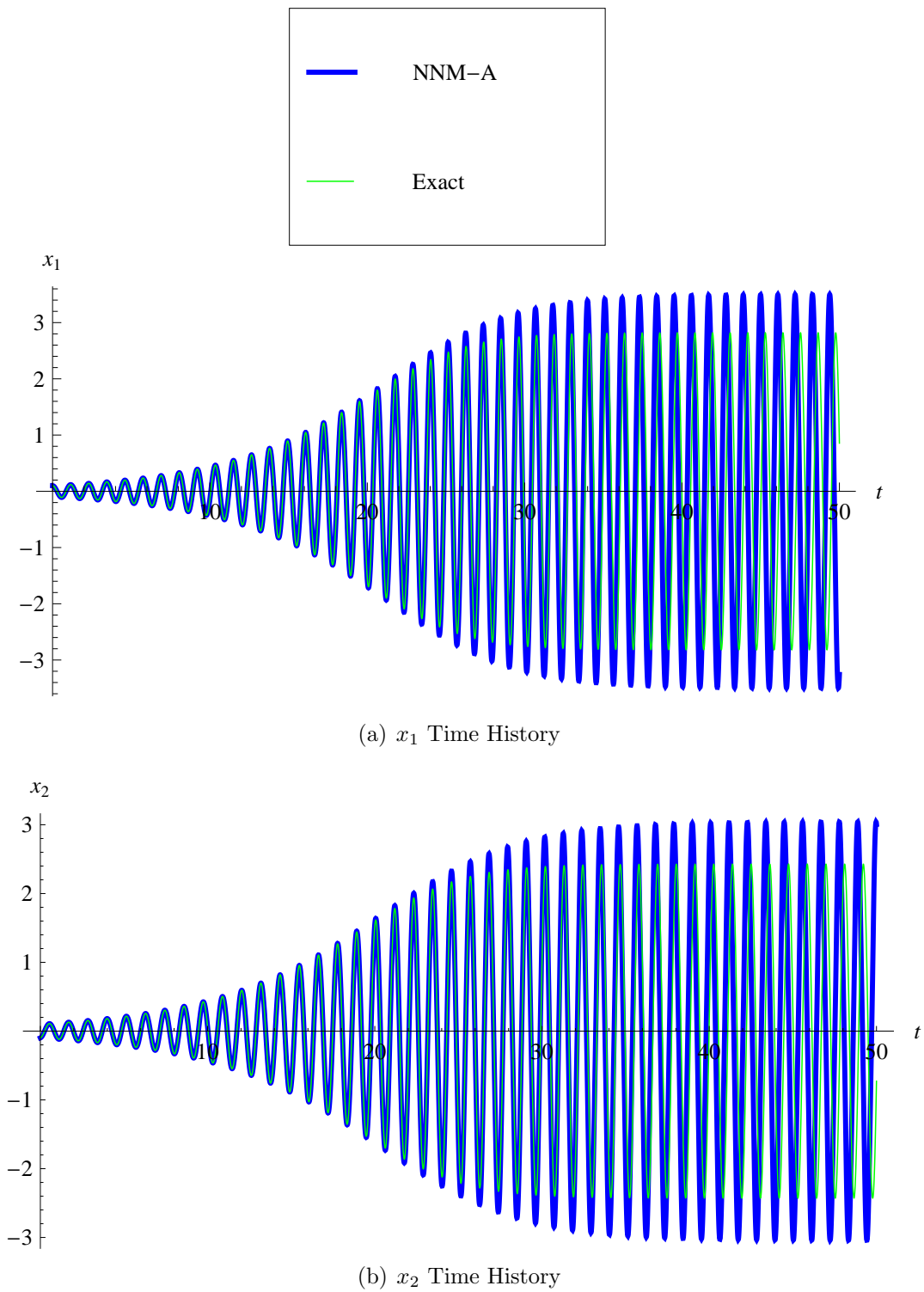


Figure 5.8: Nonlinear SMD Time History for Second NNM, Case 2

5.2 Pitch-Plunge Airfoil with Quasi-steady Aerodynamics

The pitch-plunge airfoil with quasi-steady aerodynamics and a nonlinear pitch stiffness was the first aeroelastic system on which the NNM method was attempted. Since it was the simplest aeroelastic system, it was also used for studies on master coordinate selection and improved coefficient solution methods.

For the test cases presented, the following constants were used in Eq. (4.2).

$$\begin{aligned}\mu &= 11 \\ a &= -0.35 \\ x_\alpha &= .2 \\ r_\alpha &= .5 \\ \bar{\omega} &= 0.5 \\ G_\alpha &= 0.5\end{aligned}\tag{5.1}$$

Additionally $C[k]$ was set to unity making the aerodynamics quasi-steady. This model has a dimensionless linear flutter speed of 0.807 and linear flutter frequency of 0.1598 Hz. Other cases were tested, but the results were very nearly the same and only confirmed the conclusions reached with the model above.

5.2.1 Sample Results

Since the system in Eq. (4.2) is not in the form needed for the NNM method, it must first be transformed. The simplest route is to multiply by the inverse of the mass matrix so the plunge degree of freedom can be used as the master coordinate. At each freestream velocity of interest, the standard derivation of the asymptotic NNMs was followed. The final result is two uncoupled modal equations. Below is an example of this result for a nondimensional

velocity of 1.05 times the linear flutter velocity. The LCO NNM modal equation is

$$\begin{aligned}
 \ddot{u} = & u(-1.000 - 4.37u^2 - 9.44\dot{u}^2 - 26.5u^4 - 62.7u^2\dot{u}^2 - 7.45\dot{u}^4 \\
 & - 192.1u^6 - 272u^4\dot{u}^2 + 155.2u^2\dot{u}^4 + 192.8\dot{u}^6 \\
 & - 465u^8 - 1288u^6\dot{u}^2 - 1373u^4\dot{u}^4 - 900u^2\dot{u}^6 - 331\dot{u}^8) \\
 & + \dot{u}(0.00462 - 2.86u^2 + 0.312\dot{u}^2 - 68.5u^4 - 44.3u^2\dot{u}^2 + 25.5\dot{u}^4 \\
 & - 206u^6 - 231u^4\dot{u}^2 - 76.0u^2\dot{u}^4 - 69.3\dot{u}^6 \\
 & + 207u^8 + 1091u^6\dot{u}^2 + 1475u^4\dot{u}^4 + 636u^2\dot{u}^6 + 62.9\dot{u}^8).
 \end{aligned} \tag{5.2}$$

The destabilizing linear damping term is apparent in this LCO modal equation. The second NNM modal equation is a damped oscillator as would be expected.

$$\begin{aligned}
 \ddot{u} = & u(-0.236 - 0.01472\dot{u}^2 - 0.0316\dot{u}^4 + 0.01460\dot{u}^6 - 0.00224\dot{u}^8) \\
 & + \dot{u}(-0.207 + 0.00738u^2 - 0.00224u^4 + 0.0000965u^6 - 1.347 \times 10^{-6}u^8) \\
 & + (0.00179u^3 - 0.000434u^5 + 0.00001555u^7 - 1.855 \times 10^{-7}u^9 - 0.00874u^3\dot{u}^2 \\
 & + 0.000555u^5\dot{u}^2 - 9.72 \times 10^{-6}u^7\dot{u}^2 - 0.00469\dot{u}^3 - 0.0239u^2\dot{u}^3 + 0.00207u^4\dot{u}^3 \\
 & - 0.0000443u^6\dot{u}^3 + 0.00549u^3\dot{u}^4 - 0.0001631u^5\dot{u}^4 - 0.01516\dot{u}^5 + 0.01151u^2\dot{u}^5 \\
 & - 0.000483u^4\dot{u}^5 - 0.001066u^3\dot{u}^6 + 0.00738\dot{u}^7 - 0.001865u^2\dot{u}^7 - 0.001197\dot{u}^9)
 \end{aligned} \tag{5.3}$$

The stabilizing linear damping is easily visible in this damped modal equation. For comparison, the modal equations of motion for the LNM are also presented. First, the LCO mode is

$$\ddot{u} = u(-1.000 - 1.215u^2 - 6.83\dot{u}^2) + \dot{u}(0.00462 - 4.99u^2 - 3.12\dot{u}^2). \tag{5.4}$$

The damped modal equation for LNM is

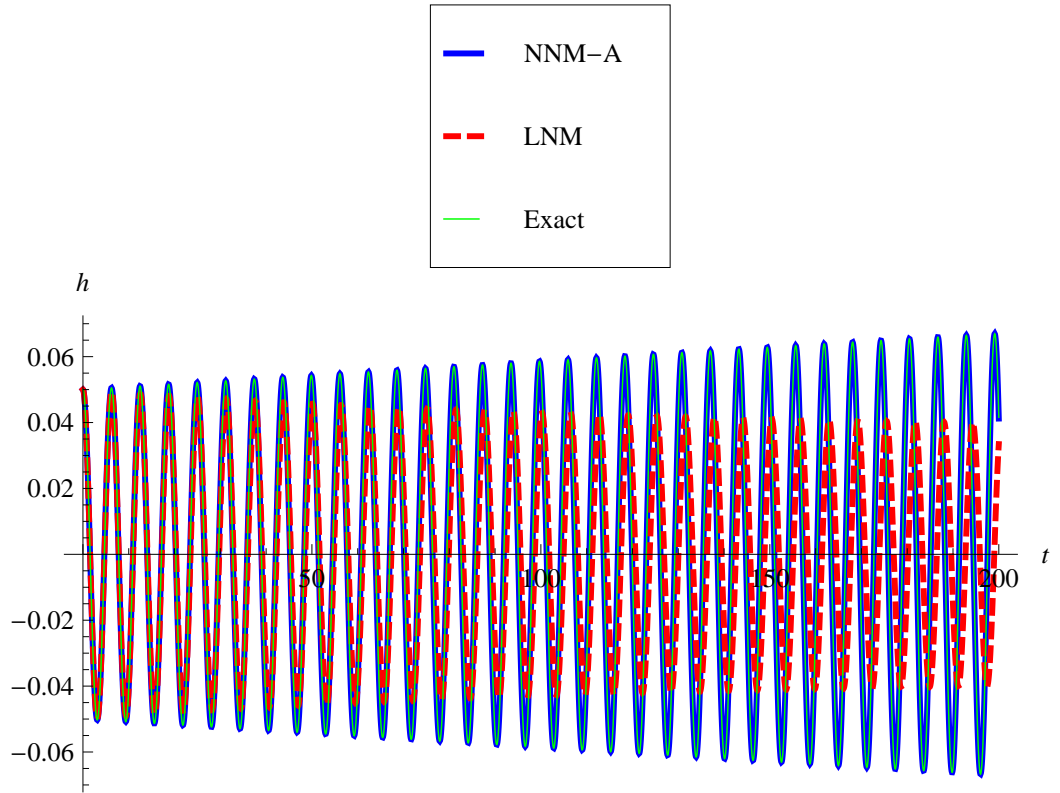
$$\ddot{u} = u(-0.236 + 0.0228\dot{u}^2) + \dot{u}(-0.207 + 0.01661u^2) + (0.00404u^3 + 0.01039\dot{u}^3) \tag{5.5}$$

The stabilizing and destabilizing linear damping terms can also be seen in these LNM equations. Comparing these two sets of equations, it is obvious that the NNM equations capture significantly more nonlinear coupling terms than the LNM equations.

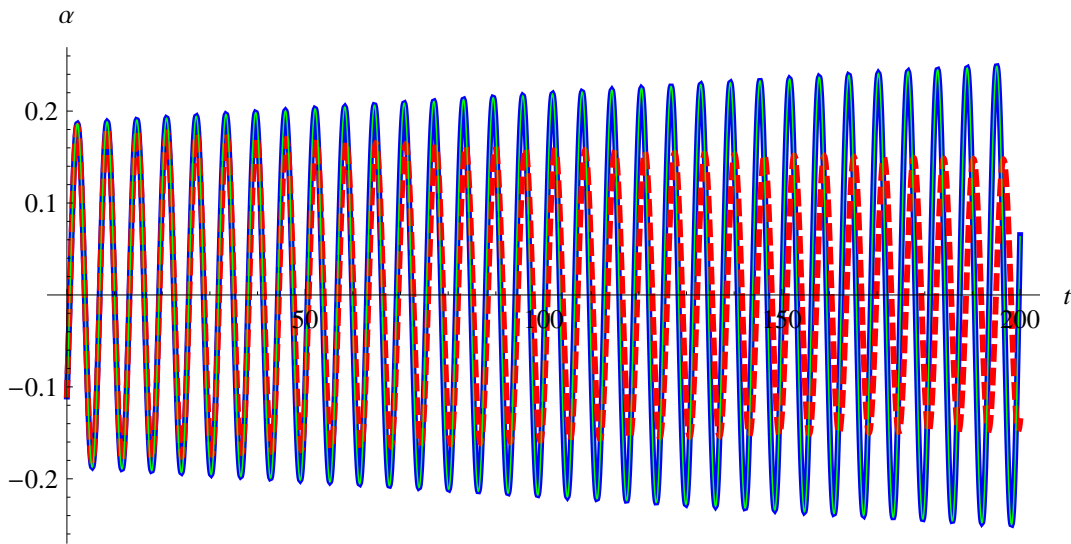
The Runge-Kutta simulation of the NNM modal equation for LCO is compared to a simulation of the original equation of motion and the LNM equation of motion for LCO. The exact solution is given a modal initial condition for the LCO NNM. Figure 5.9 shows the growth of LCO motion and 5.10 shows in phase space the motion after settling into LCO. As can be seen in the time history and phase space plots, the NNM does a very good job of modeling LCO motion and growth. The NNM is obviously much better than the LNM. The reason the LNM equation does not do well is obvious when Eqs. (5.2) and (5.4) are compared since the LNM equation is missing a vast majority of the nonlinear terms.

Figure 5.11 shows a comparison of the time history for the damped modes. Both the NNM and the LNM give a nearly exact solution for the damped mode's decay. All of this motion occurs in the linear amplitude range and since the linear parts of both solutions are exact, a nearly exact solution is produced. These are not exact solutions since the nonlinear terms still exist and are inexact even though they are very, very small. Due to the inexactness of the NNM, which is used to generate the modal initial condition for the simulation of the original equations of motion, an extremely small part of the LCO mode is excited by the initial condition. If the simulation of the exact equations of motion is allowed to run for long enough, the LCO motion will begin to appear. This is shown in Fig. 5.12. Since this growth is due to inaccuracies in the initial condition, the modal solutions do not show this motion growth.

The results for the NNM are not always as good as in the above example. If the nonlinearities in the system are too strong, the asymptotic NNM will not perform as well. Figure 5.13 is the same system as above except the nondimensional freestream velocity has been increased to 1.17 times the linear flutter velocity. The higher velocity causes a higher amplitude. This makes the system nonlinearities stronger since the nonlinearity is dependent on the amplitude. In the figure, it is obvious that neither the NNM or LNM are doing a

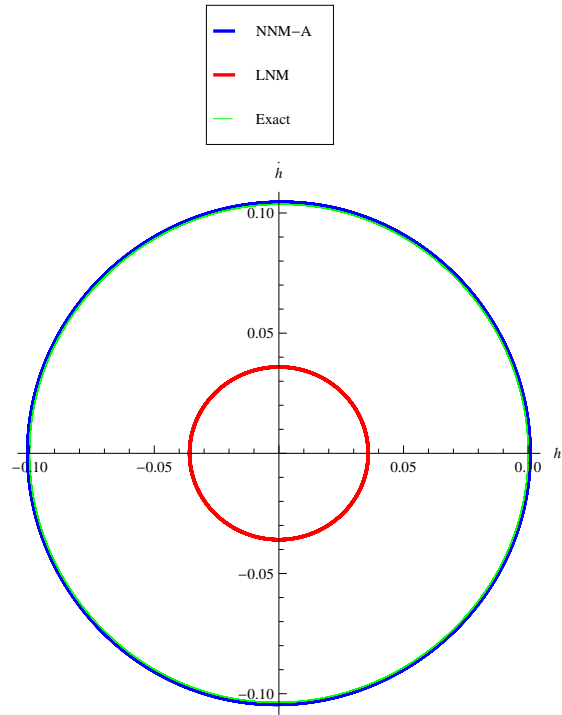


(a) Plunge

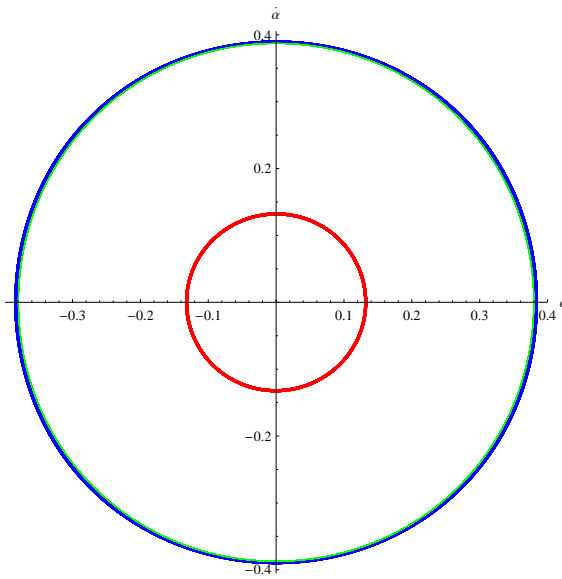


(b) Pitch

Figure 5.9: LCO Time History Plots of Quasi-steady Airfoil at $1.05 V_f$

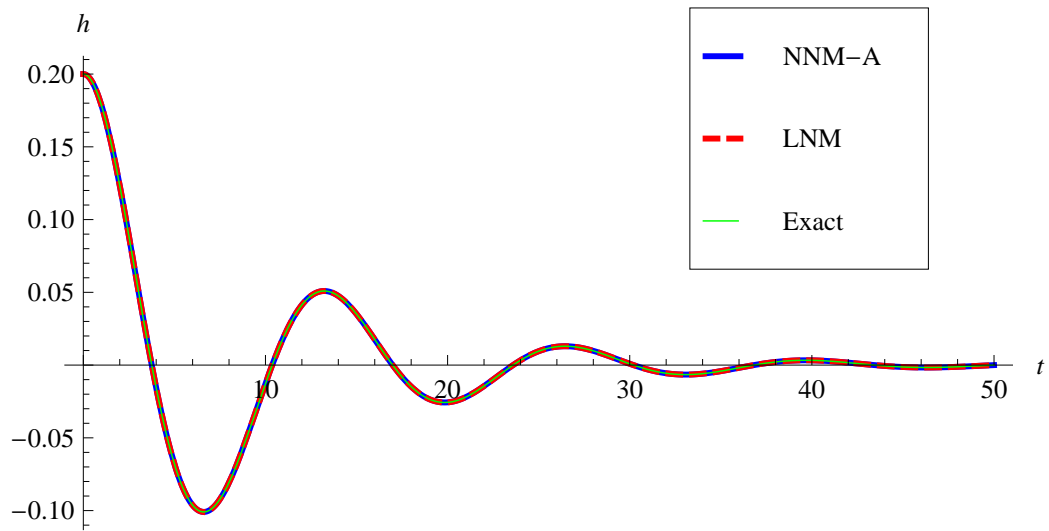


(a) Plunge

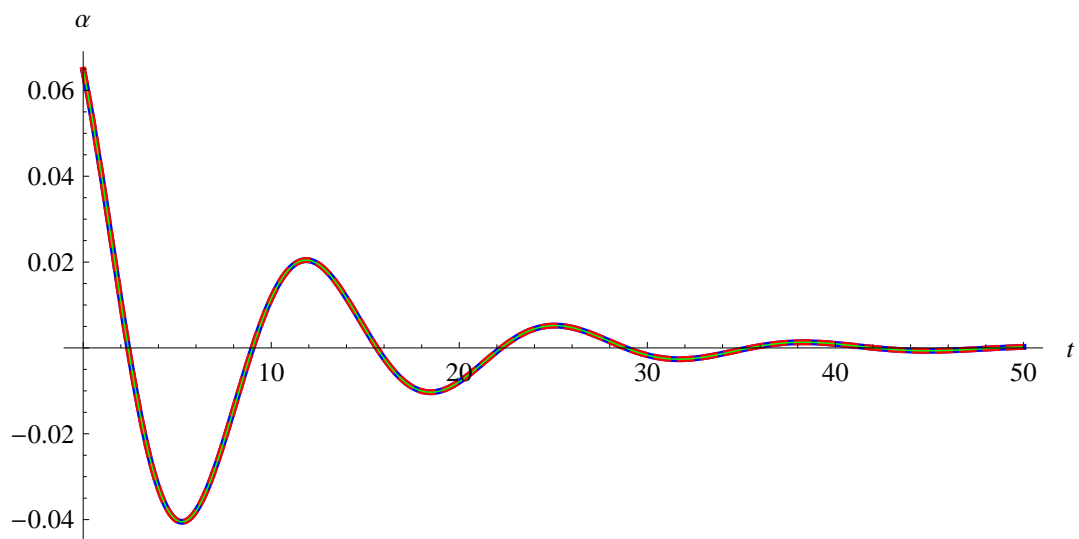


(b) Pitch

Figure 5.10: LCO Phase Space Plots of Quasi-steady Airfoil at $1.05 V_f$



(a) Plunge



(b) Pitch

Figure 5.11: Damped Mode Time History Plots of Quasi-steady Airfoil at $1.05 V_f$

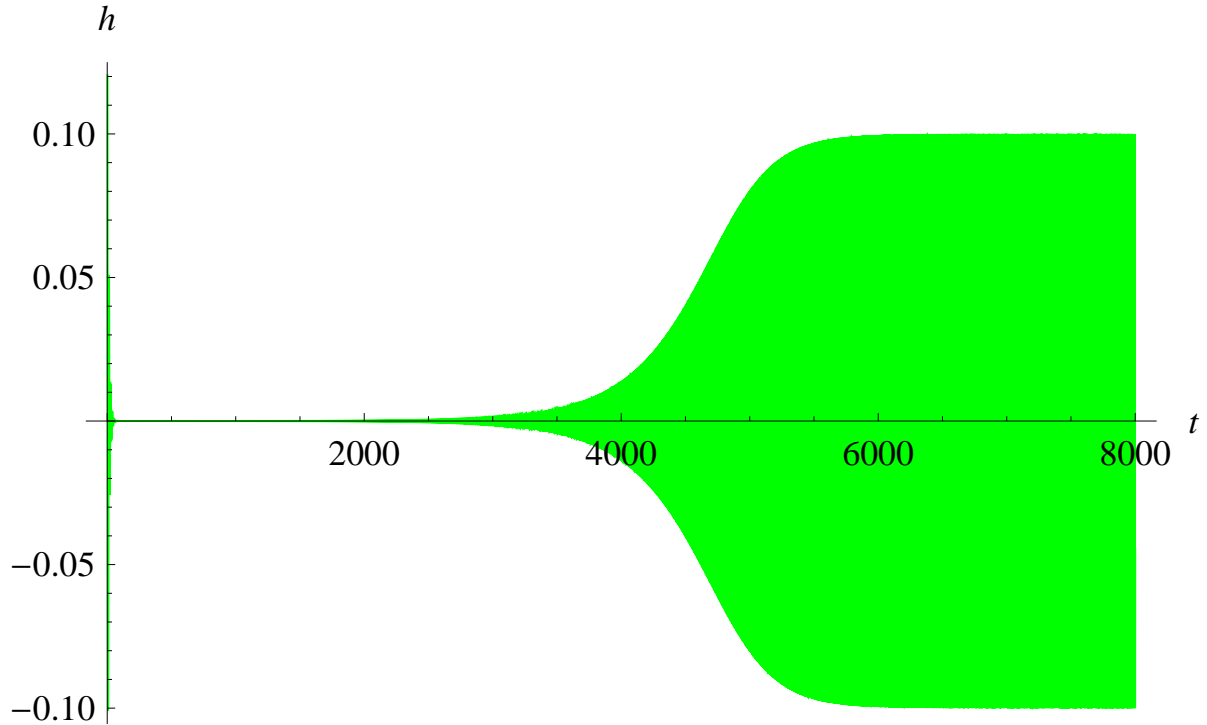
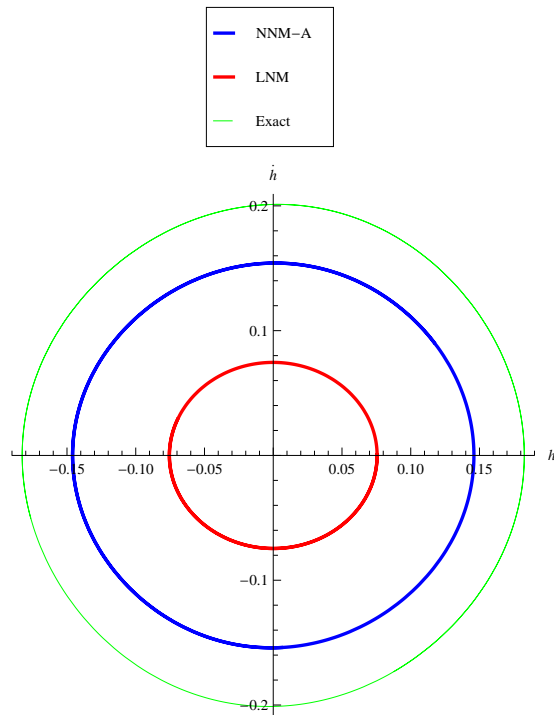


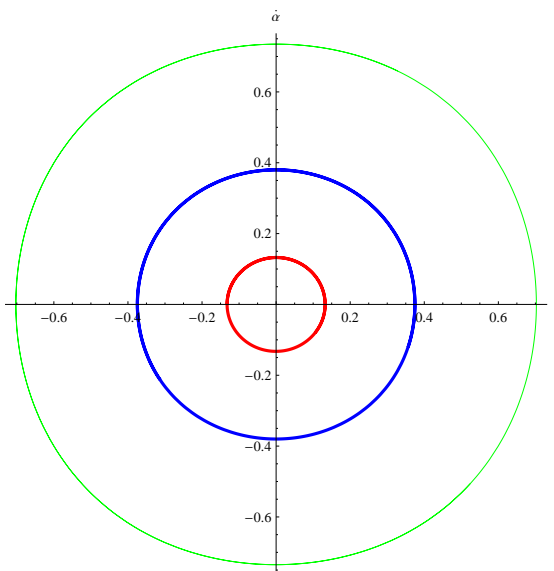
Figure 5.12: Growth of LCO Motion in Exact System due to Approximate Initial Condition

good job of modeling the exact solution, but the NNM is doing much better than the LNM. Figures 5.14 and 5.15 show the exact and asymptotic NNM frequencies and amplitudes as the freestream velocity is increased. These figures also display the degradation of the NNM solution when the velocity is increased. If the velocity is increased further, the asymptotic solution will slowly lose its stability and produce a divergent solution even though a LCO still exists for the exact solution.

Figures 5.16 and 5.17 show the convergence of the solution as the order of the approximation is increased. At $1.01V_f$, the solution quickly converges toward zero as the order is increased. However, the solution does not immediately converge at $1.05V_f$. The error first increases and then converges toward zero.



(a) Plunge



(b) Pitch

Figure 5.13: LCO Phase Space Plots of Quasi-steady Airfoil at $1.17 V_f$

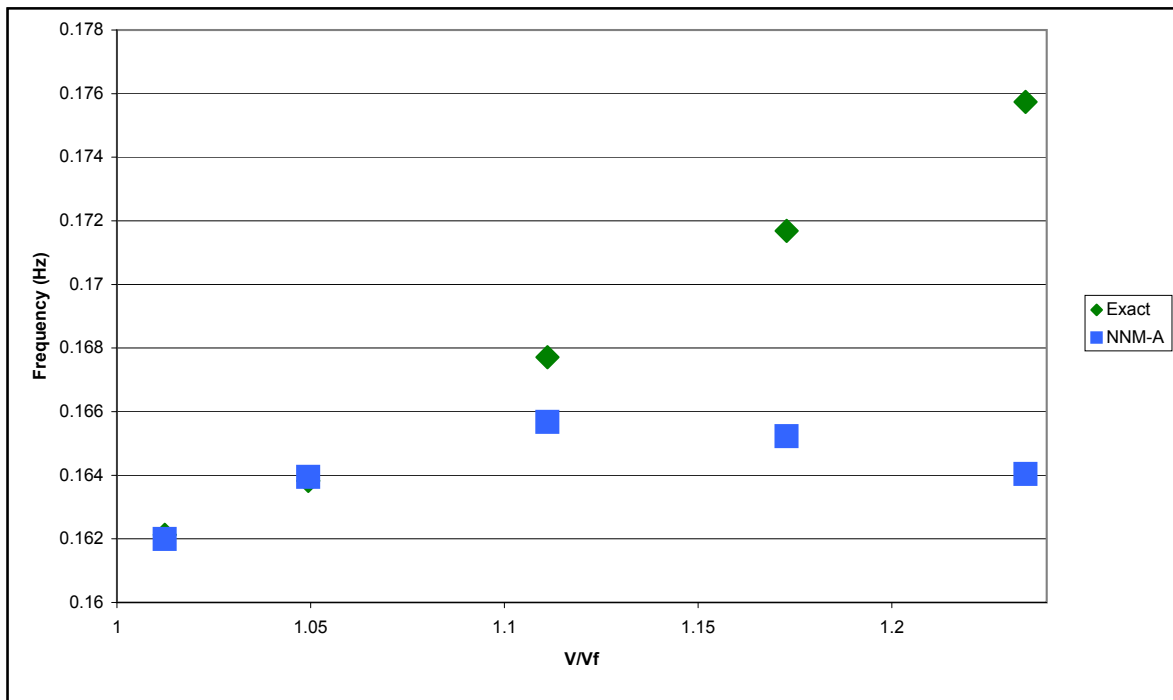


Figure 5.14: Frequency vs. Velocity

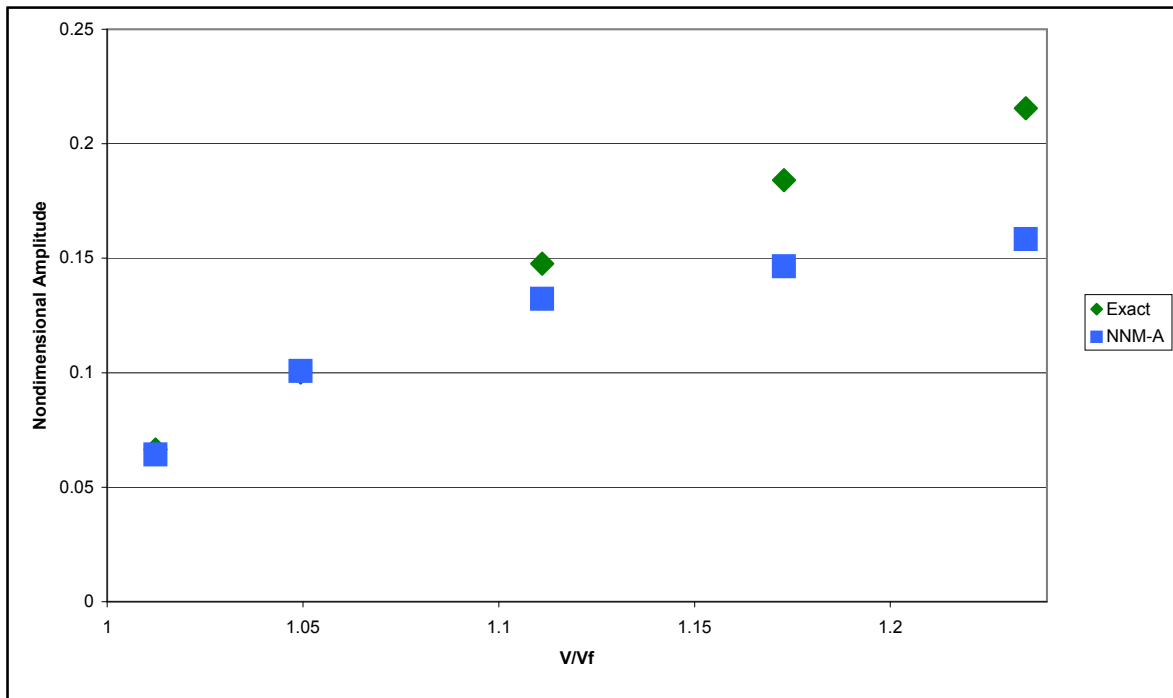


Figure 5.15: Amplitude vs. Velocity

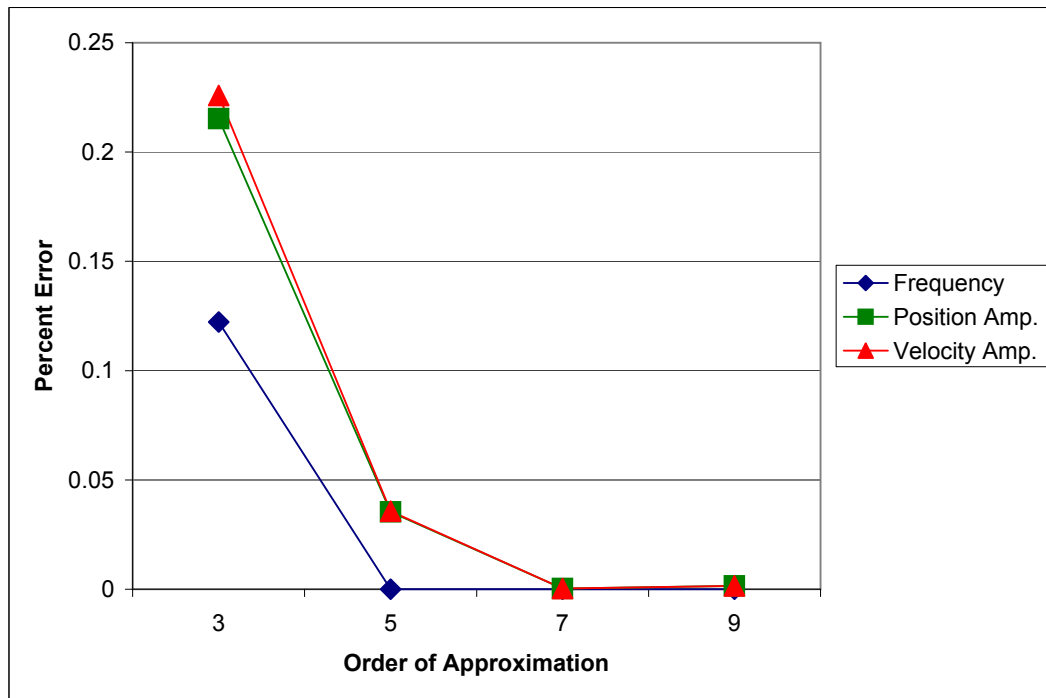


Figure 5.16: Asymptotic Convergece at $1.01V_f$

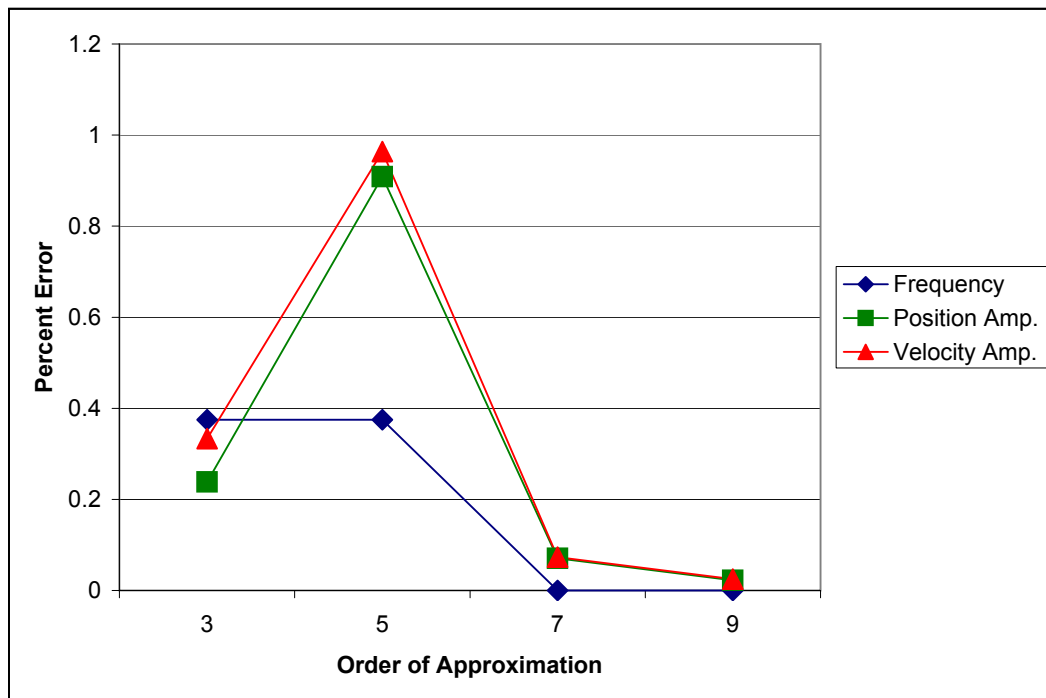


Figure 5.17: Asymptotic Convergece at $1.05V_f$

5.2.2 Master Coordinate Study

Each nonlinear normal mode is built off a specific master coordinate. Since the resulting mode is an approximation, the selection of the master coordinate affects the accuracy of the results. The master coordinate can be directly a degree of freedom or it can be a modal coordinate. Throughout this work three different modal coordinates were used for the pitch-plunge airfoil model. They are referred to as M^{-1} , linear structural mode shapes with apparent mass, and linear flutter mode. Each is discussed in detail below.

Direct Degree-of-Freedom (M^{-1})

The easiest master coordinate to use is one of the degrees of freedom of the system. However, unlike in the spring-mass-damper example, the mass matrix for an aeroelastic system is usually not an identity matrix. The aeroelastic system from Eq. (4.2) was rewritten as

$$[M] \{\ddot{q}_i\} = f_i [\{q_i\}, \{\dot{q}_i\}]. \quad (5.6)$$

Note that the mass matrix $[M]$ above is the aeroelastic mass matrix and thus includes the apparent mass effects from the aerodynamic model. Both sides of the rewritten equation are then multiplied by the inverse of the mass matrix to get

$$\{\ddot{q}_i\} = [M]^{-1} f_i [\{q_i\}, \{\dot{q}_i\}]. \quad (5.7)$$

Now one of the degrees of freedom may be used as the master coordinate. This master coordinate may be referred to as the M^{-1} , plunge, or pitch master coordinate.

Linear Structural Mode Shapes with Apparent Mass

The second master coordinate used was referred to as the linear structural mode shapes with apparent mass effects. This is a modal degree of freedom used as the master coordinate. To find this modal coordinate, the aeroelastic system in Eq. (4.2) was linearized and the

freestream velocity was set to zero.

$$\begin{pmatrix} 1 + \frac{1}{\mu} & x_\alpha - \frac{a}{\mu} \\ x_\alpha - \frac{a}{\mu} & r_\alpha^2 + \frac{1}{8\mu} + \frac{a^2}{\mu} \end{pmatrix} \begin{pmatrix} \ddot{h} \\ \ddot{\alpha} \end{pmatrix} = \begin{pmatrix} 0 & 0 \\ 0 & 0 \end{pmatrix} \begin{pmatrix} \dot{h} \\ \dot{\alpha} \end{pmatrix} - \begin{pmatrix} \bar{\omega}^2 & 0 \\ 0 & r_\alpha^2 \end{pmatrix} \begin{pmatrix} h \\ \alpha \end{pmatrix} \quad (5.8)$$

A standard linear modal analysis was performed and the modal transformation matrix was found. The linear modal transformation matrix was used to transform the nonlinear system which is in the form of Eq. (5.6). Since the aeroelastic mass matrix is linear and does not depend on the velocity, the transformation converts it to an identity matrix and system will be of the nice form below.

$$\{\ddot{\eta}_i\} = f_i [\{\eta_i\}, \{\dot{\eta}_i\}] \quad (5.9)$$

With the nonlinear system written in terms of the linear structural modes with apparent mass, η_i , each of the modal coordinates could be used as the master coordinate.

Linear Flutter Mode

The linear flutter mode was also used as a modal master coordinate. Starting with the aeroelastic equations of motion in Eq. (4.2), the system was linearized. The velocity of interest (above the linear flutter velocity) was chosen and the eigenvalue procedure detailed in Patil[46] was used to find the left and right modal transformation matrices required to put the linear system in decoupled, second-order form. When these transformation matrices are applied to a linearized system in first-order form, it results in a block diagonal matrix with sub-matrices of the form:

$$\begin{bmatrix} 0 & 1 \\ C_1 & C_2 \end{bmatrix}. \quad (5.10)$$

When these same transformation matrices are applied to the nonlinear first-order system matrix, the resulting matrix is fully populated. Assuming a cubic pitch stiffness nonlinearity,

the block diagonal parts take the form seen below and the off block diagonal zeros are constants times α^2 .

$$\begin{bmatrix} C_3\alpha^2 & 1 + C_4\alpha^2 \\ C_1 + C_5\alpha^2 & C_2 + C_6\alpha^2 \end{bmatrix} \quad (5.11)$$

This first-order system of equations obviously cannot be converted back to second-order form and is consequently not in the form needed for the standard derivation of NNM. Thus, the first-order formulation had to be utilized anytime the linear flutter mode was used as the master coordinate. When choosing the two master coordinates from the first-order system, the two equations that would create the flutter mode from the linear matrix must be selected. If the other pair that creates the damped mode is selected, the LCO will not be found. Additionally, the linear unknown modal coefficients will be exactly zero since there is no linear coupling between the modes.

Master Coordinate Results

Figures 5.18 and 5.19 show the results from the master coordinate study. Note that the vertical axis is logarithmic. The percent error of the NNM solution is plotted against increasing velocity. The errors are found by comparing the NNM solution to the simulation of the original equations of motion. The percent error was calculated for the frequency, the displacement amplitude of the master and slave coordinates, and the velocity amplitude of the master and slave coordinates. The average of all four amplitude errors gave an accurate picture of how the NNM was performing with out have to look at a whole handful of plots; therefore, the average amplitude error is presented in the plot. The master coordinates are as follows, Minv is the plunge, Minv 2 is the pitch, ZV and ZV 2 are the first and second linear structural modes with apparent mass, and flutter is the linear flutter mode.

It is obvious from the figures that the accuracy of the results is dependent on the selection of the modal coordinate. It is not immediately apparent what the best coordinate would be. Selection would appear to depend on what velocity was of interest. The results

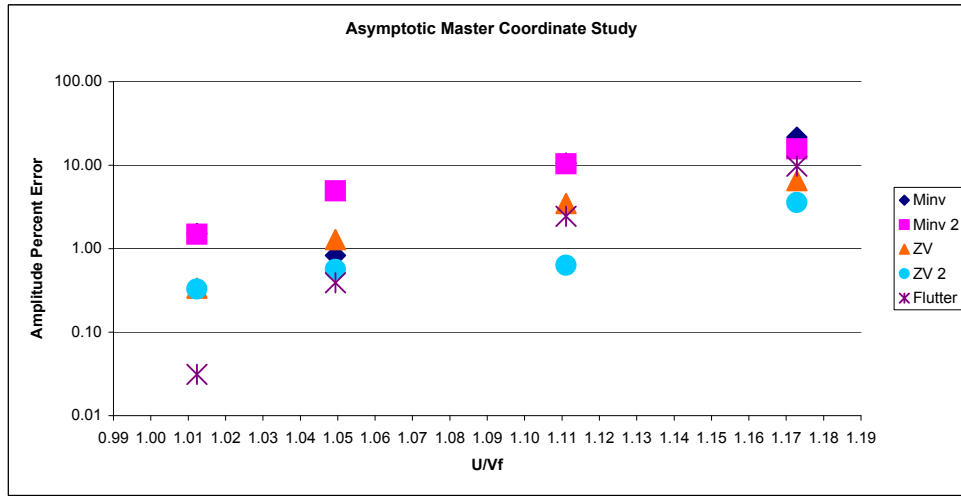


Figure 5.18: Master Coordinate Amplitude Error Results

for all of the master coordinates degrade as the velocity increases. This is caused by the larger amplitude at the higher velocities creating a system that effectively has a stronger nonlinearity. Within about 10% of the flutter velocity, the linear flutter mode gives the best results for both amplitude and frequency. After this point the, linear flutter master coordinate starts becoming unstable and produces a divergent solution at $1.19V_f$ (just beyond the range of the plot). At a certain velocity (or amplitude), all of the NNMs based on an asymptotic formulation will begin to diverge. In this case, the linear flutter master coordinate is the first to lose it's stability. The structural mode shapes are not far behind and produce a divergent solution at $1.29V_f$. The pitch and plunge master coordinates remain stable much longer ($> 2V_f$), but as can be seen in the error plots they have a large error even at $1.17V_f$. Since the flutter mode is the most accurate in the low velocity range where the asymptotic method can be trusted, it is the best master coordinate for the low speed regime. Additionally, as will be shown in the section on the collocation solution, the linear flutter mode exhibits an apparent convergence and very low error when used with the collocation method while the other mode shapes do not. With this information, the linear flutter mode can be considered the best choice of master coordinate.

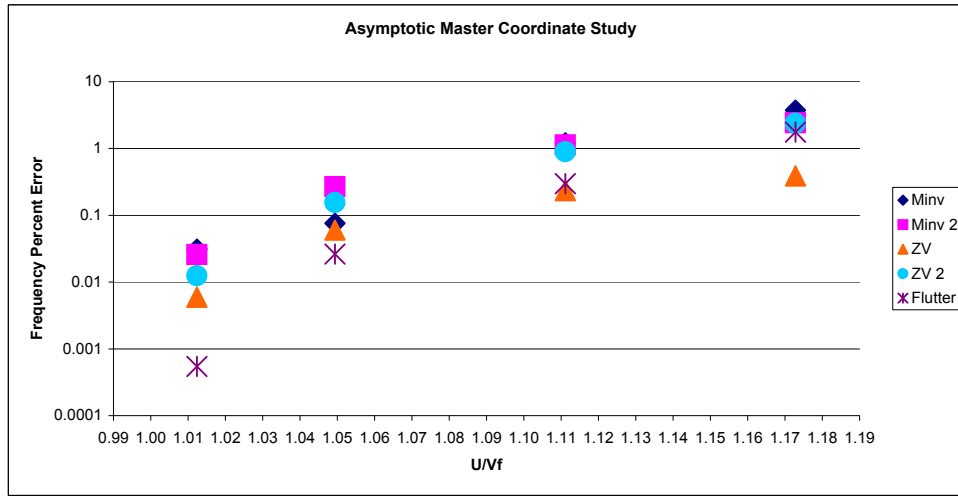


Figure 5.19: Master Coordinate Frequency Error Results

5.2.3 Galerkin Modal Coefficient Solution

The Galerkin solution method was used in an attempt to improve on the results of the asymptotic method. Use of the Galerkin method should allow stronger nonlinearities in the system without a large loss in accuracy. The Galerkin solution also remains stable at high velocities. The Galerkin method can offer very good results, but has two main drawbacks. The computational cost for the Galerkin method is quite high with the Galerkin solution taking near ten minutes while the asymptotic solution can be found in about 0.1 seconds. The Galerkin solution was also sensitive to the region used for integration and there is no immediately apparent method to iterate the integration region and establish a convergence criterion.

Galerkin Solution at Moderate Velocity

Table 5.2 contains the results from the Galerkin method used for the same airfoil system used in the sample results section above. The moderate velocity, $1.17V_f$, was used. The “Region - Exact Ratio” column is the integration limits divided by the amplitude of the exact solution. This gives the size of the integration region relative to the size of the exact LCO motion. The

Table 5.2: Galerkin Integration Region Data

Region - Exact Ratio	Integration Limits		NNM-G Solution Amplitude		Exact Solution Amplitude		Percent Error		Solution-Region Fraction	
	U	V	u	v	u	v	u	v	u	v
0.5	0.0913	0.1006	0.1579	0.1694	0.1826	0.201	-13.53	-15.80	1.729	1.684
0.75	0.1369	0.1509	0.1361	0.1475			-25.45	-26.66	0.994	0.978
0.9	0.1643	0.1811	0.1454	0.1409			-20.36	-29.95	0.885	0.778
1	0.1826	0.201	0.1440	0.1522			-21.12	-24.36	0.789	0.756
1.1	0.201	0.221	0.1707	0.1886			-6.51	-6.27	0.850	0.852
1.2	0.219	0.241	0.1733	0.1811			-5.07	-9.99	0.791	0.750
1.3	0.237	0.262	0.1833	0.204			0.38	1.57	0.772	0.781
1.4	0.256	0.282	0.1832	0.203			0.36	1.03	0.717	0.722
1.5	0.274	0.302	0.1858	0.202			1.74	0.54	0.678	0.670
1.6	0.292	0.322	0.157695	0.1654			-13.63	-17.76	0.540	0.514

actual limits used for the Galerkin integrals are given in the next two columns. The percent error for u and v is presented. Since the M^{-1} plunge master coordinate is being used, u and v correspond directly to h and \dot{h} . The last two columns in the table, “Solution - Region Fraction,” is the Galerkin solution amplitudes divided by the integration limits. This number shows how large the approximate LCO solution is compared to the integration region. As can be seen by looking at these results, the error fluctuates as the size of the integration region is increased. The solution-region fraction does not have any special relationship to the error. The best results are found when the fraction is around 0.72, but a few rows up a fraction of about 0.76 generates some of the worst results. Without a special relation between what would be the only two known quantities in a problem where the exact solution is not known, an iteration scheme and convergence criteria are difficult to create. Five of the solutions from the table are plotted in Figs. 5.20 through 5.24. The rows corresponding to the plotted solutions are in bold. The figures show that that the Galerkin solution can give very good results, but if the integration region is not the correct size the Galerkin solution offers poor results that no better than the asymptotic solution.

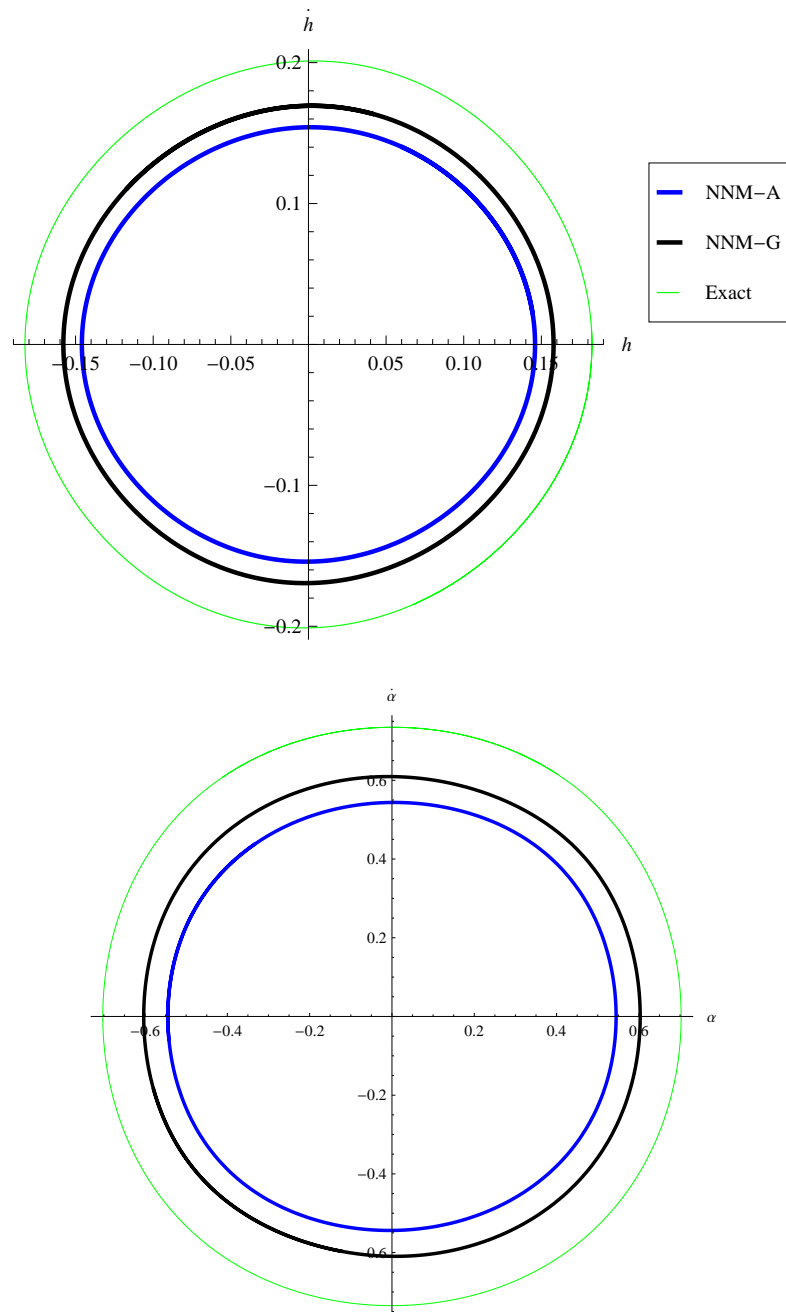


Figure 5.20: Galerkin with Integration Region $0.5 \times \text{Exact}$ Amplitudes, $1.17V_f$

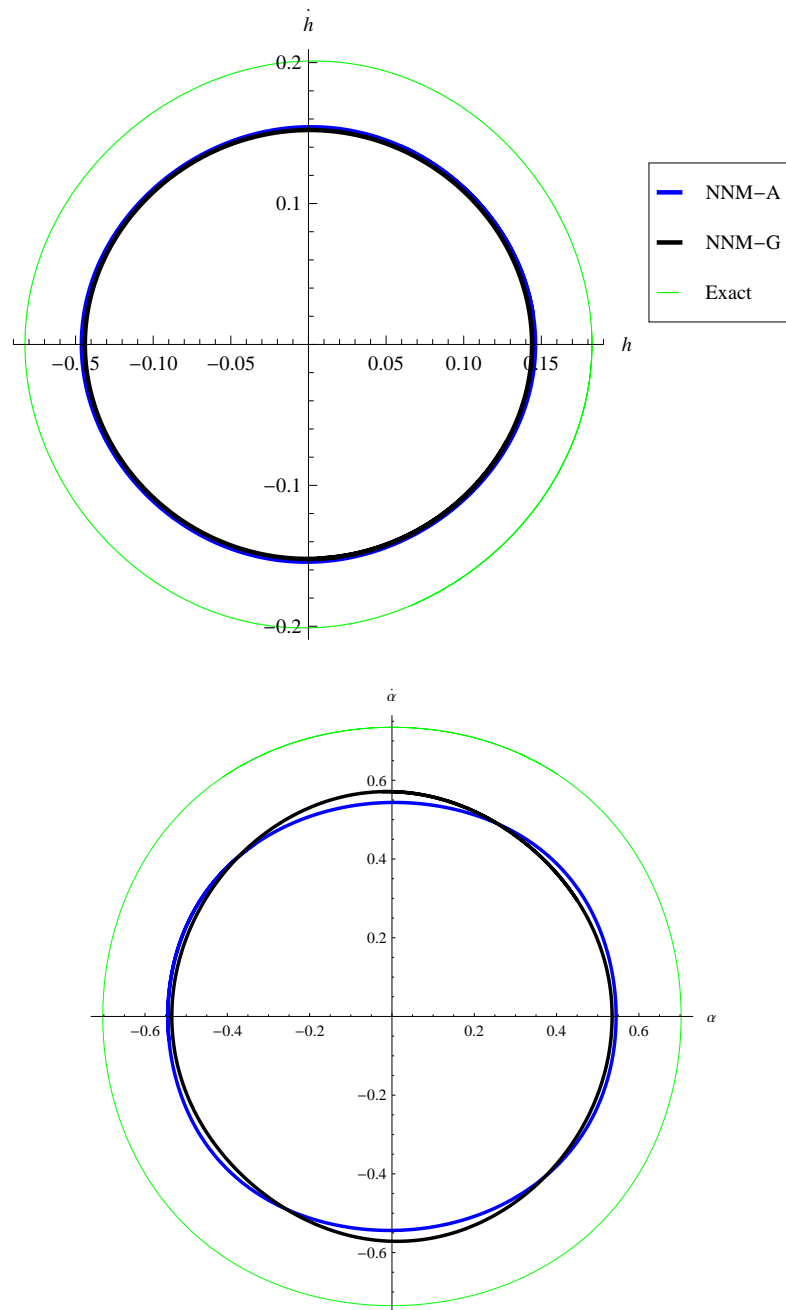


Figure 5.21: Galerkin with Integration Region $1.0 \times \text{Exact}$ Amplitudes, $1.17V_f$

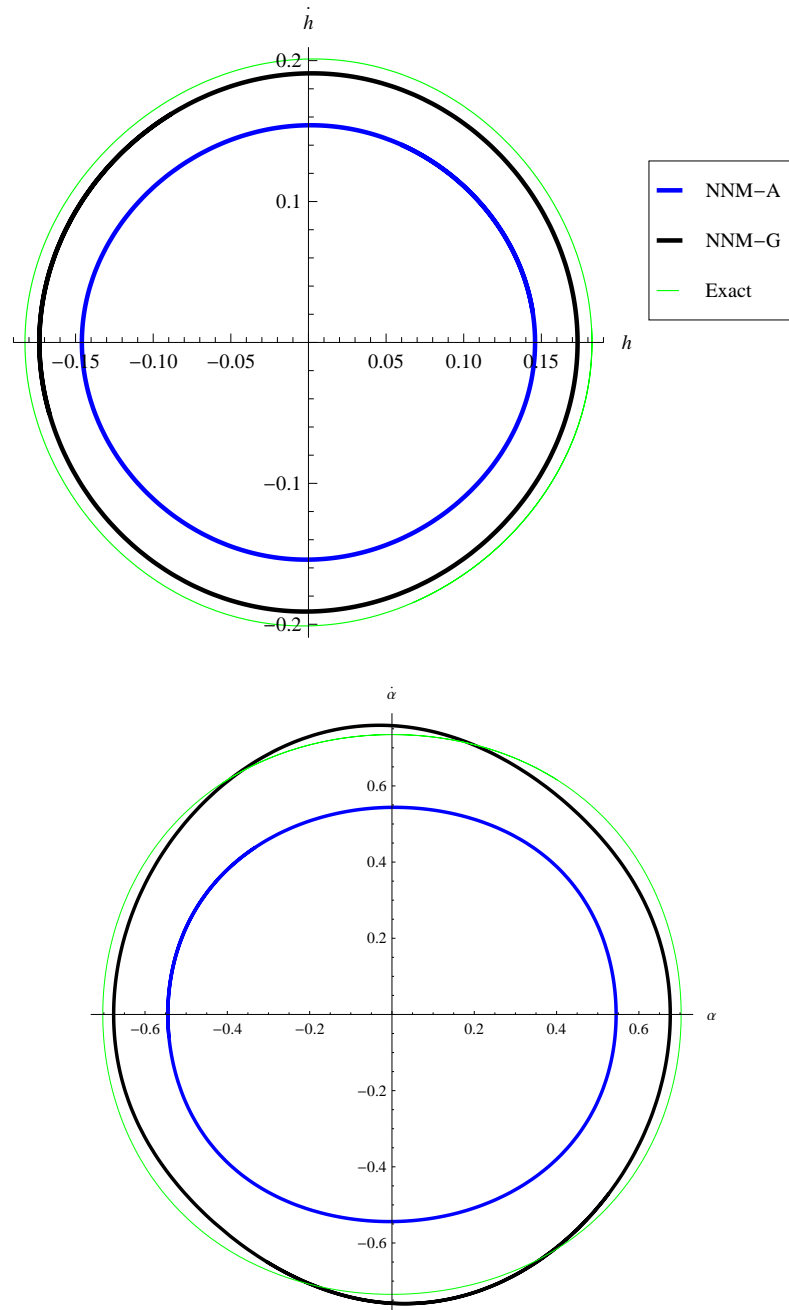


Figure 5.22: Galerkin with Integration Region $1.2 \times \text{Exact}$ Amplitudes, $1.17V_f$

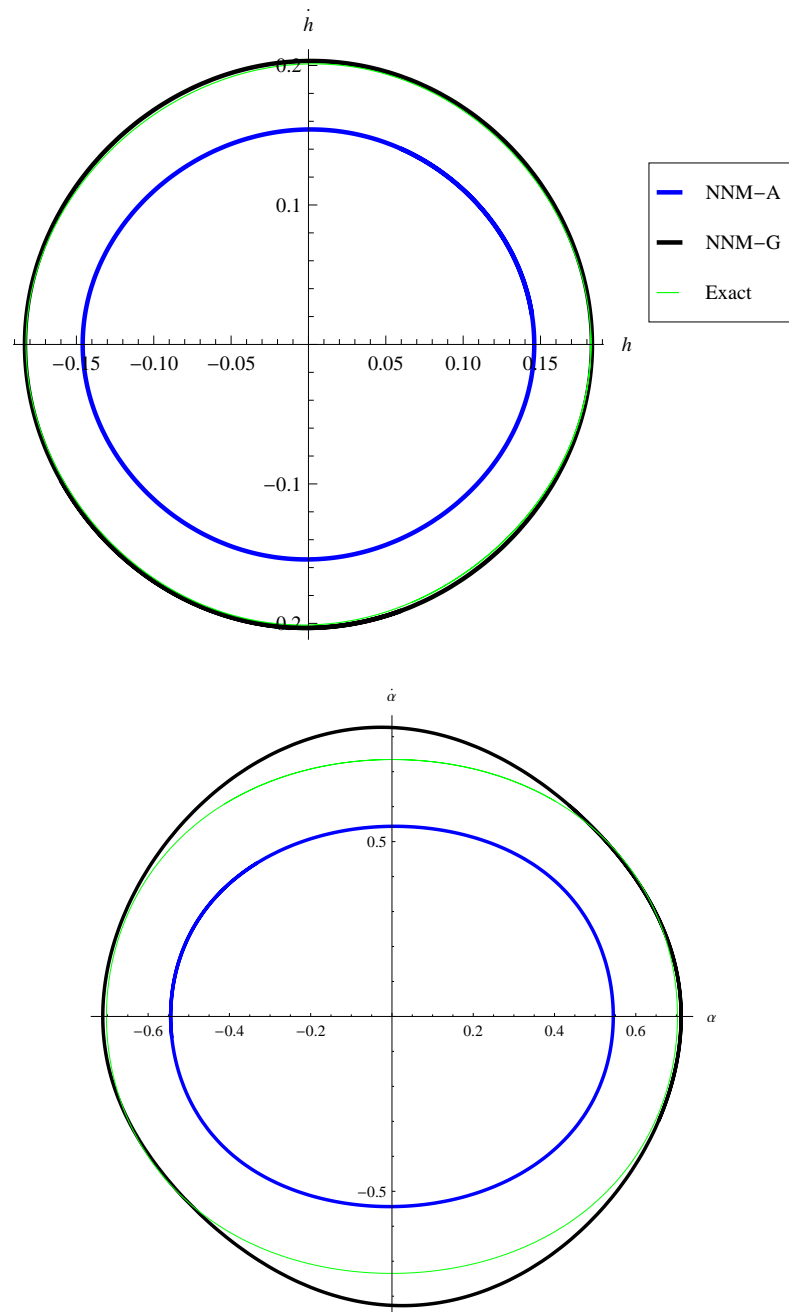


Figure 5.23: Galerkin with Integration Region $1.4 \times \text{Exact}$ Amplitudes, $1.17V_f$

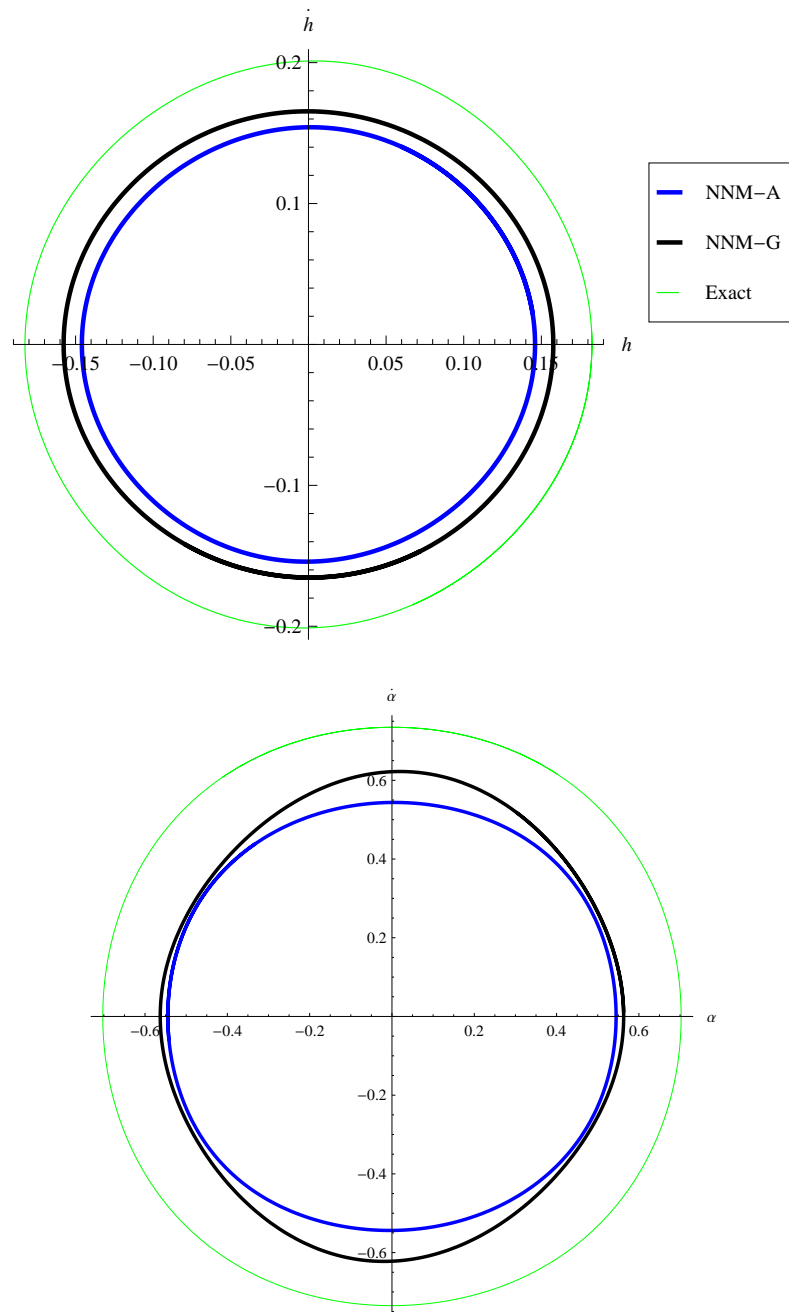


Figure 5.24: Galerkin with Integration Region $1.6 \times \text{Exact}$ Amplitudes, $1.17V_f$

Galerkin Solution at High Velocity

The velocity for the airfoil model was increased to $1.5V_f$ to determine the accuracy of the Galerkin solution with even stronger nonlinearities. The integration region was varied over the same range as in Table 5.2, but satisfactory results were not found. Figure 5.25 shows the best results that were obtained with the Galerkin method for this case. As is obvious in the figure, the Galerkin solution is no better than the asymptotic at a high velocity. The Galerkin integrals have to be taken over such a large region to encompass the LCO amplitude that the actual error for the LCO ends up being quite high.

5.2.4 Collocation Modal Coefficient Solution

The collocation method was used in an attempt to improve the results from the asymptotic method while avoiding the problems of the Galerkin method. Several results are presented here that show how well the collocation method works. The same airfoil model as in the previous sections was used.

Collocation Method at Moderate Velocities

To generate the collocation solution, a set of points must be chosen. At the moderate velocity of 1.17 times the flutter velocity, the asymptotic solution can offer a starting point for selecting these points. Even though the asymptotic solution has a fairly large error in this regime, the information is good enough for a first collocation solution. Successive iterations can be done by selecting the points from a collocation solution and repeating the collocation method with the new set of points.

Table 5.3 shows the resulting error in both amplitude and frequency of LCO after one, two, and three iterations of the collocation method. The amplitude error shown is an average of the displacement and velocity amplitudes as it seemed to be the best indicator of the solutions accuracy. Results are shown with both the linear flutter mode and airfoil plunge used as the master coordinate. The plunge master coordinate data can be compared

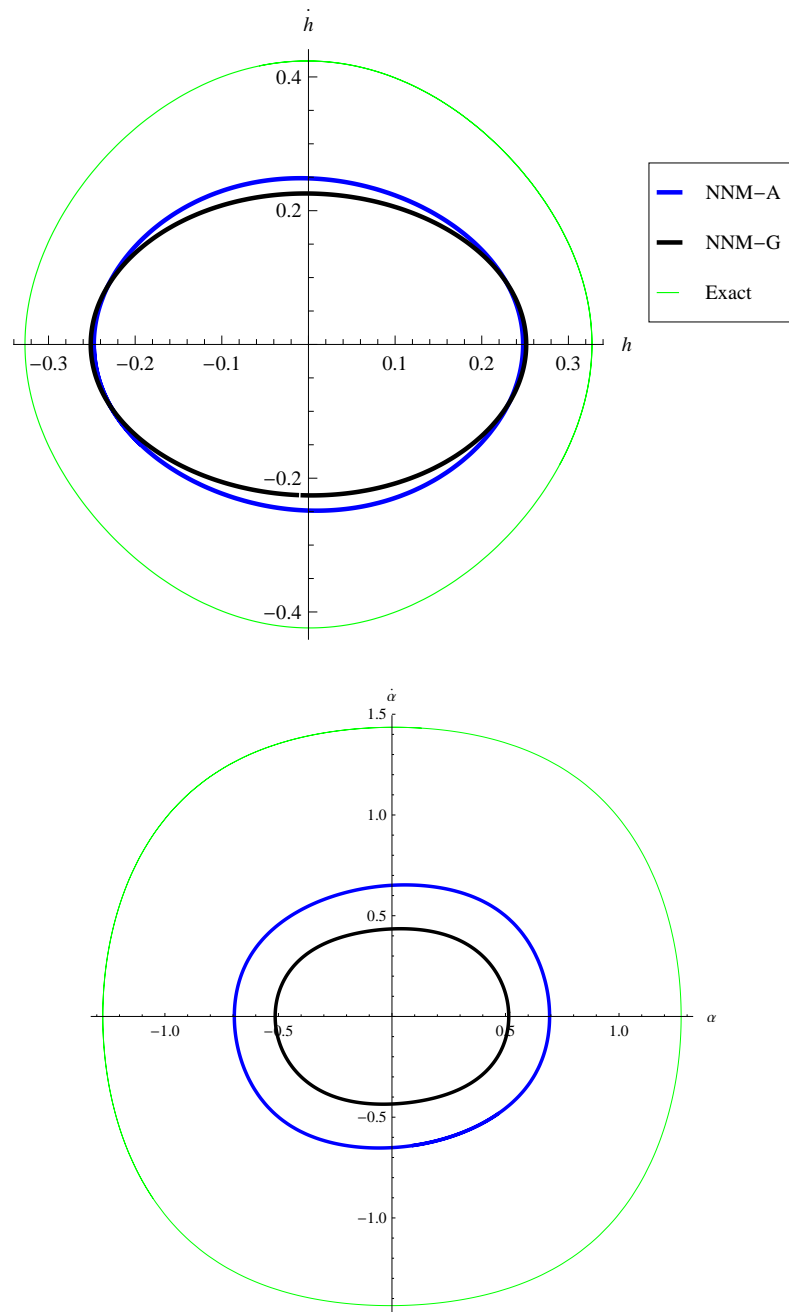


Figure 5.25: Galerkin with Integration Region $1.2 \times$ Exact Amplitudes, $1.5V_f$

Table 5.3: Collocation Results

	Solution	Percent Error	
		Frequency	Amplitude
Flutter Master Coordinate	Asymptotic	1.758	11.035
	Collocation 1	0.135	0.794
	Collocation 2	0.037	0.291
	Collocation 3	0.022	0.185
Plunge Master Coordinate	Asymptotic	3.760	22.150
	Collocation 1	1.240	6.535
	Collocation 2	0.107	0.778
	Collocation 3	0.386	1.877

directly to the previous sections since it is the exact same case and master coordinate. For each row in the table, an equally spaced set of points for the collocation solution was taken from two adjacent quadrants in the previous LCO solution. The first collocation iteration shows an excellent result in both master coordinates. With the plunge master coordinate, the error may increase or decrease for additional iterations, but generally trends downward. For the flutter mode master coordinate, additional collocation iterations provide a further decrease in error. Convergence for this technique has not been proven, but existed for several other cases tested.

Figure 5.26 compares the steady state LCO of the collocation solution using the linear flutter mode master coordinate to the asymptotic and exact results at a freestream velocity of 1.17 times the flutter velocity. This figure corresponds to the first flutter mode, collocation iteration in table 5.3. A single iteration of the collocation method shows dramatically improved results. The amplitude in this case is less than one percent in error.

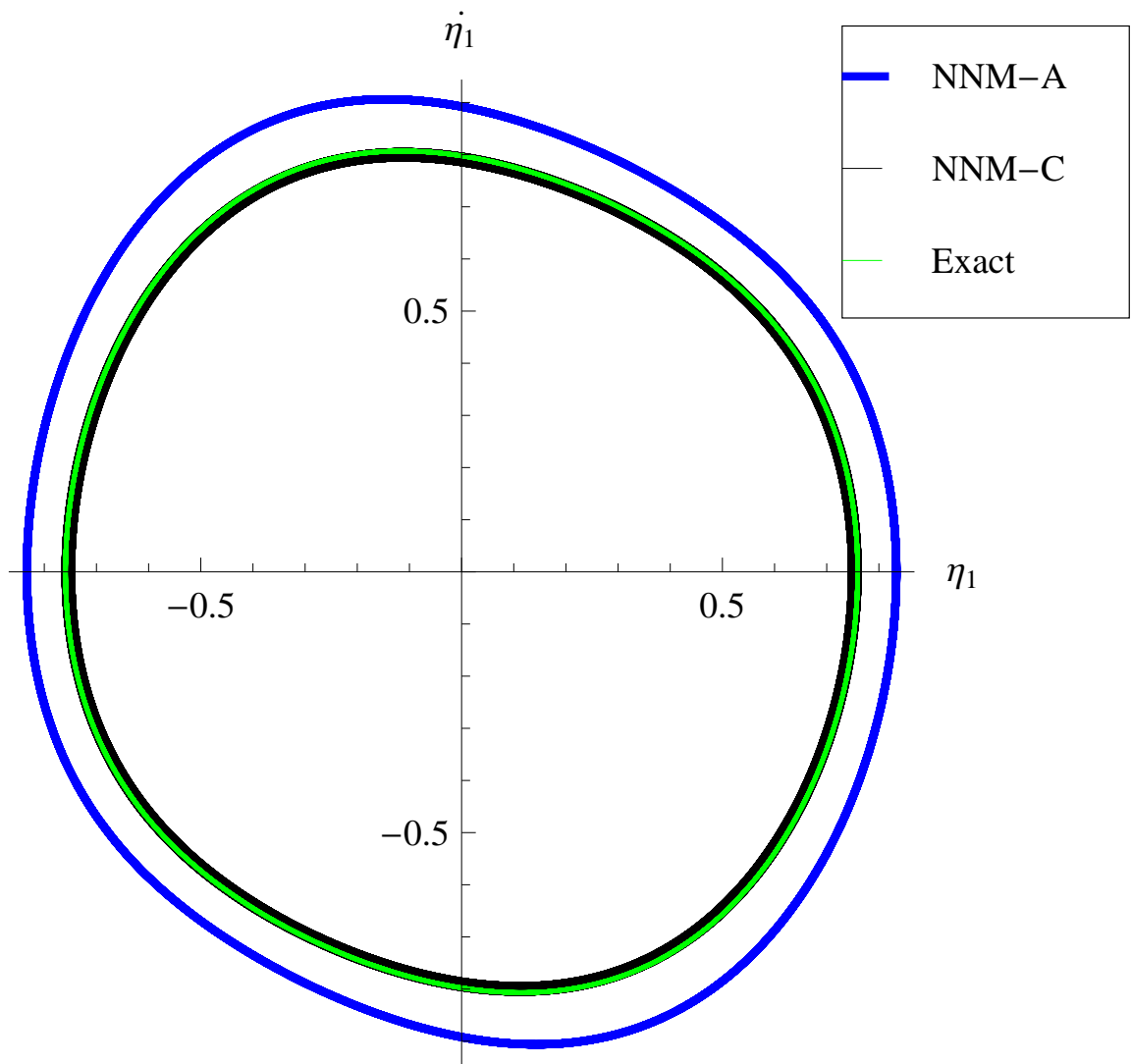


Figure 5.26: Collocation Modal Coefficient Solution Sample Results at $1.17V_f$

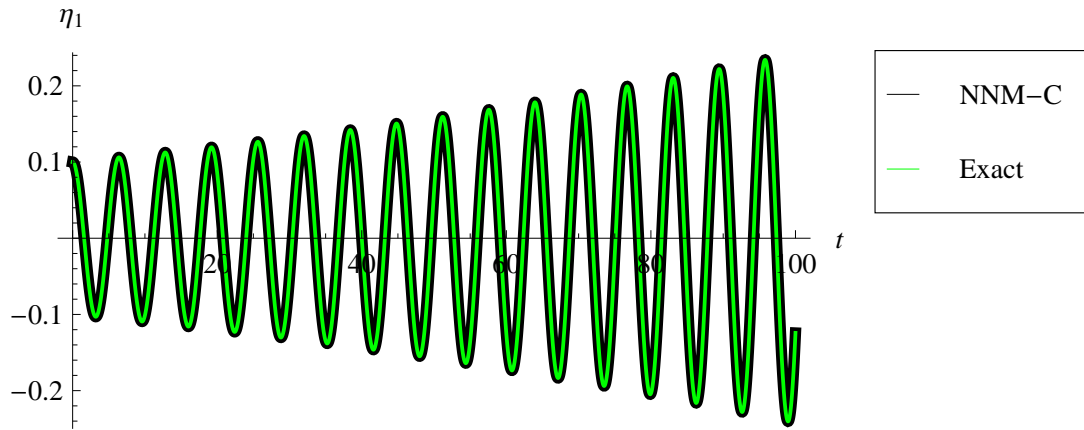
Collocation Method and Motion Growth

Since the collocation method was meant to push the error to zero on the LCO path, the accuracy of growth of the motion from the initial condition was not assured. However, the growth was actually modeled very accurately. Using a single collocation iteration, Figs. 5.27(a) through 5.27(c) were generated to show the accuracy in the growth phase of the motion from a small initial condition. After the third growth figure, the motion quickly stabilizes into the LCO shown in Fig. 5.26. As the figures show, the error during the growth is very small. The error in the moderate amplitudes has no chance to grow because it is sandwiched between two areas where the error is forced towards zero, the linear range due to exact linear coefficients and the band where the LCO occurs due to the selection of the collocation points. This demonstrates that the collocation method works very well for the growth phase as well as steady LCO.

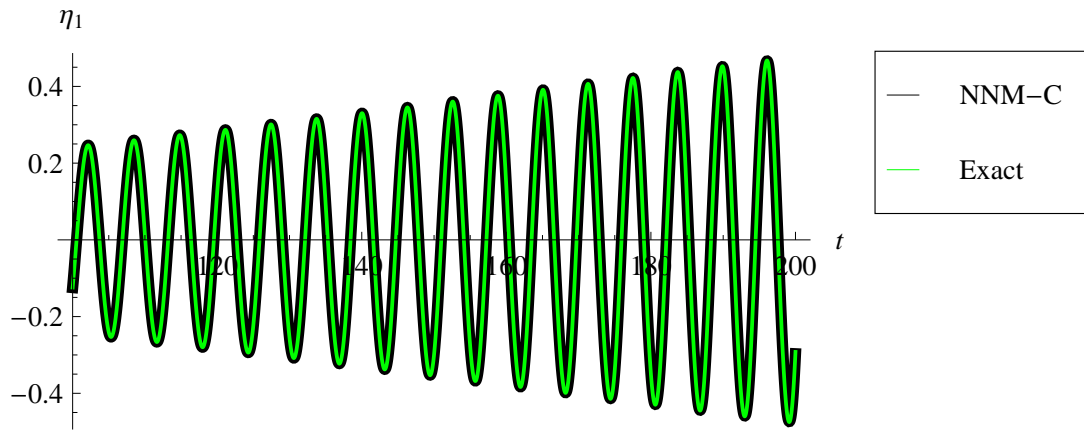
Collocation Method at High Velocities

In addition to the reduction in error at low velocities where the asymptotic solution is stable, the collocation solution remains stable at high amplitudes and velocities where the asymptotic solution is no longer stable and the Galerkin solution has not been found to offer satisfactory results. With the appropriate selection of u_i and v_i points, the collocation method offers a solution of very high accuracy even at very high velocities. However, no direct way exists to select points for the first iteration of the collocation solution. If the points chosen are too much smaller in magnitude than the LCO, the collocation solution will be unstable just like the asymptotic. Nonetheless, with a little trial and error and a simple iteration scheme an excellent solution can be found.

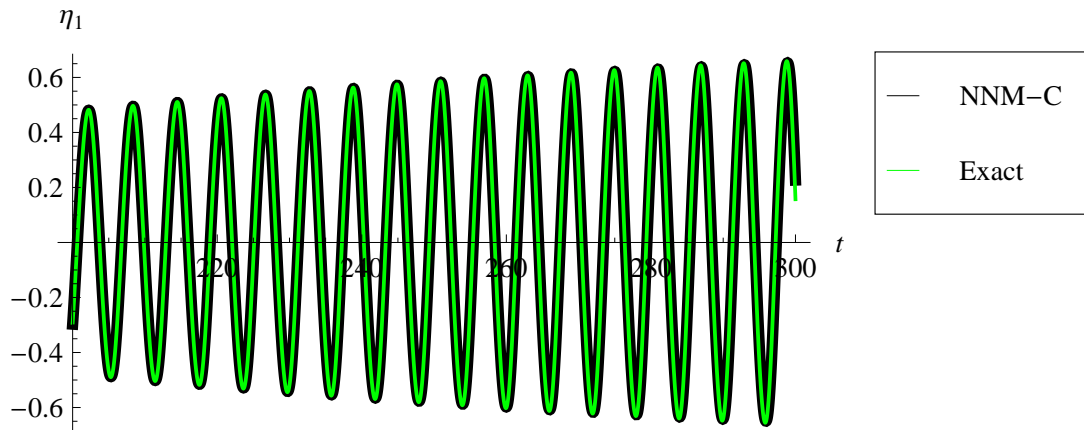
This example uses the same system as above, except the velocity has been increased to 1.5 times the linear flutter velocity. The linear flutter mode is used as the master coordinate. The exact solution could be used to select the points needed for collocation, but this does not offer a realistic example. So as a rough first guess, the collocation points from the 1.17 times the linear flutter example were doubled in magnitude. These points created a stable



(a) 0 to 100 Seconds



(b) 100 to 200 Seconds



(c) 200 to 300 Seconds

Figure 5.27: Motion Growth with Collocation Solution

collocation solution, seen in Fig. 5.28, although the error was relatively high at about 7%, 12% and 26% for the frequency, displacement amplitude, and velocity amplitudes, respectively. If a stable solution had not been found the magnitudes could have been increased further until a stable solution was reached. The former iteration method of using the previous collocation solution's points to select the next set does not work in this case. Selecting these points will generate an unstable solution. Instead, the points extracted from the new collocation solution are averaged with the points from the previous solution. If a stable solution is found, then this iteration continues. Sometimes an unstable solution will be generated. If this occurs, the current unstable set of points is averaged with the previous stable set of points. The iteration continues in this fashion until the percent step size for all the u_i and v_i points is less than 10%. Table 5.4 demonstrates this process. The boxes containing only dashes indicate that the point set was not extracted from the solution, but was taken from the previous stable set of points. As can be seen the solution converges to a very accurate result. Figures 5.28 through 5.30 correspond to the iterations listed in the table. A figure for iteration 3 is not included since it produces an unstable solution. The figures, especially the converged Fig. 5.30, clearly show the excellent accuracy of the collocation solution even for the highly nonlinear solution that cannot even be approximately captured by the asymptotic or Galerkin solutions.

5.3 Pitch-Plunge Airfoil with Unsteady Aerodynamics Sample Results

The constants from Eq. (5.1) were used with the unsteady aeroelastic equations. The dimensionless linear flutter velocity for this system is 1.699 and the linear flutter velocity is 0.1387 Hz. Since the linear flutter mode has been established as the preferred master coordinate and the first-order formulation already had to be used due to the unsteady aerodynamics, the linear flutter mode was selected as the master coordinate for this test case. As previously discussed in the master coordinate section, the two first-order modal degrees of freedom that

Table 5.4: Collocation Iteration at a High Velocity

Iteration	Collocatoin Points				Error			Percent Step Size	
	Used		Extracted		Frequency	Displacement Amplitude	Velocity Amplitude	u_i	v_i
	u_i	v_i	u_i	v_i					
1	1.66	0	1.22	0	6.689	16.297	25.598	N/A	N/A
	1.12	1.24	0.79	0.93					
	0	1.6	0	1.06					
	-1	1.16	-0.55	0.82					
2	1.44	0	1.35	0	3.082	6.485	10.888	-13.3	-
	0.96	1.09	0.87	1.04				-14.7	-12.5
	0	1.33	0	1.17				-	-16.9
	-0.78	0.99	-0.56	0.92				-22.5	-14.7
3	1.40	0	-	-	unstable solution	unstable solution	unstable solution	-3.1	-
	0.91	1.06	-	-				-4.5	-2.1
	0	1.25	-	-				-	-6.0
	-0.67	0.96	-	-				-13.9	-3.5
4	1.42	0	1.45	0	0.29	0.95	0.94	-1.6	-
	0.93	1.07	0.94	1.13				-2.2	-1.0
	0	1.29	0	1.25				-	-3.0
	-0.72	0.97	-0.57	0.99				-6.9	-1.8

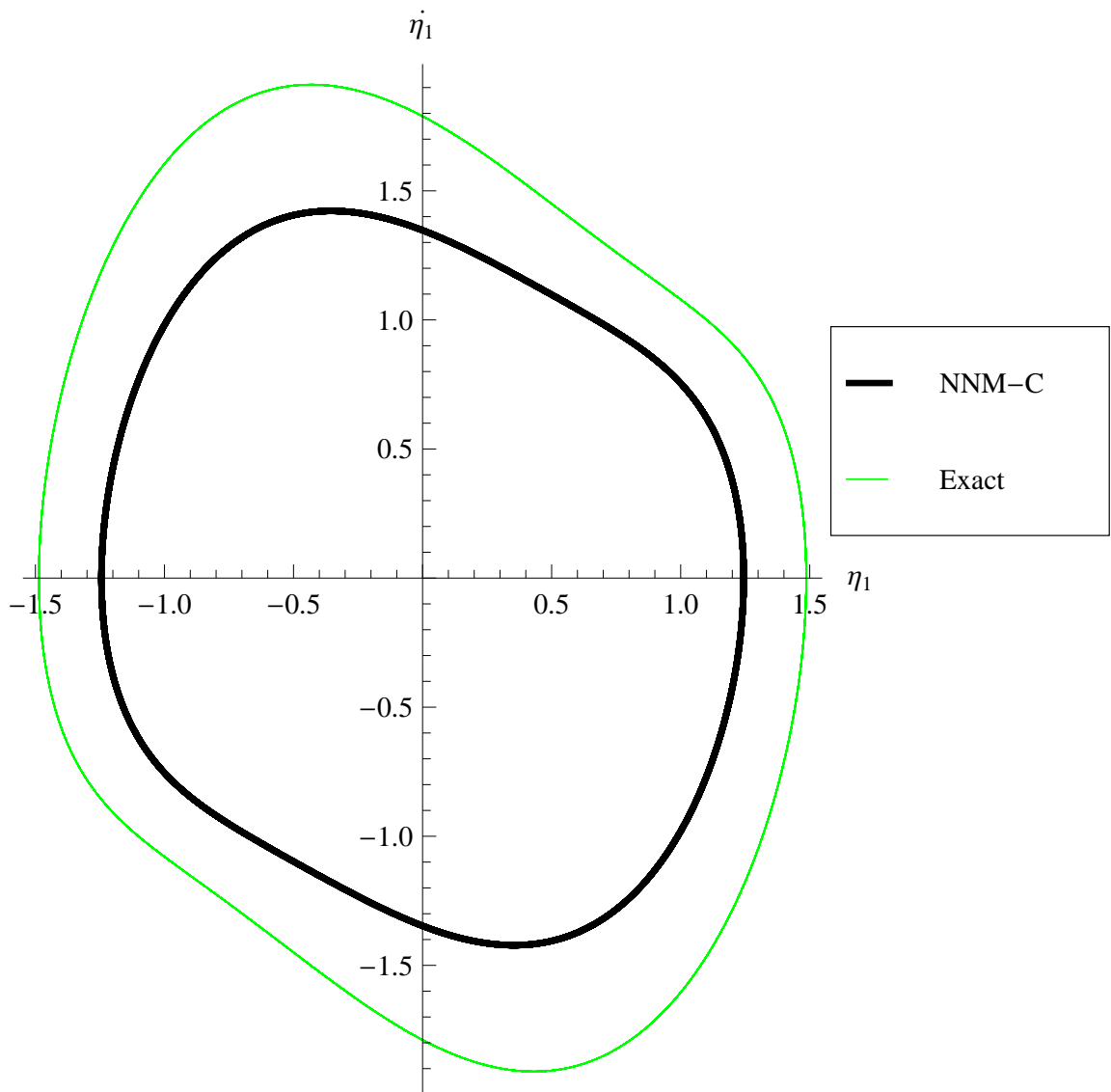


Figure 5.28: Collocation Iteration 1 at $1.5V_f$

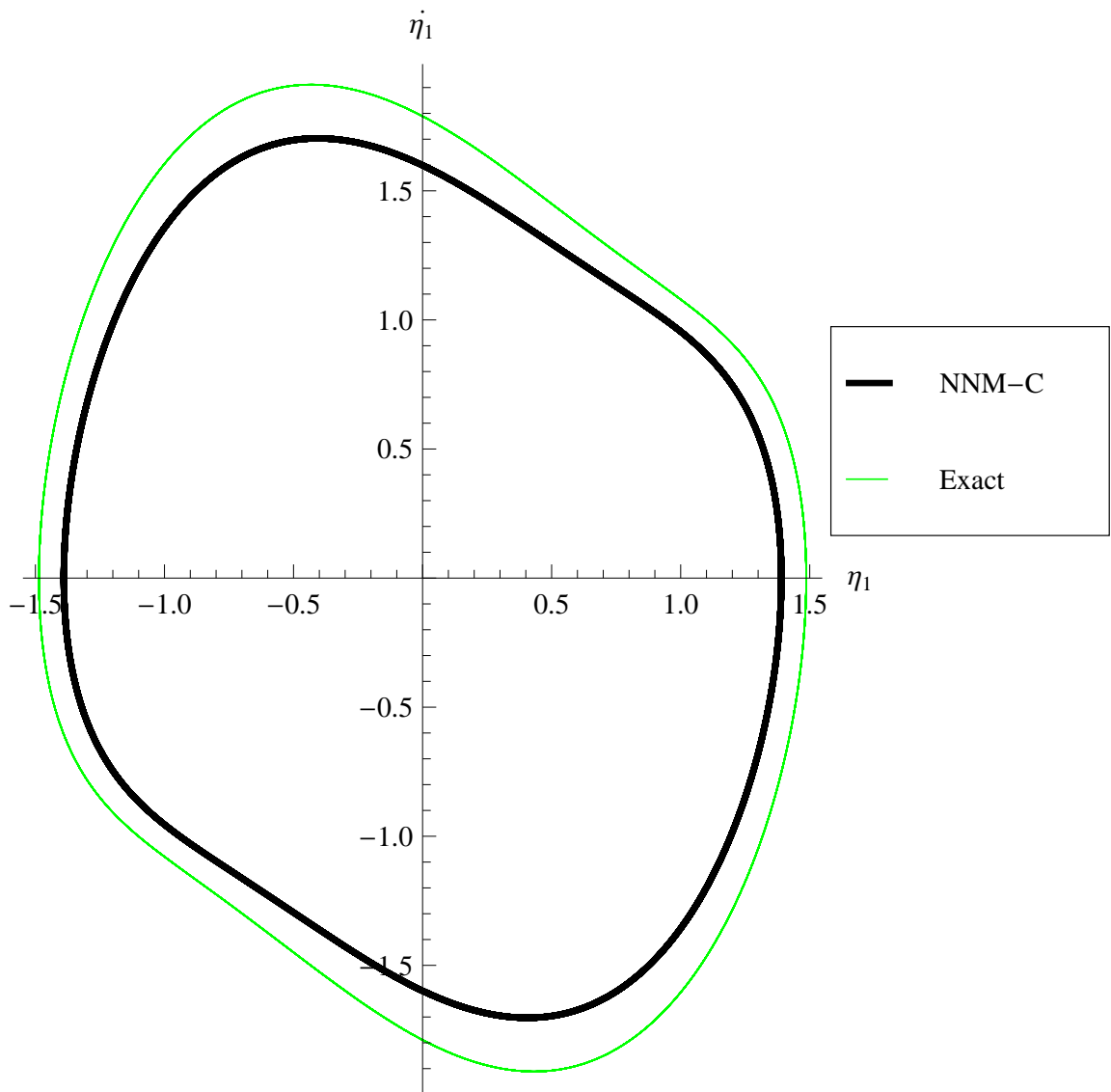


Figure 5.29: Collocation Iteration 2 at $1.5V_f$

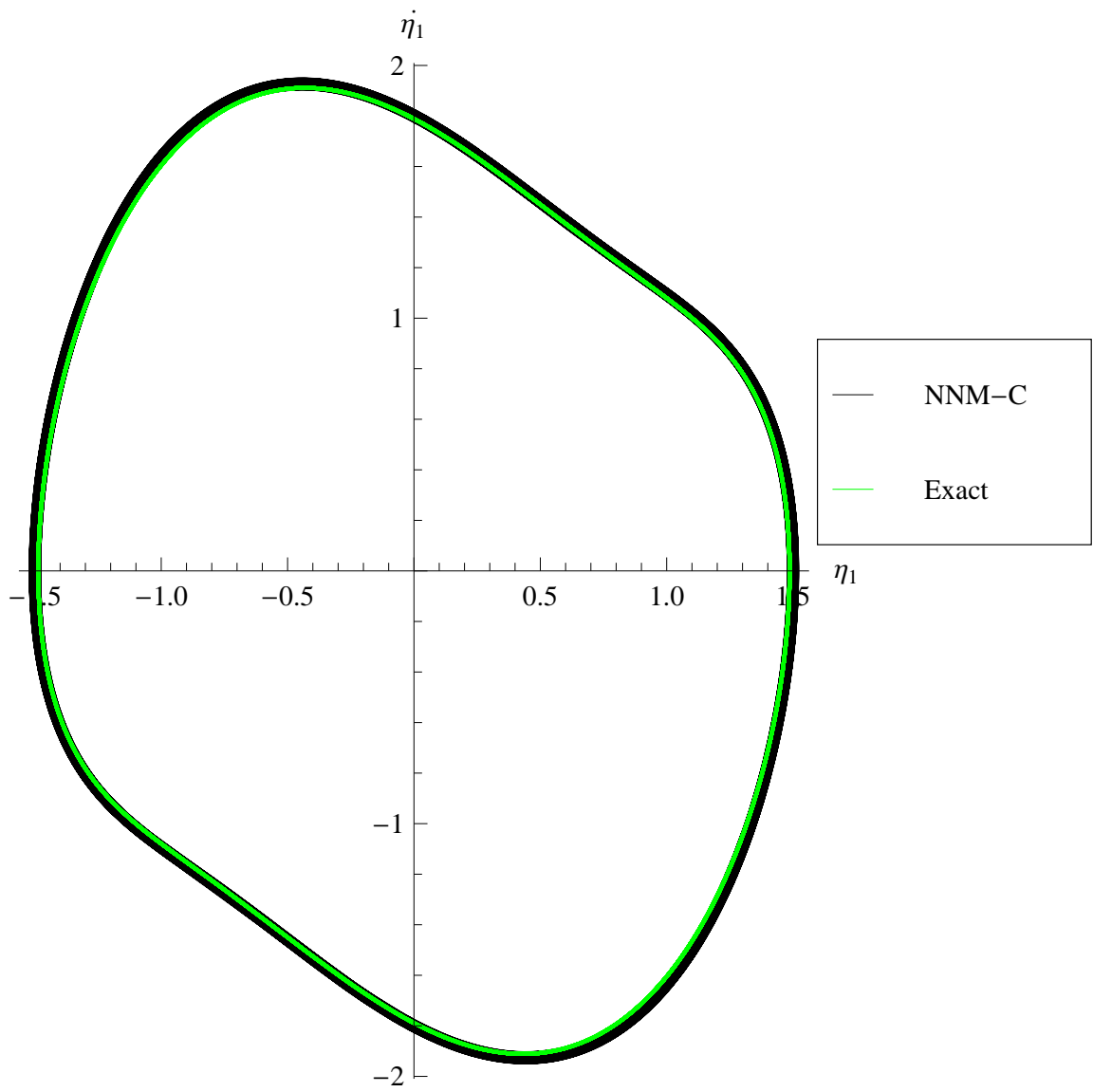


Figure 5.30: Collocation Iteration 4 at $1.5V_f$

correspond to the linear flutter mode must be selected. If the first-order degrees of freedom corresponding to the damped linear mode are selected the LCO will cannot be found only the damped motion can be found. With the linear flutter mode as the master coordinate, the linear modal coefficients are exactly zero and only a single NNM is found. If another master coordinate were used, pitch for instance, there would be three real solutions to the linear modal coordinates. With the corresponding nonlinear coefficient solutions, these would create be two meaningful NNMs corresponding to the LCO mode and the damped mode. The third is an aerodynamic "lag" mode and does not produce a meaning physical motion. Obviously the use of the linear flutter mode simplifies the process and results.

The final result of using the linear flutter mode on the unsteady aeroelastic system is a single set of coupled first-order equations.

$$\begin{aligned}
 \dot{u} = & u(0.0769 + 0.00524u^2 + 0.1301v^2 - 0.001716u^4 + 0.0241u^2v^2 + 0.0455v^4 \\
 & + 0.0001875u^6 - 0.001861u^4v^2 + 0.00566u^2v^4 + 0.00530v^6 \\
 & - 6.83 \times 10^{-6}u^8 - 0.000254u^6v^2 - 0.0001571u^4v^4 + 0.000340u^2v^6 + 0.000205v^8) \\
 & + v(-0.728 - 0.0452u^2 - 0.1247v^2 + 0.00357u^4 - 0.0686u^2v^2 - 0.0421v^4 \\
 & + 0.000840u^6 - 0.00653u^4v^2 - 0.01373u^2v^4 - 0.00474v^6 \\
 & - 0.0000754u^8 - 0.000229u^6v^2 - 0.000781u^4v^4 - 0.000741u^2v^6 - 0.0001777v^8)
 \end{aligned} \tag{5.12}$$

$$\begin{aligned}
 \dot{v} = & u(0.728 + 0.00844u^2 + 0.210v^2 - 0.00277u^4 + 0.0388u^2v^2 + 0.0733v^4 \\
 & + 0.000302u^6 - 0.00230u^4v^2 + 0.00913u^2v^4 + 0.00854v^6 \\
 & - 0.00001101u^8 - 0.000409u^6v^2 - 0.000253u^4v^4 + 0.000548u^2v^6 + 0.000331v^8) \\
 & + v(0.0769 - 0.0729u^2 - 0.201v^2 + 0.00575u^4 - 0.1106u^2v^2 - 0.0679v^4 \\
 & + 0.001354u^6 - 0.01053u^4v^2 - 0.0221u^2v^4 - 0.00764v^6 \\
 & - 0.0001215u^8 - 0.000368u^6v^2 - 0.001259u^4v^4 - 0.001194u^2v^6 - 0.000287v^8)
 \end{aligned} \tag{5.13}$$

The Runge-Kutta simulation of these equations is compared to linear normal modes and the

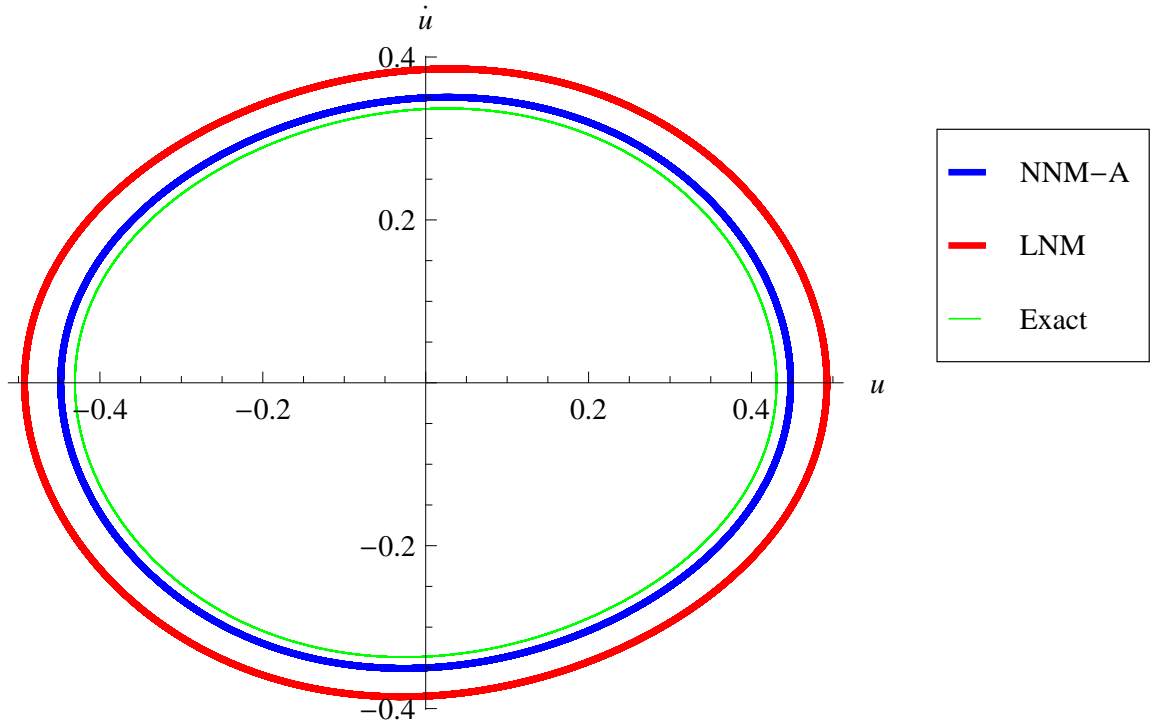


Figure 5.31: Steady LCO results at $\bar{u} = 1.05V_f$ for Linear Flutter Mode - US Aero

exact equations in Figs. 5.31 and 5.32. The figures represent the results at a freestream velocity of 1.05 and 1.17 times the linear flutter velocity, respectively. As with the quasi-steady results, the NNM works well at lower amplitudes and the error increases when the amplitude was increased. The NNM always performs better than the LNM as in other cases. As can be seen, especially in the higher velocity case, the phase space plot is the same shape for the unsteady aerodynamics as it is in the quasi-steady aerodynamic cases. This difference in the physical nature of the motion is also captured by the NNM solution. The difference can be seen in Fig. 5.33 where the unsteady and quasi-steady solutions have been normalized by their magnitudes and plotted together.

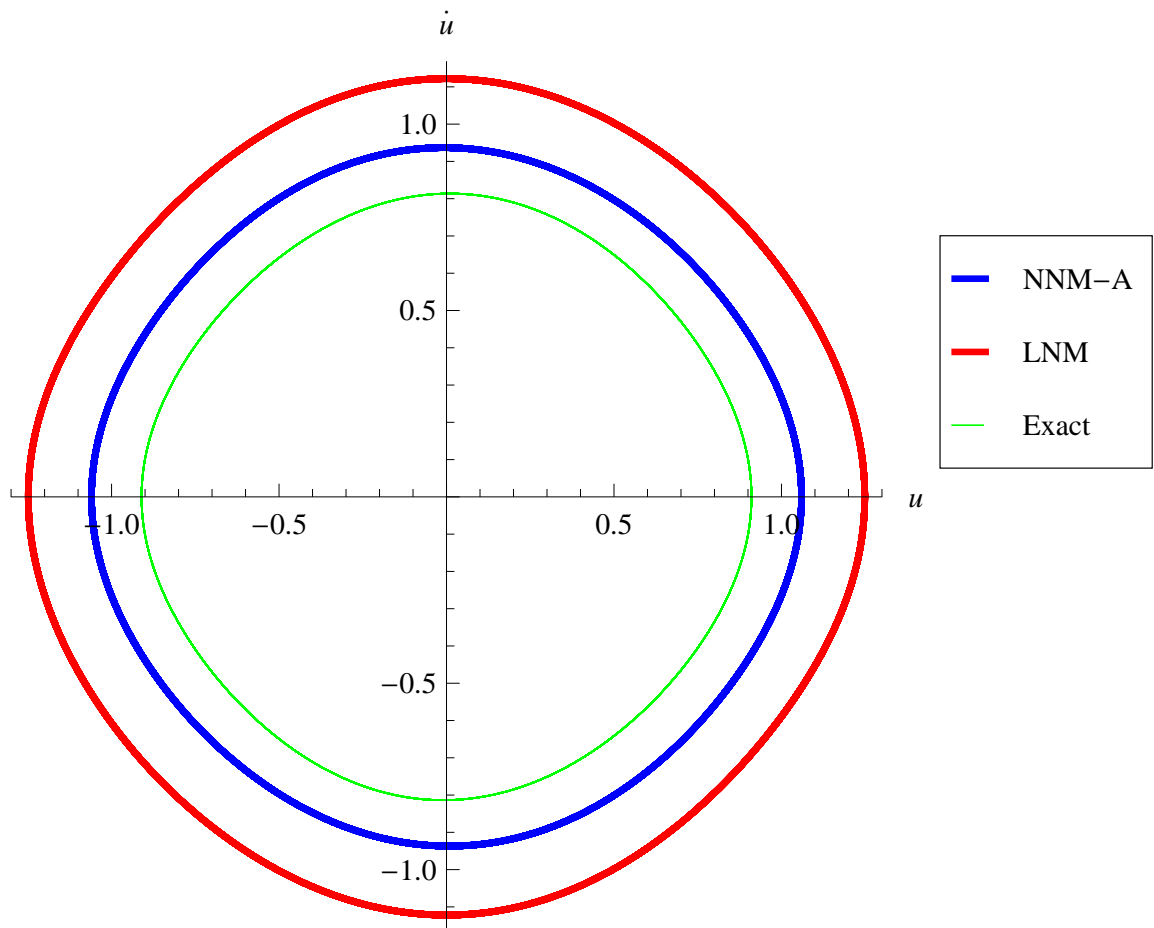


Figure 5.32: Steady LCO results at $\bar{u} = 1.17V_f$ for Linear Flutter Mode - US Aero

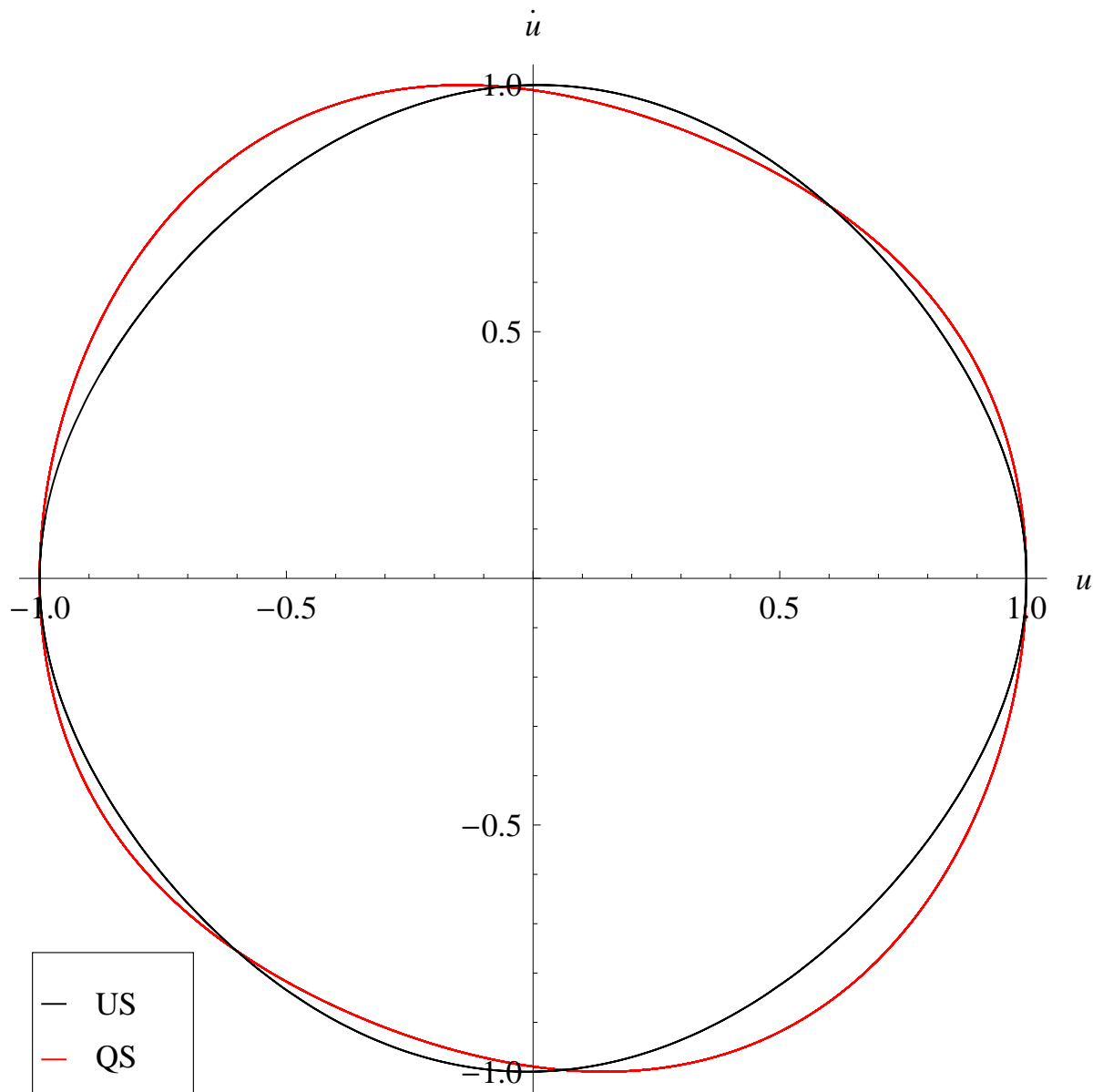


Figure 5.33: Normalized Unsteady (US) vs. Quasi-steady (QS) LCO solution at $1.17V_f$

5.4 Goland Beam Wing

The Goland wing model was used to demonstrate the method with a more realistic system containing more degrees of freedom. Nonlinearities were provided by a cubic stall-like term in the quasi-steady aerodynamic equations. The beam model was discretized with orthogonal polynomials that satisfied all the beam boundary conditions via the assumed modes method and Lagrange's equations. The orthogonal polynomials were chosen over the exact beam bending and torsion mode shapes because the polynomials process much faster. The discretized beam system from Eq. (4.16) was multiplied by the inverse of the mass matrix so the assumed beam modes could be used directly as master coordinates for the NNM solution method. This is similar to what was referred to as the M^{-1} master coordinate in previous sections. Because the LCO was composed primarily of the first torsion shape, the importance of picking the first torsion mode shape as the master coordinate was quickly realized. If the first bending or other shapes were chosen, the linear modal coefficients were very large. When the large linear coefficients were used in the asymptotic, nonlinear coefficient equations computational errors resulted. As such the first torsion shape was always used as the master coordinate.

For the case studied, the standard set of constants for the Goland wing were used[42].

$$\begin{aligned}l &= 20\text{ft} \\b &= 3\text{ft} \\m &= 0.746\text{slug/ft} \\I_y &= 1.943\text{slug ft}^2/\text{ft} \\S_y &= 0.447\text{slugft/ft} \\EI &= 23.6 \times 10^6\text{lbft}^2 \\GJ &= 2.39 \times 10^6\text{lbft}^2 \\a &= -0.34 \\C_{l\alpha} &= 2\pi\end{aligned}\tag{5.14}$$

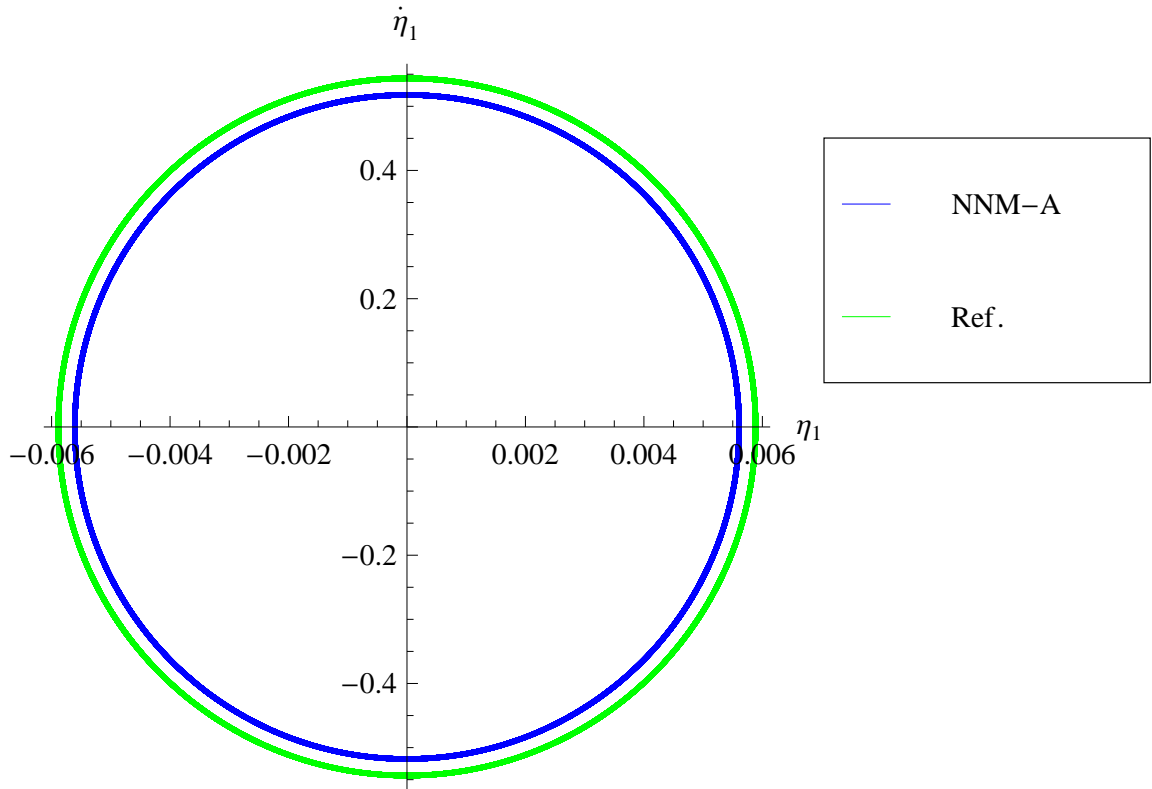


Figure 5.34: Goland Wing with 5 Bending and 5 Torsion Modes

The sample results appearing in this section were obtained at 1.05 times the flutter velocity. Figure 5.34 shows a sample of the results obtained. The reference solution was obtained from a simulation of the discretized beam system with all ten modes and the NNM result in this figure also included all the modes. In the figure η_1 corresponds to the first torsion mode since it is the master coordinate. A good agreement was found between the NNM and reference solution. As typical with previous results, the amplitude matched well and the frequency matched very well.

5.4.1 Modal Truncation

When linear modal analysis is used to model linear systems, it is often found that only a few important modes need to be included in the solution to get results nearly as accurate as

with the inclusion of many modes. Since this beam model includes as many as ten modes, a NNM solution was produced using two, four, six, eight, and ten modes. Each solution has an equal number of bending and torsion modes. All the systems were run at a velocity of 1.05 times the linear flutter velocity of the ten mode system. Table 5.5 shows the linear flutter velocity for each system and the actual ratio of the test speed to the flutter velocity. Studying the results of the series of NNM solutions shows that modal truncation can be extended to nonlinear normal modes. Certain modes can be excluded without much loss in accuracy based on the values of the linear and nonlinear modal coefficients.

Figure 5.35 shows the two, four, and ten mode NNM solution as compared to the reference solution for ten modes. This figure shows that the four mode solution does basically the same job as the ten mode solution which is the first indication that modal truncation will work. A plot of the amplitude percent error vs. the number of included modes is shown in Fig. 5.36. Here the amplitude error is the average of the displacement and velocity errors of the first torsion mode. The amplitude average gives the best indication of the solution's error. The plot indicates that the error for the four mode solution is only just slightly more than the ten mode solution and the six and eight mode solutions are indistinguishable from the ten mode solution. This can be verified by looking at Table 5.6. The amplitude and frequency errors are shown for each of the solutions. When moving from a four to a ten mode solution, only a 5% relative and 0.28% absolute reductions in the error are achieved.

The times required for each of the beam solutions are shown in Table 5.7. The time for simulation of the full order and reduced order reference modes are shown. As the number of included modes is increased the time for the NNM solution reduces when compared to the simulation of the reference system. The time required for 10 mode NNM solution is much better than for the full order reference solution. When compared to reduced order NNM solutions (with 4 or 6 modes), the advantage of the NNM solution is even greater.

Table 5.6 also shows another useful result. The error of each solution has approximately the same error when compared to a reduced-order reference solution using the same number of modes as the NNM solution. The two mode solution shows a slightly better result,

but this is explained by the fact that LCO found is of a lower amplitude. The consistency in error is important because it shows that there is no error increase due to using additional slave coordinates. As such, the only hindrance to increasing the number of modes is increased computational time to process the extra modes.

One further important result is obtained by looking at the modal coefficients for each of the slave modes. Table 5.8 shows the modal coefficients and Table 5.9 shows the normalized modal coefficients for all the slave modes. Each column in the tables corresponds to the identified beam mode. The first six rows correspond to a_{1i} through a_{9i} from the modal approximation function in Eq. (3.5). The third, fourth, and fifth constants are left out since they are exactly zero (the system does not have any quadratic nonlinearities). The bottom six rows likewise correspond to b_{1i} through b_{9i} . To generate the values in the normalized table, the absolute value of each modal coefficient was taken and then they were normalized by the maximum coefficient in each row. The normalization makes it easier to see which modes have the highest magnitude coefficients.

The coefficients indicate the strength of the coupling of each slave mode with the linear and nonlinear combinations of the master mode's displacement and velocity. For instance, in the table with the direct modal coefficients the b_{6i} term is very large in the first bending mode. This indicates a very strong coupling between the cube of first torsion mode's displacement and the velocity of the first bending mode.

Looking back at Eq. (3.5), it is apparent that the magnitude of the modal coefficients is indicative of the importance of each term. Comparing the magnitudes of the coefficients from the different modes tells which ones are most active in the final motion. The columns (modes) with the largest numbers are the most strongly coupled with the motion of the master coordinate and are therefore the most important to include in the solution. The normalized table indicates that the most important slave modes to include are the first and second bending modes and the second torsion mode. Beyond those modes the indicated importance drops off quickly. It is interesting to note, that for this case the same conclusion could have been drawn from looking at the results of the linear analysis and comparing

Table 5.5: Beam Wing Flutter Velocities and Run Speeds

Modes	Flutter Velocity	V/Vf
10	291.65	1.0500
8	291.65	1.0500
6	291.65	1.0500
4	291.69	1.0499
2	293.57	1.0431

Table 5.6: Beam Wing Error

Modes	Percent Error			
	Vs. 10 Mode Reference Solution		Vs. Reduced-Order Reference Solution	
	Amplitude Average	Frequency	Amplitude Average	Frequency
10	4.73	0.05	4.73	0.05
8	4.72	0.05	4.72	0.05
6	4.74	0.03	4.73	0.03
4	5.01	0.05	4.76	0.08
2	7.96	0.61	3.66	0.02

the change in linear flutter velocity; however, not nearly as much information on physical nature of the motion is available in the linear results. The most important modes in the linear system will have the highest linear coefficients, but the nonlinear coefficients will not necessarily follow that trend.

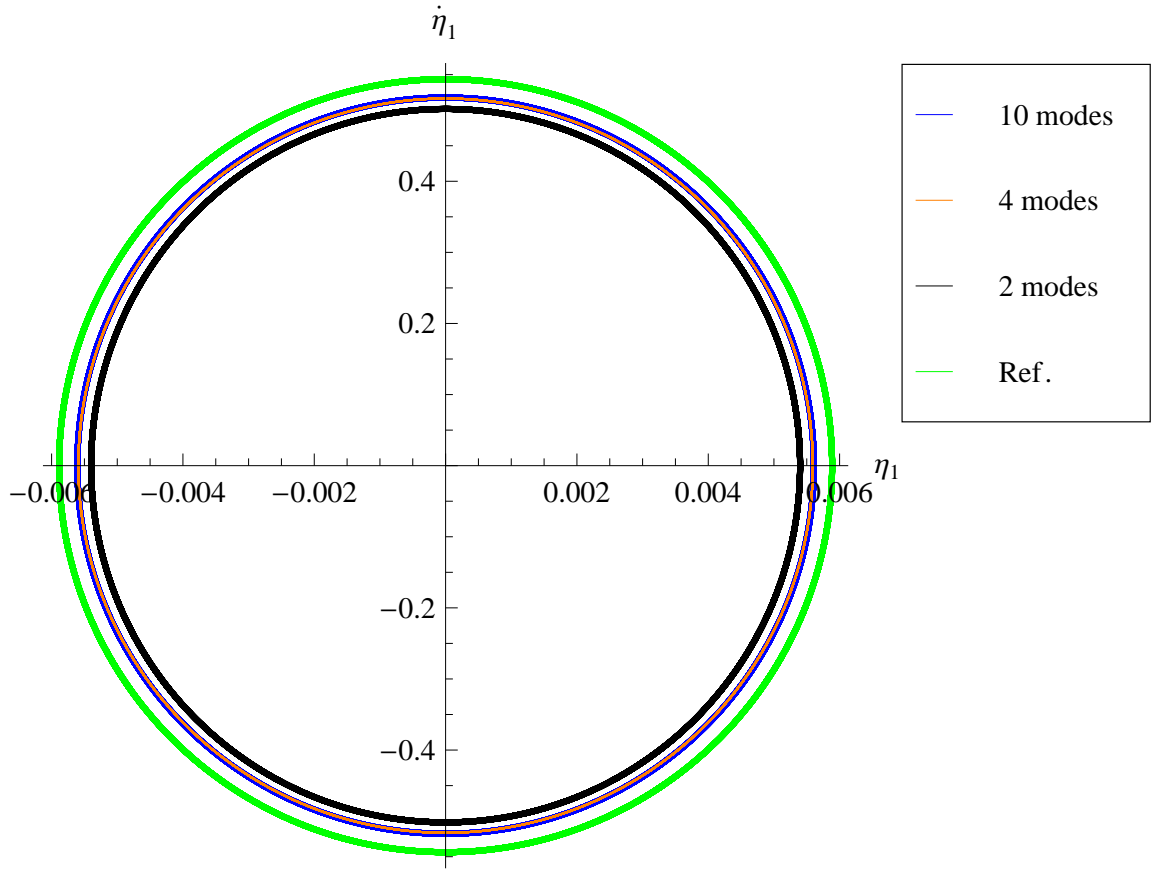


Figure 5.35: Goland Wing with Multiple Modal Solutions

Table 5.7: Beam Wing CPU Times in Seconds

Number of Modes	10	8	6	4	2
NNM Simulation	86.5	27.0	12.53	5.25	2.77
NNM Creation	302	89.0	20.2	5.25	0.0780
NNM Total	388	116.0	32.7	10.50	2.84
Reference Simulation	851	96.6	24.1	6.74	1.047

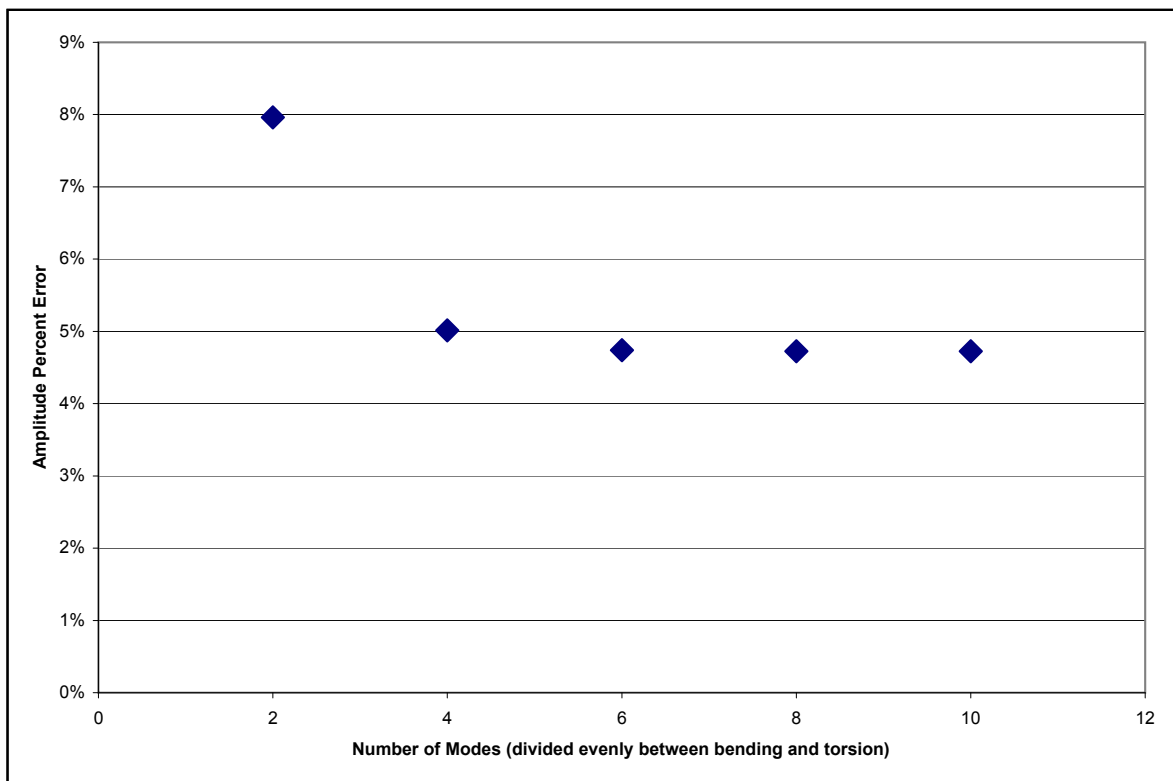


Figure 5.36: Goland Wing LCO Amplitude Error vs. Number of Modes

Table 5.8: Beam Wing Modal Coefficients

		Bending Modes				
		1	2	3	4	5
Position Coefficient $X_{i[u,v]}$	1	0.0395	0.0382	0.01640	-0.00269	-0.000311
	2	0.0001340	5.29E-05	5.96E-06	-3.56E-06	2.13E-06
	6	-1160	-443	-284	-397	-193.4
	7	-4.55	-1.509	0.221	0.1890	-0.391
	8	-1419	-0.0610	-0.01254	0.00989	0.00218
	9	-0.000515	-0.000217	-4.15E-05	9.06E-06	-8.57E-07
Velocity Coefficient $Y_{i[u,v]}$	1	-1.134	-0.448	-0.0505	0.0301	-0.01804
	2	0.0395	0.0382	0.01640	-0.00269	-0.000310
	6	38190	12648	-1888	-1591	3308
	7	-0.1219	-296	-638	-1359	-617
	8	3.89	2.46	1.490	0.1534	-0.760
	9	-0.1224	-0.0612	-0.01258	0.00990	0.00218

		Torsion Modes			
		2	3	4	5
Position Coefficient $X_{i[u,v]}$	1	0.406	-0.1812	-0.0561	0.01401
	2	0.00001132	1.161E-05	-3.34E-06	3.48E-07
	6	-70.2	-139.1	-189.3	-149.7
	7	-0.840	-0.603	0.801	0.0290
	8	-0.01548	-0.01271	0.01632	0.00683
	9	-2.51E-05	-3.60E-05	-1.5E-05	-5.82E-06
Velocity Coefficient $Y_{i[u,v]}$	1	-0.0958	-0.0983	0.0282	-0.00294
	2	0.406	-0.1812	-0.0561	0.01401
	6	7086	5073	-6773	-246
	7	51.2	-202	-844	-565
	8	-1.052	-0.300	1.990	0.209
	9	-0.01551	-0.01275	0.01631	0.00683

Table 5.9: Normalized Beam Wing Modal Coefficients

		Bending Modes					Torsion Modes			
		1	2	3	4	5	2	3	4	5
Normalized Position Coefficient $\xi_{i[u,v]}$	1	0.10	0.09	0.04	0.01	0.00	1.00	0.45	0.14	0.03
	2	1.00	0.39	0.04	0.03	0.02	0.08	0.09	0.02	0.00
	6	1.00	0.38	0.24	0.34	0.17	0.06	0.12	0.16	0.13
	7	1.00	0.33	0.05	0.04	0.09	0.18	0.13	0.18	0.01
	8	1.00	0.00	0.00	0.00	0.00	0.00	0.00	0.00	0.00
	9	1.00	0.42	0.08	0.02	0.00	0.05	0.07	0.03	0.01
Normalized Velocity Coefficient $\eta_{i[u,v]}$	1	1.00	0.39	0.04	0.03	0.02	0.08	0.09	0.02	0.00
	2	0.10	0.09	0.04	0.01	0.00	1.00	0.45	0.14	0.03
	6	1.00	0.33	0.05	0.04	0.09	0.19	0.13	0.18	0.01
	7	0.00	0.22	0.47	1.00	0.45	0.04	0.15	0.62	0.42
	8	1.00	0.63	0.38	0.04	0.20	0.27	0.08	0.51	0.05
	9	1.00	0.50	0.10	0.08	0.02	0.13	0.10	0.13	0.06

Chapter 6

Conclusions

There exists a need for a nonlinear analysis method that can capture limit cycle oscillation in aeroelastic systems and simultaneously offer insight in the physical mechanisms of the motion. This dissertation set out with the goal of exploring and developing the nonlinear normal mode method to fill this niche. Along the way, many important discoveries were made.

Nonlinear normal modes were shown to be capable of modeling limit cycle oscillation in a simple spring-mass-damper system and in several aeroelastic systems. A first-order formulation of nonlinear normal modes enabled both modeling of first-order aerodynamic equations appearing in systems with unsteady aerodynamics and use of the linear flutter mode as the master coordinate. The master coordinate used in the creation of the nonlinear normal mode was shown to have importance in the accuracy of the results. For the aeroelastic systems examined, the linear flutter mode generally performed best out of the master coordinates studied. As the master coordinate, the linear flutter mode was most representative of the final motion and the author suspects this observation can be generalized to other systems.

The eigenvalue method to solve for the linear modal coefficient was found to be preferable regardless of which coefficient solution method was used for the nonlinear coefficients. The asymptotic coefficient solution method was found to adequately model LCO for velocities

near the linear flutter velocity where the nonlinearities were weak. The Galerkin coefficient solution method can improve on the results of the asymptotic method especially in moderate velocity range, but needs more work before it can be used with any realistic problems due to the computational time needed and difficulty in selecting the appropriate region of integration. The collocation method was found to be superior to both the asymptotic and Galerkin solution methods. The collocation method produces excellent results across all the speed regimes tested and the computational time is very low. It can accurately model both stabilized limit cycle oscillation motion and growth of the motion from a small initial condition. The collocation method also appears to converge even with a very simple iteration scheme when the linear flutter mode was used as the master coordinate.

The nonlinear normal mode method was applied to a beam wing model with a linear structural model and nonlinear aerodynamics. The linear modal concept of modal truncation was shown to extend to nonlinear normal modes and allowed a solution in much less time without a significant loss in accuracy. The higher order model also demonstrates that the modal coefficient solution can be used to give physical insight into how the modes used to generate the solution interact and which modes are most important in the motion. This is a primary advantage of the nonlinear normal mode method over other more purely computational methods currently available.

All in all, the nonlinear normal mode method has been shown to be a viable option for the analysis of limit cycle oscillation in aeroelastic systems and is worth further pursuit.

6.1 Future Work

During this work, several avenues for improvement of the nonlinear normal mode method have been identified.

This research limited itself to a single modal approximation function, i.e., polynomial expansion, for ease of computation and to facilitate a direct comparison between different coefficient solution methods. Higher order shape functions of the same type and other types

of modal approximation functions will likely offer benefits in accuracy and/or computational time and should be explored for both the Galerkin and collocation solution methods. A thorough study of these shape functions and guidelines for their selection could be a research topic unto itself.

The Galerkin and collocation solutions can produce excellent accuracy, but only if the integration region or collocation points are correctly selected. A method for iterating the integration region for the Galerkin solution and establishing a convergence criterion would be very beneficial for the use of the method. A simple, intuitive iteration scheme was implemented for the collocation solution. For certain cases, it will converge, but in others it may not. Although the convergence criteria is straight forward (collocation points and solution are nearly coincident), a more robust iteration scheme would benefit the collocation method.

The first-order form of the nonlinear normal mode method offers a more varied selection of master coordinates. Instead of a particular displacement and the corresponding velocity being selected, two displacements, two velocities, or a displacement and velocity from a different degree of freedom could be selected. The effect of making these different selections would be interesting and there may be some systems where it would be advantageous to pick one of these unorthodox pairs.

Throughout the process of generating a nonlinear normal mode solution, several manual steps are taken. These include: selection of the real coefficient solutions when the asymptotic method is used directly, selection of the correct master coordinates when the linear flutter mode is being used, selection of the correct nonlinear normal mode to simulate the LCO instead of a damped solution (especially important in systems with many degrees of freedom and therefore many NNMs). Procedures to automatically make these selections would greatly facilitate the use and implementation of the NNM method in more complex and higher order systems.

Finally, the next big step in moving the nonlinear normal mode method towards being useful to the aeroelastic design and analysis community is implementation in a very

realistic, aeroelastic wing model. This will likely involve the use of a finite element model. The nonlinear normal modes could be used directly with the degrees of freedom in a finite element model, but this would not be a good idea due to the very large number of nonlinear normal modes that would exist and the very large number of modal coefficients that would need to be found. A better way to approach the problem would be a modal representation of the finite element model. The linear structural dynamic modes, zero velocity aeroelastic modes, or ideally the linear aeroelastic modes at the velocity of interest could be used. The nonlinear equations of motion could be written in terms of these modes and the execution of the nonlinear normal mode solution would then be very similar to the process used many times in this work.

Bibliography

- [1] Bunton, R. W. and Denegri Jr., C. M., “Limit cycle oscillation characteristics of fighter aircraft,” *Journal of Aircraft*, Vol. 37, No. 5, 2000, pp. 916 – 918.
- [2] Denegri Jr., C. M., “Limit cycle oscillation flight test results of a fighter with external stores,” *Journal of Aircraft*, Vol. 37, No. 5, 2000, pp. 761 – 769.
- [3] Denegri Jr., C. M., Dubben, J. A., and Maxwell, D. L., “In-flight wing deformation characteristics during limit-cycle oscillations,” *Journal of Aircraft*, Vol. 42, No. 2, 2005, pp. 500 – 508.
- [4] Dowell, E., Thomas, J., Hall, K., and Denegri, C. J., “Theoretical Predictions of F-16 Fighter Limit Cycle Oscillations for Flight Flutter Testing,” *Journal of Aircraft*, Vol. 46, 2009, pp. 1667–1672.
- [5] Dawson, K. S. and Maxwell, D. L., “Limit-cycle oscillation flight-test results for asymmetric store configurations,” *Journal of Aircraft*, Vol. 42, No. 6, 2005, pp. 1589 – 1596.
- [6] Woolston, D., Runyan, H., and Byrdsong, T., “Some effects of system nonlinearities in the problem of aircraft flutter,” Tech. rep., NACA TN 3539, 1955.
- [7] Lee, B. and LeBlanc, P., “Flutter analysis of a two-dimensional airfoil with cubic nonlinear restoring force,” Tech. rep., National Research Council of Canada, Aeronautical Note, NAE-AN-36 NRC No. 25438, 1986.

- [8] Houbolt, J., “A recurrence matrix solution for the dynamic response of elastic aircraft,” *Journal of Aeronautical Sciences*, Vol. 17, 1959, pp. 540–550.
- [9] Price, J. S., Alighanbary, H., and Lee, B. H. K., “The Aeroelastic Response of a Two-Dimensional Airfoil with Bilinear and Cubic Structural Nonlinearities,” *Journal of Fluids and Structures*, Vol. 98, No. 2, 1995, pp. 175 – 175.
- [10] Krylov, N. and Bogoliubov, N., *Introduction to Nonlinear Mechanics*, , translation by Solomon Lifschitz, Princeton University Press, Princeton, New Jersey, 1947.
- [11] Zhao, L. and Yanc, Z., “Chaotic motions in an airfoil with nonlinear stiffness in incompressible flow,” *Journal of Sound and vibration*, Vol. 138, 1990, pp. 245–254.
- [12] Lee, B., Gong, L., and Wong, Y., “Analysis and computation of nonlinear dynamic response of a two-degree-of-freedom system and its application in aeroelasticity,” *Journal of Fluids and Structures*, Vol. 11, No. 3, 1997, pp. 225 – 246.
- [13] Lee, B., Jiang, L., and Wong, Y., “Flutter of an airfoil with a cubic restoring force,” *Journal of Fluids and Structures*, Vol. 13, No. 1, 1999, pp. 75 – 101.
- [14] Liu, L., Wong, Y., and Lee, B., “Application of the centre manifold theory in non-linear aeroelasticity,” *Journal of Sound and Vibration*, Vol. 234, No. 4, 2000, pp. 641 – 659.
- [15] Liu, L. and Dowell, E., “The secondary bifurcation of an aeroelastic airfoil motion: effect of high harmonics,” *Nonlinear Dynamics*, Vol. 37, No. 1, 2004/07/01, pp. 31 – 49.
- [16] Liu, L., D. E. T. J., “Higher Order Harmonic Balance Analysis for Limit Cycle Oscillations in an Airfoil with Cubic Restoring Forces,” *46th AIAA Structures, Structural Dynamics, and Materials Conference*, 2005.
- [17] O’Neil, T., Gilliatt, H., and Strganac, T., “Investigations of aeroelastic response for a system with continuous structural nonlinearities,” *Presented at 37th AIAA Structures, Structural Dynamics, and Materials Conference, AIAA Paper 96-1390*, 1996.

- [18] Gilliatt, H., Strganac, T., and Kurdila, A., “Nonlinear aeroelastic response of an airfoil,” *35th Aerospace Sciences Meeting and Exhibit, AIAA-1997-0456*, 1997.
- [19] Gilliatt, H. C., Strganac, T. W., and Kurdila, A. J., “On the presence of internal resonances in aeroelastic systems,” Vol. 3, Long Beach, CA, USA, 1998, pp. 2045 – 2055.
- [20] O’Neil, T. and Strganac, T. W., “Aeroelastic response of a rigid wing supported by nonlinear springs,” *Journal of Aircraft*, Vol. 35, No. 4, 1998, pp. 616 – 622.
- [21] Thompson, D. J. and Strganac, T., “Store-Induced Limit Cycle Oscillations and Internal Resonances in Aeroelastic Systems,” *AIAA 2000-1413, 41st AIAA Structures, Structural Dynamics, and Materials Conference*, 2000.
- [22] Sheta, E. F., Harrand, V. J., Thompson, D. E., and Strganac, T. W., “Computational and experimental investigation of limit cycle oscillations of nonlinear aeroelastic systems,” *Journal of Aircraft*, Vol. 39, No. 1, 2002, pp. 133 – 141.
- [23] Kim, K. and Strganac, T., “Aeroelastic studies of a cantilever wing with structural and aerodynamic nonlinearities,” *43rd AIAA Structures, Structural Dynamics, and Materials Conference*, 2002.
- [24] Kim, K. and Strganac, T., “Nonlinear Responses of a cantilever wing with an external store,” *44th AIAA Structures, Structural Dynamics, and Materials Conference*, 2003.
- [25] Tang, D., Dowell, E. H., and Hall, K. C., “Limit cycle oscillations of a cantilevered wing in low subsonic flow,” *AIAA journal*, Vol. 37, No. 3, 1999, pp. 364 – 371.
- [26] Tang, D., Henry, J. K., and Dowell, E. H., “Limit cycle oscillations of delta wing models in low subsonic flow,” *AIAA journal*, Vol. 37, No. 11, 1999, pp. 1355 – 1362.
- [27] Tang, D. and Dowell, E. H., “Effects of angle of attack on nonlinear flutter of a delta wing,” *AIAA journal*, Vol. 39, No. 1, 2001, pp. 15 – 21.

- [28] Attar, P., Dowell, E., and Tang, D., “A theoretical and experimental investigation of the effects of a steady angle of attack on the nonlinear flutter of a delta wing plate model,” *Journal of Fluids and Structures*, Vol. 17, No. 2, 2003, pp. 243 – 259.
- [29] Tang, D., Attar, P., and Dowell, E. H., “Flutter/limit cycle oscillation analysis and experiment for wing-store model,” *AIAA Journal*, Vol. 44, No. 7, 2006, pp. 1662 – 1675.
- [30] Tang, D. and Dowell, E. H., “Flutter and limit-cycle oscillations for a wing-store model with freeplay,” *Journal of Aircraft*, Vol. 43, No. 2, 2006, pp. 487 – 503.
- [31] Attar, P. J., Dowell, E. H., and White, J. R., “Modeling delta wing limit-cycle oscillations using a high-fidelity structural model,” *Journal of Aircraft*, Vol. 42, No. 5, 2005, pp. 1209 – 1217.
- [32] Attar, P. J., Dowell, E. H., and Tang, D., “Delta wing with store limit-cycle-oscillation modeling using a high-fidelity structural model,” Vol. 45, 1801 Alexander Bell Drive, Suite 500, Reston, VA 20191-4344, United States, 2008, pp. 1054 – 1061.
- [33] Attar, P. and Gordnier, R., “Aeroelastic prediction of the limit cycle oscillations of a cropped delta wing,” *Journal of Fluids and Structures*, Vol. 22, No. 1, 2006/01/, pp. 45 – 58.
- [34] Shaw, S. and Pierre, C., “Normal modes for non-linear vibratory systems,” *Journal of Sound and Vibration*, Vol. 164(1), 1993, pp. 85–124.
- [35] Shaw, S. and Pierre, C., “Normal modes of vibration for non-linear continuous systems,” *Journal of Sound and Vibration*, Vol. 169(3), 1994, pp. 319–347.
- [36] Pesheck, E., Boivin, N., Pierre, C., and Shaw, S., “Nonlinear Modal Analysis of Structural Systems Using Multi-Mode Invariant Manifolds,” *Nonlinear Dynamics*, Vol. 25, 2001, pp. 183–205.

- [37] Pesheck, E., Pierre, C., and Shaw, S., “A new Galerkin-based approach for accurate non-linear normal modes through invariant manifolds,” *Journal of Sound and Vibration*, Vol. 249(5), 2002, pp. 971–993.
- [38] Jiang, D., Pierre, C., and Shaw, S., “Nonlinear normal modes for vibratory systems under harmonic excitation,” *Journal of Sound and Vibration*, Vol. 288, 2005, pp. 791–812.
- [39] Pierre, C., Jiang, D., and Shaw, S., “Nonlinear normal modes and their application in structural dynamics,” *Mathematical Problems in Engineering*, Vol. 2006, 2006, pp. 1–15.
- [40] Pesheck, E., Pierre, C., and Shaw, S., “Accurate Reduced-Order Models for a Simple Rotor Blade Model Using Nonlinear Normal Modes,” *Mathematical and Computer Modelling*, Vol. 33, 2001, pp. 1085–1097.
- [41] Khalil, H. K., *Nonlinear Systems, Third Edition*, Prentice Hall, Upper Saddle River, New Jersey, 2002.
- [42] Bisplinghoff, R., Ashley, H., and Halfman, R., *Aeroelasticity*, Addison-Wesley Publishing Company, 1955.
- [43] Theodorsen, T., “General Theory of Aerodynamic Instability and the Mechanism of Flutter,” Tech. rep., NACA report 496, 1935.
- [44] Venkatesan, C. and Friedmann, P., “New Approach to Finite-State Modeling of Unsteady Aerodynamics,” *AIAA Journal*, Vol. 24, 1986, pp. 1889–1897.
- [45] Goland, M., “The Flutter of a Uniform Cantilever Wing,” *Journal of Applied Mechanics*, Vol. 12, No. 4, December 1945.
- [46] Patil, M., “Decoupled Second-Order Equations and Modal Analysis of a General Non-conservative System,” *AIAA Dynamics Specialists Conference, AIAA-2000-1654*, 2000.